Advanced Theories of Water Infiltration and Redistribution in Porous Media

Experimental Studies and Modeling

Luwen Zhuang

ISBN: 978-90-6266-447-4

Title: Advanced Theories of Water Infiltration and Redistribution in Porous Media; Experimental Studies and Modeling

NUR-code: 934

NUR-description: Hydrogeology

Number of pages: 169

Cover illustration: Luwen Zhuang

Cover lay-out: Luwen Zhuang

Printed by: ProefschriftMaken || www.proefschriftmaken.nl

Advanced Theories of Water Infiltration and Redistribution in Porous Media;

Experimental Studies and Modeling

Geavanceerde Theorieën van Waterinfiltratie en Redistributie in Poreuze Media;

Experimentele Studies en Modeleerwerk

(met een samenvatting in het Nederlands)

Proefschrift

ter verkrijging van de graad van doctor aan de Universiteit Utrecht
op gezag van de rector magnificus, prof. dr. G.J. van der Zwaan,
ingevolge het besluit van het college voor promoties
in het openbaar te verdedigen op
dinsdag 28 februari 2017 des middags te 2.30 uur

door

Luwen Zhuang

geboren op 3 augustus 1987 te Jining, Shan Dong, China

Promotor: Prof.dr.ir. S.M. Hassanizadeh

The Reading Committee

Prof. C.J. van Duijn
Technische Universiteit Eindhoven;Utrecht University
Prof. R. Helmig
Universität Stuttgart
Prof. I. Neuweiler
Leibniz Universität Hannover
Dr. A. Raoof
Utrecht University
Prof. M.Th. van Genuchten
Federal University of Rio de Janeiro; Utrecht University

The Examining Committee

Prof. A. Ahmadi
Université de Bordeaux
Prof. C.J. van Duijn
Technische Universiteit Eindhoven; Utrecht University
Prof. I. Neuweiler
Leibniz Universität Hannover
Dr. A. Raoof
Utrecht University
Prof. M.Th. van Genuchten
Federal University of Rio de Janeiro; Utrecht Univeristy

This thesis was accomplished with financial support from the China Scholarship Council (CSC).

To my parents and brother

此书献给我的父母和弟弟

Contents

Chapter 1

Introduction

1.1 Theories of unsaturated flow in soil

Traditionally, multiphase flow in porous media is described by the so-called extended Darcy's Law, which is based on the original Darcy's Law by including the relative permeability. The driving force in the horizontal direction is only the pressure gradient, which means that flow will cease without a pressure gradient. However, this is contradicted by experimental evidence (Kona, 1997). Hassanizadeh and Gray (1993b) found that the actual driving force for the horizontal flow of a phase is the gradient in the Gibbs free energy, which itself is a function of saturation, specific interfacial area, and fluid pressure. Thus, in addition to the pressure gradient, gradients in saturation and the specific interfacial area also appear in the generalized Darcy's law. This means that in principle it is possible to maintain gradients in pressure and saturation under no-flow conditions. Since few studies of the generalized formula exist, in this thesis we only consider the saturation gradient as a new driving force in order to reduce uncertainties in the estimation of parameters. The generalized Darcy's law for one-dimensional horizontal unsaturated flow is defined by

$$q^w = -\frac{k^{rw}k}{\mu^w}\left(\frac{\partial p^w}{\partial x} - \lambda\frac{\partial S^w}{\partial x}\right) \tag{1.1}$$

where S^w is water saturation, q^w is the Darcy flow velocity, k denotes the intrinsic permeability, k^{rw} is relative permeability, μ^w is the viscosity of water, and λ is a material property.

In addition to the generalized Darcy's law, the constitutive relationship between capillary pressure and saturation is fundamental to characterizing unsaturated flow in soils. Traditionally, capillary pressure, defined as the difference in fluid pressures, is assumed to be a function of saturation as follows

$$p^a - p^w = p^c(S^w) \tag{1.2}$$

where p^a and p^c are air pressure and capillary pressure, respectively. However, it is know that this relationship depends on the flow history, and hence is not a unique function. Rather than resorting to a hysteretic relationship, Hassanizadeh and Gray (1993b) have suggested that non-uniqueness in the capillary pressure-saturation relationship can be modelled by introducing the air-water specific interfacial area into the formulation. The air-water specific interfacial area, denoted by a^{wa}, is defined as the total area of all air-water interfaces within a unit volume of the porous medium.

The approach would then involve a three-dimensional surface relating interfacial area with capillary pressure and saturation (Hassanizadeh and Gray, 1993a):

$$a^{wa} = a^{wa}\left(p^c, S^w\right) \tag{1.3}$$

Projection of this surface onto the p^c-S^w plane would form the hysteresis loops of the primary (or main) drainage and imbibition curves. Several experimental and modeling studies have suggested that the saturation-capillary pressure-interfacial area surface is indeed unique for all drainage and imbibition equilibrium points, whether on the main or on scanning curves (e.g., Held and Celia, 2001; Chen and Kibbey, 2006; Chen et al., 2007; Joekar-Niasar et al., 2010; Joekar-Niasar and Hassanizadeh, 2011; Karadimitriou et al., 2014).

For the air-water specific interfacial area, an evolution equation must be provided. Assuming that the air-water interfacial mass density is constant, the following equation can be given (Hassanizadeh, 2015):

$$\frac{\partial a^{wa}}{\partial t} + \frac{\partial\left(a^{wa} w^{wa}\right)}{\partial x} = E^{wa} \tag{1.4}$$

where w^{wa} is the macroscopic flux of the specific interfacial area. This variable is given by a Darcy-type equation (Hassanizadeh, 2015):

$$w^{wa} = -k^{wa}\left(\frac{\partial a^{wa}}{\partial x} + \Omega\frac{\partial S^w}{\partial x}\right) \tag{1.5}$$

in which k^{wa} is the interfacial permeability, including surface tension, and Ω is another material coefficient. E^{wa} is the net production rate of the specific interfacial area.

Moreover, it has been reported that the relation between differences in fluid pressures and saturation during dynamic processes differs from the equilibrium relation (see e.g., Topp and Peters, 1967; Smiles et al., 1971; Vachaud et al., 1972; Elzeftawy and Mansell, 1975; Stauffer, 1978; Wildenschild et al., 2001; O'Carroll et al., 2005; Oung et al., 2005; Bottero et al., 2011; Weller et al., 2011). Stauffer (1978) proposed to define a dynamic capillary pressure in addition to the standard static capillary pressure. Through experimental studies, he found that the difference between dynamic and static capillary pressure depends linearly on the temporal rate of change of saturation.

Following Hassanizadeh and Gray (1990) and Kalaydjian (1992),we selected a different conceptual approach. The approach assumes that there is only one capillary pressure, notably the one that is measured under quasi-static conditions. What is

measured under dynamic conditions is not capillary pressure but the difference between the two fluid pressures. Based on a thermodynamic approach, Hassanizadeh and Gray (1990) and Kalaydjian (1992) showed that the difference in fluid phase pressures under dynamic conditions is not just equal to the standard capillary pressure, but includes a dynamic term depending upon the temporal rate of saturation change. A linearized approximation is written as (Hassanizadeh and Gray,1993a):

$$p^a - p^w - p^c = -\tau \frac{\partial S^w}{\partial t} \tag{1.6}$$

where τ is a non-equilibrium (or dynamic) capillarity coefficient. The capillary pressure p^c here corresponds to the pressure difference obtained under quasi-static conditions. Recent studies have suggested that the dynamic coefficient τ varies with saturation (e.g., Dahle et al., 2005; Manthey et al., 2005; Camps-Roach et al., 2010; Joekar-Niasar et al., 2010; Goel and O'Carroll, 2011; Bottero et al., 2011). Comprehensive reviews of experimental and numerical research related to the effects of dynamic capillarity are given by Hassanizadeh et al. (2002), Diamantopoulos and Durner (2011) and Joekar-Niasar and Hassanizadeh (2012).

1.2 Research objectives

The main objective of this research is to provide an increased understanding of the advanced theories of two-phase flow presented above. To achieve this objective, experiments, numerical simulations, and mathematical analyses have been performed. Specific objectives are as follows

- Simulating an existing horizontal redistribution experiment, to test the validity of the generalized Darcy's law.
- Designing, performing and simulating well-defined horizontal redistribution experiments, to have a better understanding of the generalized Darcy's law.
- Simulating an existing downward infiltration experiment, including dynamic capillarity effects.
- Analyzing the dynamic capillarity effect term mathematically, in order to gain insights in its effect on the solutions.
- Designing and performing well-defined experiments to quantify the dynamic capillarity effect.

1.3 Thesis outline

This thesis is organized as follows.

In **Chapter 2**, numerical simulation results of a recent horizontal redistribution experiment are presented. Two different modeling approaches were used to analyze this experiment. In one approach, the applicability of the standard Richards equation with a hysteretic capillary pressure-saturation relationship (including scanning curves) is assumed. The approach assumes continuity in the water pressure and flux across the contact surface between the two sides. In the second approach, an extended two-phase flow formulation involving the air-water specific interfacial area is used. For this approach, continuity in the Gibbs free energy for air-water interfaces and the interfacial area flux is used as additional conditions at the contact surface.

In **Chapter 3**, three laboratory methods are described to characterize the unsaturated soil hydraulic properties of two sands used in laboratory experiments presented later in this thesis. A small custom-built cell or box was developed to conduct multistep outflow (MSO) and multistep flux (MSF) experiments, while the commercial HYPROP (HMS) system was used for the evaporation experiments. Results obtained from the different methods are compared and discussed.

In **Chapter 4**, results of well-defined horizontal redistribution experiments are shown. Three sets of quasi one-dimensional hysteretic redistribution experiments were carried out in a Plexiglas sandbox. The sandbox was divided into two sharply different zones: wet and semi-dry parts. The wet side was initially kept at full saturation, while the initial saturation of the dry side was set as 0.2, 0.4 and 0.6 for three different experiments. These experiments were also simulated numerically.

In **Chapter 5**, simulation results of saturation overshoot observed during one-dimensional downward infiltration of water into dry sand are presented. Two alternative models were employed to perform simulations. In both models, the Richards equation, which is a combination of standard Darcy's law and the continuity equation, is employed for describing the movement of water phase. Also, in both models, the dynamic capillarity equation was employed to give the relationship between water pressure and saturation. Then, in one model, the traditional hysteretic capillary pressure-saturation curves were used, while in the second model the interfacial area-capillary pressure-saturation surface was used to simulate hysteresis. A series of sensitivity analyses was also conducted to determine the effect of various parameters on the magnitude and extent of saturation overshoot.

In **Chapter 6**, a mathematical analysis of the effect of the dynamic capillarity term in the unsaturated flow model is provided. Various relationships between τ and S^w were considered. Traveling wave solutions of the full set of equations were obtained. Parameter values for the model were based on a recent experimental study of downward infiltration of water into a relatively dry one-dimensional sand column.

In **Chapter 7**, results of a series of dynamic drainage experiments are presented. Both static and dynamic primary, main and scanning drainage experiments were performed in a small cell with highly characterized water sensors. The value of the dynamic capillarity coefficient τ was calculated based on local pressure differences and average saturation measurements during static and dynamic drainage experiments.

In **Chapter 8**, the main conclusions and recommendations for future work are presented.

References

Bottero, S., S.M. Hassanizadeh, P.J. Kleingeld, and T.J. Heimovaara. 2011. Nonequilibrium capillarity effects in two-phase flow through porous media at different scales. Water Resour. Res. 47: W10505.

Camps-Roach, G., D.M. O'Carroll, N.T. A., and S. Toshihiro. 2010. Experimental investigation of dynamic effects in capillary pressure: Grain size dependency and upscaling Geremy. Water Resour. Res. 44: W08544.

Chen, L., and T.C.G. Kibbey. 2006. Measurement of air-water interfacial area for multiple hysteretic drainage curves in an unsaturated fine sand. Langmuir 22(16): 6874–6880.

Chen, D., L.J. Pyrak-Nolte, J. Griffin, and N.J. Giordano. 2007. Measurement of interfacial area per volume for drainage and imbibition. Water Resour. Res. 43(12): W12504.

Dahle, H.K., M.A. Celia, and S.M. Hassanizadeh. 2005. Bundle-of-tubes model for calculating dynamic effects in the capillary-pressure-saturation relationship. Transp. Porous Media 58(1): 5–22.

Elzeftawy, A., and R.S. Mansell. 1975. Hydraulic conductivity calculations for unsaturated steady-state and transient-state flow in sand. p. 599–603. *In* Soil Sci. Soc. Am. J.

Goel, G., and D.M. O'Carroll. 2011. Experimental investigation of nonequilibrium capillarity effects: Fluid viscosity effects. Water Resour. Res. 47(9): 1–15.

Hassanizadeh, S.M. 2015. Advanced Theories of Two-Phase Flow in Porous Media. p. 47–62. *In* Handbook of Porous Media, Third Edition. CRC Press.

Hassanizadeh, S.M., M.A. Celia, and H.K. Dahle. 2002. Dynamic effect in the capillary pressure-saturation relationship and its impacts on unsaturated flow. Vadose Zone J. 1(1): 38–57.

Hassanizadeh, S.M., and W.G. Gray. 1990. Mechanics and thermodynamics of multiphase

flow in porous media including interphase boundaries. Adv. Water Resour. 13(4): 169–186.

Hassanizadeh, S.M., and W.G. Gray. 1993a. Thermodynamic basis of capillary pressure in porous media. Water Resour. Res. 29(10): 3389–3405.

Hassanizadeh, S.M., and G.W. Gray. 1993b. Toward an improved description of the physics of two-phase flow. Adv. Water Resour. 16: 53–67.

Held, R.J., and M.A. Celia. 2001. Modelling support of functional relationships between capillary pressure, saturation, interfacial area and common lines. Adv. Water Resour. 24: 325–343.

Joekar-Niasar, V., and S.M. Hassanizadeh. 2011. Specific interfacial area: The missing state variable in two-phase flow equations? Water Resour. Res. 47: W05513.

Joekar-Niasar, V., and S.M. Hassanizadeh. 2012. Analysis of fundamentals of two-phase flow in porous media using dynamic pore-network models: A review. Crit. Rev. Environ. Sci. Technol. 42(18): 1895–1976.

Joekar-Niasar, V., S.M. Hassanizadeh, and H.K. Dahle. 2010. Non-equilibrium effects in capillarity and interfacial area in two-phase flow: dynamic pore-network modelling. J. Fluid Mech. 655: 38–71.

Kalaydjian, F.-M. 1992. Dynamic capillary pressure curve for water/oil displacement in porous media: Theory vs. experiment. *In* SPE Annual Technical Conference and Exhibition. Society of Petroleum Engineers.

Karadimitriou, N.K., S.M. Hassanizadeh, V. Joekar-Niasar, and P.J. Kleingeld. 2014. Micromodel study of two-phase flow under transient conditions: Quantifying effects of specific interfacial area. Water Resour. Res. 50(10): 8125–8140.

Kona, S. 1997. Experimental investigation of horizontal redistribution of water in unsaturated porous media. University of Minnesota, M. Sc thesis.

Manthey, S., S.M. Hassanizadeh, and R. Helmig. 2005. Macro-scale dynamic effects in homogeneous and heterogeneous porous media. Transp. Porous Media 58(1–2): 121–145.

O'Carroll, D.M., T.J. Phelan, and L.M. Abriola. 2005. Exploring dynamic effects in capillary pressure in multistep outflow experiments. Water Resour. Res. 41(11): 1–14.

Smiles, D.E., G. Vachaud, and M. Vauclin. 1971. A test of the uniqueness of the soil moisture characteristic during transient, nonhysteretic flow of water in a rigid soil1. Soil Sci. Soc. Am. J. 35(4): 534–539.

Stauffer, F. 1978. Time dependence of the relations between capillary pressure, water content and conductivity during drainage of porous media. p. 29 Aug-1 Sept. *In* IAHR symposium on scale effects in porous media, Thessaloniki, Greece.

Topp, G., and A. Peters. 1967. Comparison of water content-pressure head data obtained by equilibrium, steady-state, and unsteady-state methods1. Soil Sci. Soc. Am. J. 31(3): 312–314.

Vachaud, G., M. Vauclin, and M. Wakil. 1972. A study of the uniqueness of the soil moisture characteristic during desorption by vertical drainage. Soil Sci. Soc. Am. J. 36(3): 531–532.

Weller, U., O. Ippisch, M. Köhne, and H.-J. Vogel. 2011. Direct measurement of unsaturated conductivity including hydraulic nonequilibrium and hysteresis. Vadose Zone J. 10(2): 654–661.

Wildenschild, D., J.W. Hopmans, and J. Simunek. 2001. Flow rate dependence of soil hydraulic characteristics. Soil Sci. Soc. Am. J. 65(1): 35–48.

Chapter 2

Modeling of Horizontal Water Redistribution in an Unsaturated Soil

Published as: Zhuang, L., S.M. Hassanizadeh, M.Th. van Genuchten, A. Leijnse, A. Raoof, and C. Qin. 2016. Modeling of horizontal water redistribution in an unsaturated soil, Vadose Zone J., 15(3).

Abstract

When two soil samples with the same hydraulic properties but different initial water saturations are brought into contact, water will redistribute horizontally between the samples until some equilibrium is reached. The part with a higher initial saturation undergoes drainage, while imbibition occurs in the other part. Hysteresis will not allow water to redistribute evenly between the two parts. In this study we used two different modeling approaches to analyze a recent experiment related to the water redistribution process. In one approach, we assumed applicability of the standard Richards equation with a hysteretic capillary pressure-saturation relationship (including scanning curves). This approach assumes continuity in the water pressure and flux across the contact surface between the two sides. In the second approach, we used an extended two-phase flow formulation based on rational thermodynamics principles and involving the air-water specific interfacial area. For this approach, we used continuity in the Gibbs free energy for air-water interfaces and the interfacial area flux as additional conditions at the contact surface. We employed two different initial conditions: uniform initial saturation for each side and slightly non-uniform initial saturation distributions consistent with the measured water contents. We compared results of both models with measurements. The Richards equation with full hysteresis could not reproduce the measured saturation distribution unless an unrealistic value of the imbibition retention curve was assigned. The interfacial area model compared well with the experimental data after optimization of some of the model parameters.

2.1 Introduction

The process of moisture redistribution in soils has attracted much attention because of its importance to many practical problems in soil science, hydrology and agricultural engineering, as well as for various porous media processes in industry. Similar redistribution processes in multi-fluid systems occur in petroleum engineering and carbon sequestration problems. Starting with early studies by Always and Clark (1911), Haines (1930) and especially Youngs (1958), many have focused on the vertical redistribution of water following infiltration (Biswas et al., 1966; Staple, 1969; Vachaud and Thoney, 1971; Talsma, 1974; Youngs and Poulovassillis, 1976, among others). A limited number of experimental studies also investigated horizontal redistribution processes in homogeneous soils (Vachaud, 1969; Kona, 1997; Feuring et al., 2014). These studies revealed different moisture distributions within the dry and wet parts of the porous media, presumably caused by macroscopic hysteresis in the soil hydraulic properties.

Many empirical and approximate theoretical models have been used to describe hysteresis in the soil hydraulic properties. Empirical descriptions include those by Dane and Wierenga (1975), Scott et al. (1983), Kool and Parker (1987), Parker and Lenhard (1987), and Luckner et al. (1989). Theoretical approaches include various independent and dependent domain models such as those described by Everett (1954), Polouvassillis (1962), Philip (1964), Topp (1971), Mualem (1975), Polouvassillis and El-Ghamry (1978) and Mualem (1984). Useful reviews of different approaches and comparisons with experimental data are given by Jaynes (1984) and Pham et al. (2005).

The various approaches above are based on relatively standard formulations involving the Richards equation for variably-saturated flow, or related models for multiphase systems. Application of these formulations to transient redistribution processes requires the use of hysteretic relationships for the constitutive (soil hydraulic) functions. An alternative approach is based on thermodynamic principles that consider the effects of specific interfacial area on fluid flow (Hassanizadeh and Gray, 1990). While many numerical studies have been carried out to investigate the general properties of this theory (Niessner and Hassanizadeh, 2008; Pop et al., 2009; Marshall, 2009; Joekar-Niasar and Hassanizadeh, 2011), the approach has never been used to analyze experimental data.

In this work, we used results of recent horizontal redistribution experiments performed by Feuring et al. (2014) to investigate the applicability of the thermodynamics-based

model of Hassanizadeh and Gray (1990), to which we refer as the interfacial area model. We simulated the experiments of Feuring et al. (2014) using two different approaches: the standard Richards equation with and without capillary hysteresis effects, and the extended Darcy model that includes the air-water interfacial area. Below we first provide a brief overview of the horizontal redistribution experiment of Feuring et al. (2014). Subsequently, we describe the standard and interfacial area models used in our study, and compare the modeling results with the experimental data.

2.2 Description of experiments

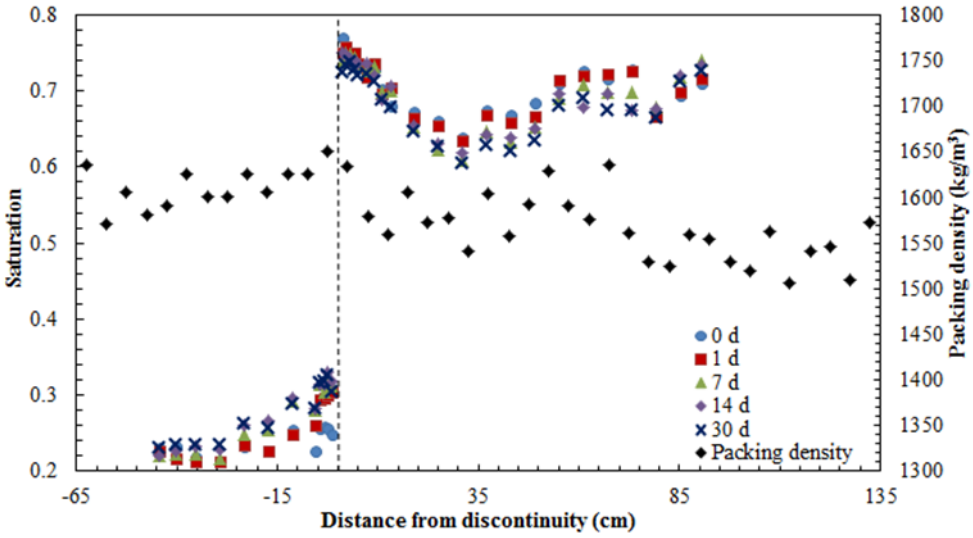

Figure 2.1 Measured packing density (black diamonds) and saturation profiles at different times (other symbols) along the flume (Feuring et al., 2014)

The experiments by Feuring et al. (2014) were designed to observe water redistribution in a long horizontal homogeneous soil flume with a discontinuity in initial saturation. They used a flume with dimensions of 200 cm (length) × 3 cm (height) × 4 cm (width). The flume was packed with sand having a mean grain diameter of 0.29 mm, and with minimum and maximum grain sizes of 0.05 mm and 2 mm, respectively. Initial water saturation along the flume was not uniform: one part, covering 65 cm ($-65 \leq x < 0$), had a relatively low saturation (average of 0.23), while the remaining 135 cm ($0 < x \leq 135$) was relatively wet (average of 0.70). The particle density was 2546 kg m^{-3}, and the average packing bulk density was 1.65×10^{-3} kg m^{-3}. Bulk densities along the flume were measured destructively every 5 cm after the flow

experiment was terminated. Results in Figure 2.1 indicate that bulk densities fluctuated slightly along the flume, and hence that the flume was not perfectly homogeneous. These results were also used to calculate porosity.

Table 2.1 Measured soil properties and parameter values

Parameter	Unit	Value
Particle density, ρ^s	kg m^{-3}	2546
Packing bulk density, ρ^b	kg m^{-3}	1650
Average porosity, φ	-	0.4
Water density, ρ^w	kg m^{-3}	998.2
Water viscosity, μ^w	Pa·s	1×10^{-3}
Main drainage retention exponent, n	-	5.0
Main drainage retention parameter, α	m^{-1}	3.26
Main imbibition retention exponent, n	-	5.0
Main imbibition retention parameter, α	m^{-1}	6.94
Irreducible water saturation, S_{ir}^w	-	0.19
Saturated hydraulic conductivity, K_s	m s^{-1}	6.38×10^{-4}
Intrinsic permeability, k	m^2	6.52×10^{-11}

The capillary pressure-saturation curves for primary drainage and main imbibition were measured by Feuring (2010). Figure 2.2 shows the measured data along with the fitted curves used in our calculations. As can be seen, residual air saturation was found to be negligible. The primary drainage curve hence coincided with the main drainage curve. We will further refer to this curve as the main drainage curve. The saturated hydraulic conductivity (K_s) was also measured, using a constant head permeameter, and was found to be 6.38×10^{-4} m s^{-1}, or 55.12 m d^{-1} (Feuring et al., 2014). The measurement of K_s was repeated recently, and the same value was found. Various soil physical and hydraulic parameter values are summarized in Table 2.1.

The dry and wet sides of the flume were initially separated by a very thin (0.044 mm) removable metal sheet. The entire system was made air-tight. Both sides were first allowed to reach equilibrium, after which the sheet was removed to start the redistribution process. Saturation values and air and water pressures along the flume were measured before the sheet was removed, and then repeatedly during a period of 30 days afterwards. Water and air pressures were measured with hydrophilic and hydrophobic tensiometers, respectively. Transducer pairs were installed at 12 locations

along the flume. The air pressure presented very little variation along the flume, and hence was assumed to be constant. In our numerical studies, we assumed the air pressure to be atmospheric. Saturation along the flume was monitored using a gamma radiation system. For the calculation of saturation, the gamma measurements had to be recalibrated based on measured values of the bulk density of the soil. These were measured destructively after the experiment terminated. The soil in the flume was subsequently collected in 5-cm segments to obtain precise gravimetric measurements of the bulk density along the flume. Measured saturation profiles at six different times are shown in Figure 2.1 (Feuring et al., 2014). Figures 2.3a and 2.3b display measured water pressures as a function of time at various points in the initially dry and wet sides, respectively. The tensiometer at -1 cm malfunctioned during the entire experiment, while the tensiometer at -6 cm stopped working properly after 15 days. Erroneous data from these two tensiometers are not included in Figure 2.3.

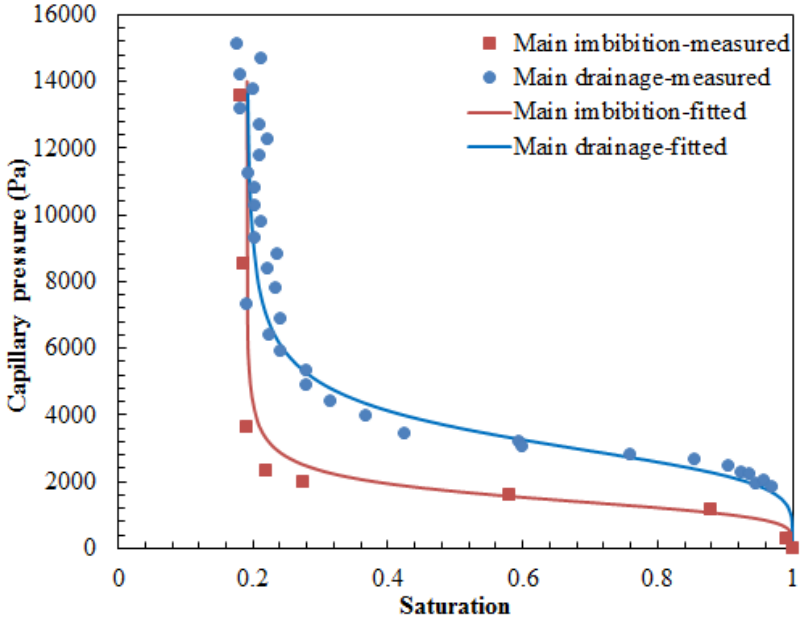

Figure 2.2 Measured and fitted van Genuchten main drainage and imbibition curves (Feuring, 2010)

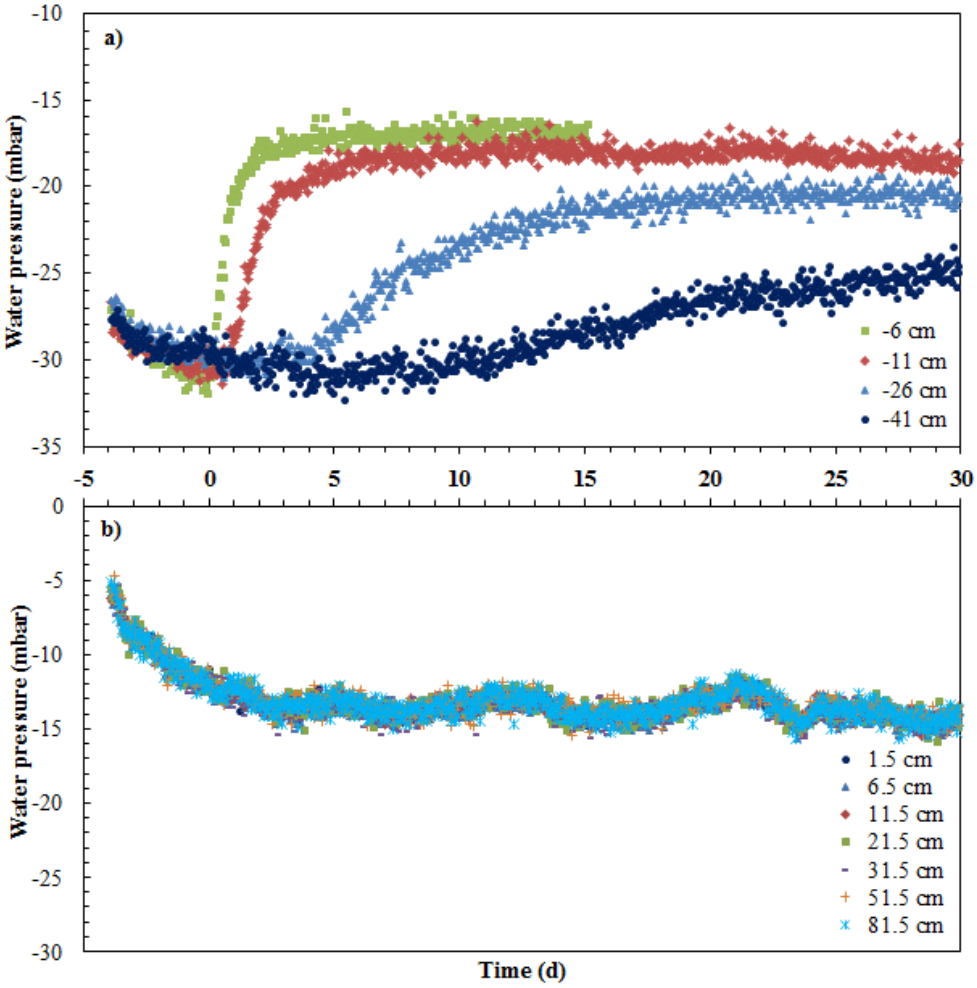

Figure 2.3 Water pressures versus time at several locations within the initially dry (a) and wet (b) sides of the flume (Feuring et al., 2014)

Figure 2.1 shows that saturation values increased rapidly in the dry side (x<0) within seven days, after which moisture redistribution slowed down substantially. By comparison, saturation in the wet side (x>0) decreased gradually and almost evenly along the entire subdomain. This was due to the much higher unsaturated hydraulic conductivities in the wet side, which led to very small pressure head gradients. As seen in Figure 2.1, the saturation discontinuity at the contact surface between the two domains (at x=0) persisted during the entire experiment. In the dry side, water pressures at positions near the contact surface increased rapidly, while pressures

started to increase much later and much slower farther away from the contact surface (see Figure 2.3). By comparison, water pressures in the wet side decreased only slightly and more uniformly. Although changes in the water pressure with time had not completely ceased after one month, the experiment was terminated, since changes in saturation were not measurable any more. The total water mass balance was evaluated gravimetrically before and after the experiments. A loss of only 7% water was found.

In the following we describe two alternative modeling approaches for analysis of the experimental data of Feuring et al. (2014). Both modeling approaches neglect any influence of the air phase since fewer variations were observed in the air pressure along the flume.

2.3 Numerical models

2.3.1 Standard model

The HYDRUS-1D software package of Simunek et al. (2013) was used to simulate the horizontal redistribution experiment of Feuring et al. (2014). HYDRUS-1D uses the finite element method to solve the Richards equation for water flow in an unsaturated porous medium. For one-dimensional horizontal flow, Richards equation reduces to:

$$\varphi \frac{\partial S^w}{\partial t} = \frac{\partial}{\partial x}\left[K(S^w) \frac{\partial h}{\partial x} \right] \tag{2.1}$$

where S^w is saturation, φ is porosity, h is the soil water pressure head defined as $h=p^w/\rho^w g$, with p^w and ρ^w being the water pressure and density, respectively, K is the unsaturated hydraulic conductivity (assumed to be a function of the pressure head), t is time, and x is the spatial coordinate.

Formulas suggested by van Genuchten (1980) equations were used to characterize the nonlinear relationships between h and S^w, and between K and S^w as follows:

$$h = -\frac{1}{\alpha}\left[S_e^{-1/m} - 1 \right]^{1/n} \tag{2.2}$$

$$K\left(S^w\right) = K_s (S_e)^l \left[1 - \left(1 - S_e^{1/m} \right)^m \right]^2 \tag{2.3}$$

$$S_e = \frac{S^w - S_{ir}^w}{1 - S_{ir}^w} \tag{2.4}$$

where S_{ir}^{w} and S_e are the residual and effective water saturations, respectively, α and n are fitting parameters, m=1-1/n, and l=0.5. Figure 2.2 compares the measured and fitted capillary pressure-saturation curves for main drainage and imbibition. A good fit was found, with the hydraulic parameter α for imbibition being approximately twice the value for drainage (see Table 2.1), as is often assumed in unsaturated flow studies (e.g., Luckner et al., 1989).

Hysteresis in HYDRUS-1D is simulated by means of scanning curves that are obtained by scaling the main imbibition and drainage curves. Every individual nodal point in the numerical model is assigned its own set of scanning curves, which are used depending upon whether drying or wetting occurs. In our study we used the approach of Lenhard and Parker (1991) to generate the various scanning curves. Their method assumes closure of the scanning loops by forcing the scanning curves to pass through the latest imbibition or drainage reversal points, thus avoiding so-called artificial pumping errors (Werner and Lockington, 2006; Šimůnek et al., 2009). Consistent with the simplified hysteresis formulations by Kool and Parker (1987), Luckner et al. (1989), and Lenhard and Parker (1991), we used for all scanning curves the same values of α and n (the former depending upon imbibition or drainage), but different values for porosity and residual water saturation. We later used the measured bulk densities, as shown in Figure 2.1, in some of the simulations to slightly adjust the values of porosity along the entire domain. This was done to account more precisely for the packing heterogeneity.

For the simulations with HYDRUS-1D we assigned 400 elements distributed evenly over the entire flow domain (2 meters). A small grid spacing was selected to render numerical dispersion of the wetting front negligible. No-flow boundary conditions were applied to both ends of the flume, while pressure heads and water fluxes were assumed to be continuous across the contact surface. The initial condition could be defined in terms of either saturation or pressure head. We performed two sets of simulations assuming either a homogeneous or heterogeneous porous medium as follows:

1) Uniform saturation values were assigned to each side (dry or wet) with a discontinuity at the contact surface. The capillary pressure-saturation curves (the main curves as well as the scanning curves) were assumed to be the same for all elements. The saturation values were based on the means of the measured initial saturations of the wet and dry sides.

2) Non-uniform measured water saturation or pressure head values were assigned as initial conditions along each side. Different porosity values and capillary pressure-saturation curves (the main or scanning curves) were assigned to different sections along the flume, consistent with the measured bulk densities shown in Figure 2.1.

2.3.2 Interfacial area model

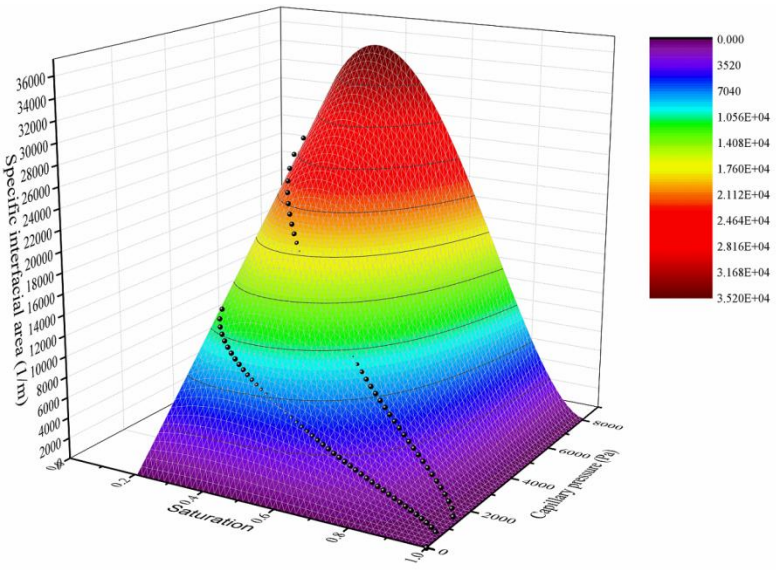

Figure 2.4 A three-dimensional surface of capillary pressure, saturation and specific interfacial area

The capillary pressure (p^c)-saturation (S^w) relationship (or water retention curve) used in the standard Richards equation depends on the flow history, and hence is not a unique function. Rather than resorting to a hysteretic relationship, Hassanizadeh and Gray (1993b) suggested that non-uniqueness in the capillary pressure-saturation relationship can be modelled by introducing the air-water specific interfacial area into the formulation. The air-water specific interfacial area, denoted by a^{wa}, is defined as the total area of all air-water interfaces within a unit volume of the porous medium. The approach would then involve a three-dimensional surface relating interfacial area with capillary pressure and saturation (Hassanizadeh and Gray, 1993a). Projection of this surface onto the p^c-S^w plane would form the hysteresis loop of the primary (or main) drainage and imbibition curves. Several experimental and modeling studies have suggested that the saturation-capillary pressure-interfacial area surface is indeed

unique for all drainage and imbibition equilibrium points, whether on the main or on scanning curves (e.g., Held and Celia, 2001; Chen and Kibby, 2006; Chen et al., 2007; Joekar-Niasar et al., 2007, 2011, 2012; Karadimitriou et al., 2014).

The three-dimensional p^c-S^w-a^{wa} surface for a given soil has to be obtained experimentally. In the experiments of Feuring et al. (2014), only the main drainage and imbibition curves were measured. For this reason we tried to develop a p^c-S^w-a^{wa} relationship in which the projection onto the p^c-S^w plane would reproduce the measured p^c-S^w curves. To do so, we had to estimate values of the specific interfacial area corresponding to measured p^c-S^w data points of the drainage and imbibition curves. We followed the method of Niemet et al. (2002) to calculate specific interfacial areas. The resulting p^c-S^w-a^{wa} points were fitted with the following power function proposed by Joekar-Niasar and Hassanizadeh (2012):

$$a^{wa}\left(S^w, p^c\right) = \gamma_1 S^w \left(1 - S^w\right)^{\gamma_2} \; p^{c^{\gamma_3}} \tag{2.5}$$

$$p^c = p^a - p^w \tag{2.6}$$

where p^c and p^a are the capillary and air pressures, respectively, and γ_1, γ_2 and γ_3 are empirical parameters. Equation (2.5) restricts the interfacial area to the physical range where water saturation varies between zero and one. The fitted surface area and its parameters are given in Figure 2.4 and Table 2.2, respectively. The black dots in Figure 2.4 correspond to p^c-S^w-a^{wa} points obtained using the approach of Niemet et al. (2002). We note that dynamic capillarity effects are neglected in Equation (2.6).

Table 2.2 Values of the coefficients in Equation (2.5)

Parameter	Value	Standard error
γ_1	24.60	3.685
γ_2	1.73	0.275
γ_3	1.01	0.017
R^2	0.992	

Next we introduce the generalized Darcy's law. Hassanizadeh and Gray (1993b) found that the real driving force for the horizontal flow of a phase is the gradient in the Gibbs free energy, which is a function of saturation, specific interfacial area and fluid pressure. Thus, in addition to the pressure gradient, gradients in saturation and specific interfacial area also appear in the generalized Darcy's law. This means that it is in principle possible to maintain gradients in pressure and saturation under no-flow

condition. Since few studies of the generalized formula exist, we only included the saturation gradient as a new driving force in order to reduce uncertainties in the estimation of parameters. The model for one-dimensional horizontal flow is defined by the following set of equations consisting of continuity equations for the water phase and the specific interfacial area, as well as the generalized Darcy's law (Niessner and Hassanizadeh, 2008; Pop et al., 2009):

$$\varphi \frac{\partial S^w}{\partial t} + \frac{\partial q^w}{\partial x} = 0 \tag{2.7}$$

$$\frac{\partial a^{wa}}{\partial t} + \frac{\partial \left(a^{wa} w^{wa} \right)}{\partial x} = E^{wa} \tag{2.8}$$

$$q^w = -\frac{k^{rw} k}{\mu^w} \left(\frac{\partial p^w}{\partial x} - \lambda \frac{\partial S^w}{\partial x} \right) \tag{2.9}$$

$$k^{rw} = S_e^{\ \delta} \tag{2.10}$$

where q^w is the Darcy flow velocity, k denotes the intrinsic permeability, k^{rw} is relative permeability, μ^w is the viscosity of water, λ is a material property, w^{wa} is the macroscopic flux of the specific interfacial area, δ is the exponent for the relative permeability, and E^{wa} is the net production rate of the specific interfacial area.

Hassanizadeh and Gray (1993b) proposed the following Darcy type equation for the flux of fluid-fluid interfaces:

$$w^{wa} = -k^{wa1} \left[\frac{\partial \left(a^{wa} \sigma^{wa} \right)}{\partial x} + \psi^{wa} \frac{\partial S^w}{\partial x} \right] \tag{2.11}$$

where k^{wa1} represents the interfacial permeability, ψ^{wa} is a material coefficient and σ^{wa} denotes the average interfacial tension. Since σ^{wa} is constant for air-water interfaces at constant temperature, Equation (2.11) simplifies to:

$$w^{wa} = -k^{wa1} \sigma^{wa} \left(\frac{\partial a^{wa}}{\partial x} + \frac{\psi^{wa}}{\sigma^{wa}} \frac{\partial S^w}{\partial x} \right) = -k^{wa} \left(\frac{\partial a^{wa}}{\partial x} + \Omega \frac{\partial S^{wa}}{\partial x} \right) \tag{2.12}$$

in which k^{wa} and Ω are adjusted material properties that include the effect of the average interfacial tension.

Compared to the model of Niessner and Hassanizadeh (2008) and Pop et al. (2009), we employed a simpler relationship for the production term. Based on the analysis given in Appendix A, the following relationship was used for the production term E^{wa}:

$$E^{wa} = -\kappa \frac{\partial a^{wa}}{\partial p^{c}} \frac{\partial S^{w}}{\partial t} \tag{2.13}$$

The above system of equations (i.e., Equations (2.5)-(2.13)) can be solved numerically in terms of the two primary variables: S^w and p^c. The solution still requires certain continuity conditions at the contact surface between the two domains where saturation is discontinuous. For the water phase we assumed continuity in the water flux and the pressure across the contact surface between the wet and dry domains. For the air-water interface we assumed continuity in the interfacial area flux, $a^{wa}w^{wa}$. One more condition is still needed to obtain a complete description of the interfacial area model. This was done by specifying continuity in the Gibbs free energy for the air-water interfaces. The corresponding expression of continuity is derived in Appendix B. The model hence imposed continuity in $ln a^{wa} + \Omega S^w / a^{wa}$ across the contact surface. As boundary conditions we assigned zero fluxes for both water and the interfacial areas.

The full set of equations describing the interfacial area model was solved numerically by means of COMSOL Multiphysics 4.4 (COMSOL, 2014). A small grid size of 0.001 m was employed to achieve mesh-independent solutions. An adaptive time-step size was used based on a residual error of 10^{-6}. The equations were solved for both the dry and wet domains, and coupled with each other by continuity conditions across the contact surface, as explained earlier.

2.4 Numerical results

We performed two sets of simulations using both the standard model and the interfacial area model. For one set we assumed uniform initial conditions (albeit with different initial saturations for the dry and wet sides). The purpose of this set of simulations was to compare predictions obtained with the two modelling approaches. For the second set we assigned non-uniform initial conditions, corresponding to the measured data. Results of this set of simulations were compared to experimental data.

2.4.1 Simulations with the Richards equation; uniform initial conditions

Two different simulations were carried out with the Richards equation: with and without hysteresis. We recognize that the simulations are relatively standard, but are included in this chapter to provide a comparison with the interfacial area model. Uniform initial saturation values of 0.23 and 0.70 were assigned to the dry and wet sides, respectively. The sand was assumed to be in an imbibition state initially, consistent with the manner in which the flume was packed. For the non-hysteretic case we used the main imbibition p^c–S^w curve for both sides. For the hysteretic case we used the main imbibition curve for the dry side and the main drainage curve for the wet side.

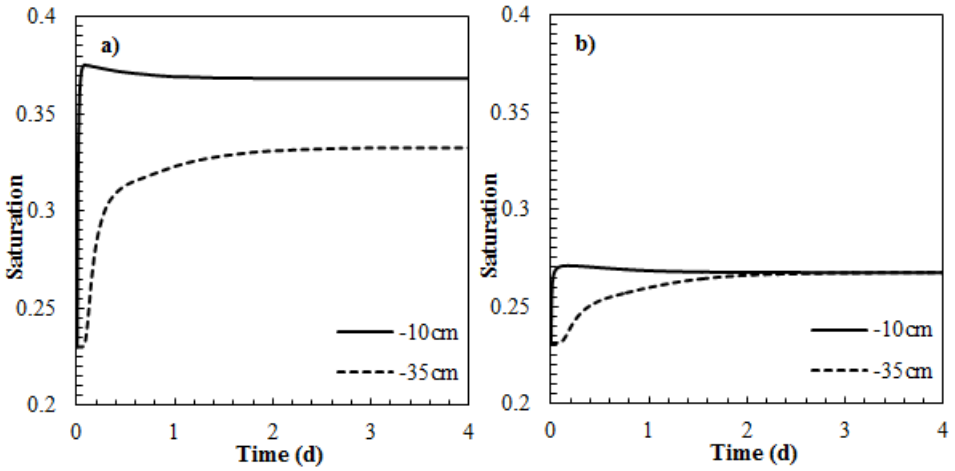

Figure 2.6 Calculated saturation values versus time at -10 and -35 cm (the dry side) using the standard model with hysteresis (a), and the interfacial area model using the standard Darcy's law (b)

Figures 2.5a and 2.5b show calculated saturation and water pressure profiles as obtained with the Richards equation without accounting for capillary hysteresis. Results show that the initial saturation and water pressure discontinuities disappeared as soon as redistribution started. A significant change in saturation in both sides is evident already after 0.5 days. The entire system was essentially at equilibrium already after only one day, with the final saturation distribution being uniform over the entire domain. Clearly, the numerical results in Figures 2.5a and 2.5b, obtained with the Richards equation without hysteresis are very much at odds with typical observations, such as the measurements shown in Figures 2.1 and 2.3.

Figures 2.5c and 2.5d show similar saturation and water pressure distributions when considering hysteresis. At the contact surface, saturations of the wet and dry sides

decreased and increased, respectively, almost immediately to values that remained nearly constant in time. Equilibrium distributions in both sides were reached within about one day. This is contrary to the experimental data (Figure 2.1), which show that complete equilibrium was probably not reached even after 30 days. Figure 2.5c clearly shows the persistence of the saturation discontinuity when hysteresis was included in the Richards equation. While different saturation distributions were obtained for the non-hysteretic and hysteretic cases, water pressure profiles and their changes in time were comparable. The time scale of change in the calculated saturation and pressure distributions, however, was much faster than the observations.

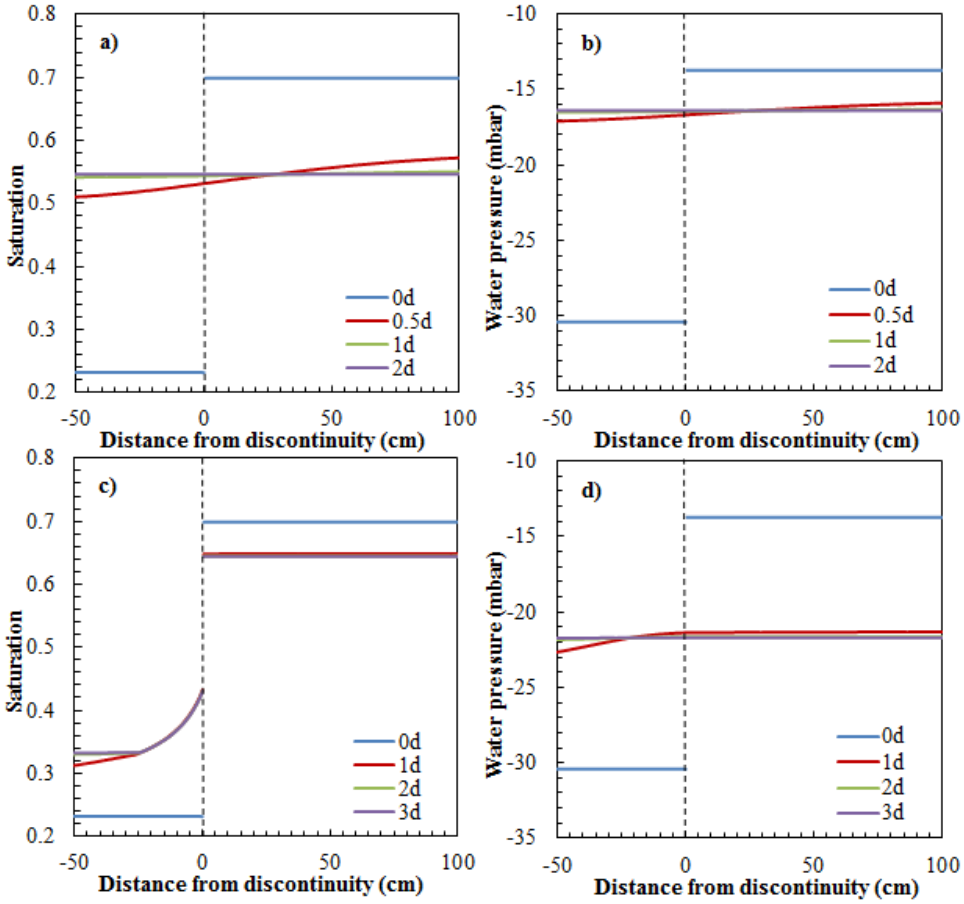

Figure 2.5 Saturation and water pressure distributions along the entire domain simulated with the Richards equation without (a, b) and with (c, d) accounting for hysteresis.

An interesting simulation result for the hysteretic case is that the saturation gradient was found to persist in the dry part, even at equilibrium, which is in agreement with the observed data. The reason is that saturation of the soil in the dry side close to the contact surface increased dramatically at first, but then started to decrease. We selected two points in the dry side to illustrate this difference in saturation. Figure 2.6a shows saturation values versus time at two locations in the initially dry side (-10 and -35 cm). Saturation at -10 cm increased rapidly to 0.38 but thereafter decreased slowly to reach a final value of about 0.37. This point hence was first subject to imbibition and then to slow drainage until the redistribution process covered the entire dry side. By comparison, the point at -35 cm only exhibited imbibition. The two points hence followed different capillary pressure-saturation scanning branches, leading to different saturations even though the final pressure values were the same as shown in Figure 2.5d.

2.4.2 Simulations with the interfacial area model; uniform initial saturation

We performed two sets of simulations with the interfacial area model in order to show the type of saturation and pressure distributions it prescribed. In one case we assumed that applicability of the standard Darcy's law (i.e., with λ=0 in Equation (2.9)), in the other case we used the generalized Darcy's law ($\lambda \neq 0$).

As initial conditions we specified the same uniform saturation values in each side as used for the HYDRUS calculations. For the interfacial area model we also needed to specify initial pressure distributions. These were chosen to be also uniform in each side and obtained from the imbibition curve corresponding to the initial saturation values. A single p^c-S^w-a^{wa} surface was used for both the dry and wet sides. The set of equations defining the interfacial area model contains five parameters (k^{wa}, Ω, κ, δ and λ). For our simulations we chose parameter values used in several earlier studies (notably Niessner and Hassanizadeh, 2008). These were: $k^{wa}=10^{-17}$ m^3 s^{-1}, $\Omega=4000$ m^{-1}, $\kappa=3\times10^4$ Pa, $\delta=3$, and $\lambda=2\times10^4$ Pa.

Figures 2.7a and 2.7b show the calculated distributions of saturation and the water pressure, respectively, using the standard Darcy's law (λ=0). Redistribution of water in both sides occurred mostly within two days, with the entire domain reaching equilibrium within three days. The saturation discontinuity at the contact surface persisted, despite the fact that a single p^c-S^w-a^{wa} surface was used for both sides.

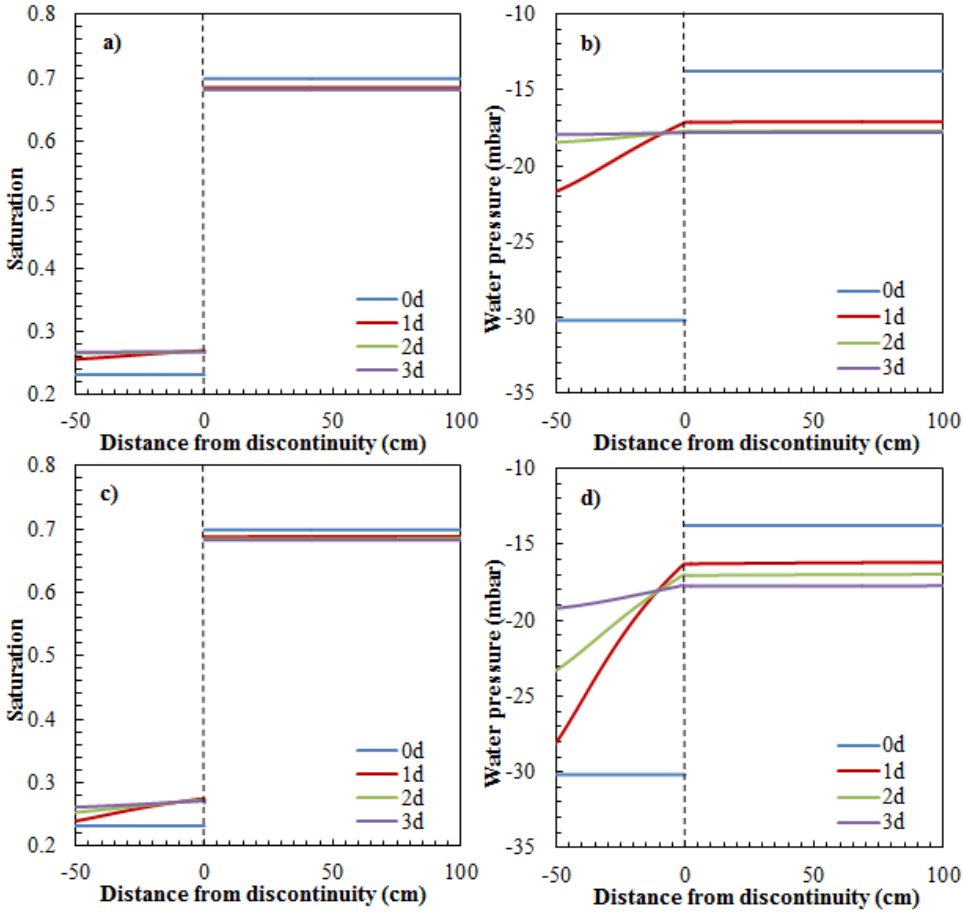

Figure 2.7 Saturation and water pressure distributions along the entire domain simulated with the interfacial area model using the standard Darcy's law (a,b), and the generalized Darcy's law (c,d)

Results of simulations with the generalized Darcy's law ($\lambda \neq 0$) are shown in Figures 2.7c and 2.7d. Saturation in the dry side increased much more gradually, while a significant gradient remained in the water pressure distribution, even after three days. The generalized Darcy's formulation ($\lambda \neq 0$) hence produced a much lower water flux, which increased the required equilibration time as compared with the standard Darcy formulation ($\lambda = 0$). An important result here is that saturation is uniform along each side at equilibrium. Thus, contrary to the standard model, the interfacial area model does not produce a non-uniform saturation distribution in the dry side, which is not in agreement with experiments. We further illustrate in Figure 2.6b the saturation changes versus time at the same points (-10 and -35 cm) in the dry side, as before for

the Richards equation. Compared with the standard model (Figure 2.6a), qualitatively similar (but lower) saturation distributions were obtained, except the identical saturation values were reached at the two points (-10 and -35 cm) at equilibrium.

2.4.3 Simulations with both models; spatially variable initial saturation distributions

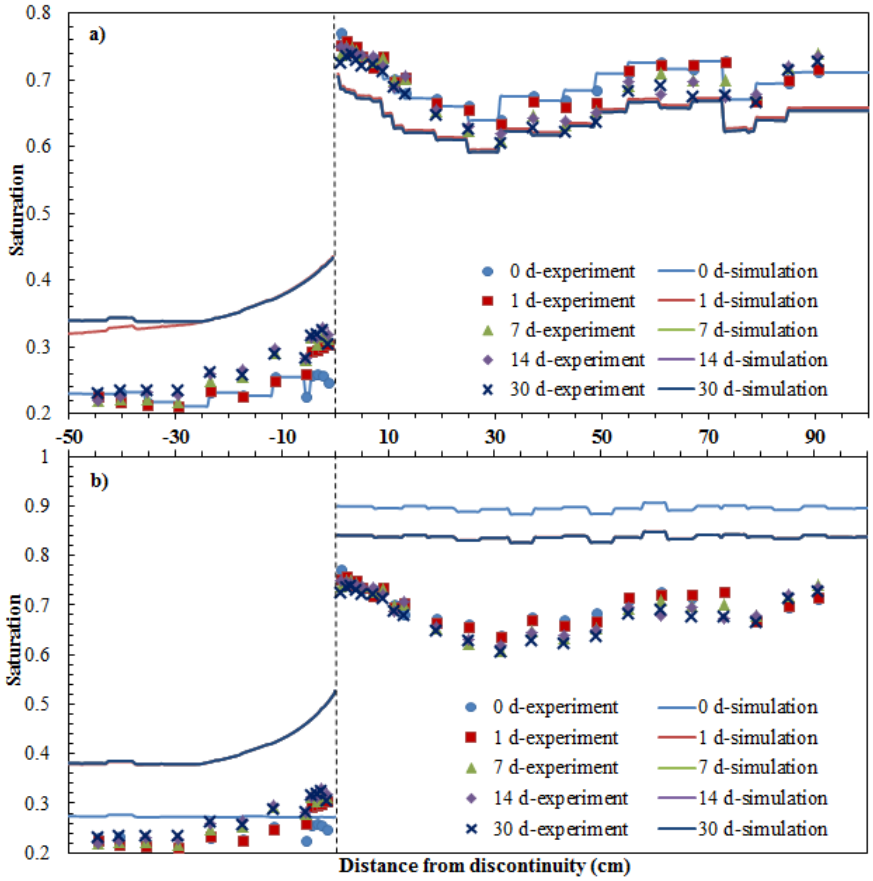

Figure 2.8 Observed saturation profiles and fitted curves obtained with the standard Richards equation using saturation (a) or pressure (b) as the initial condition

In these simulations we first used the experimentally measured initial water saturation distributions to prescribe initial conditions. We again assumed that initially the sand was everywhere in an imbibition state, consistent with the way in which the flume was packed. Moreover, based on the non-uniform bulk density distribution measured along

the flume (see Figure 2.1), we assigned different values for porosity to each segment of 5 cm along the flume. This approach would account for the heterogeneity in the sand packing. Regarding the initial condition in HYDRUS, we could specify either the water content or the pressure distributions. The latter could be calculated from measured initial saturation values using the main imbibition curve.

Results of the HYDRUS simulations are shown in Figure 2.8. The colored solid lines and dots represent numerical results and experimental data, respectively. Different colors indicate different measurement times. When saturation was used as the initial condition for the heterogeneous flume, it produced unrealistic pressure gradients at the start of the simulations (t=0). On the other hand, when we used a uniform pressure head as the initial condition, simulation results were found to be far from the observed saturation data, given in Figure 2.8b. These inconsistencies could not be resolved due to the lack of information about the initial state of various points along the flume.

The simulation results in Figure 2.8, obtained with the standard Richards equation, deviated substantially from the experimental data in the dry side. Saturations there increased much faster and remained much higher than the measured values. We tried to remedy this situation by modifying the relative permeability curve to generate lower flow rates. For this purpose we increased the value of exponent l in Equation (2.3), while keeping the other parameters as their measured values. Results are shown in Figure 2.9a. It is evident that the redistribution process was now much slower, but that saturations near the contact surface in the dry side were still too high. The only way we could force the simulation results to match the experimental data was to significantly increase the value of the coefficient α of the imbibition curve. With the value of α was increased by a factor 2, good agreement was obtained with the measured saturations, as shown in Figure 2.9b.

Next, the interfacial area model with the generalized Darcy's law was employed. For this model we needed to specify not only the initially measured saturation distribution, but also the initially measured water pressure distribution. Regarding the parameter values, we equalized the porosity φ and the saturated conductivity K_s to their measured values (see Table 2.1). Also, one p^c-S^w-a^{wa} surface was assigned to both sides. The parameter values (γ_1, γ_2, and γ_3) for this surface are given in Table 2.2. Auxiliary simulations showed that the results were not sensitive to changes in the values of the interfacial area flux parameters k^{wa} and Ω. We hence fixed these values to 10^{-17} m^3 s^{-1} and 4000 m^{-1}, respectively, as used in our preliminary simulations. The three remaining parameters were determined by fitting to the data: λ in the generalized

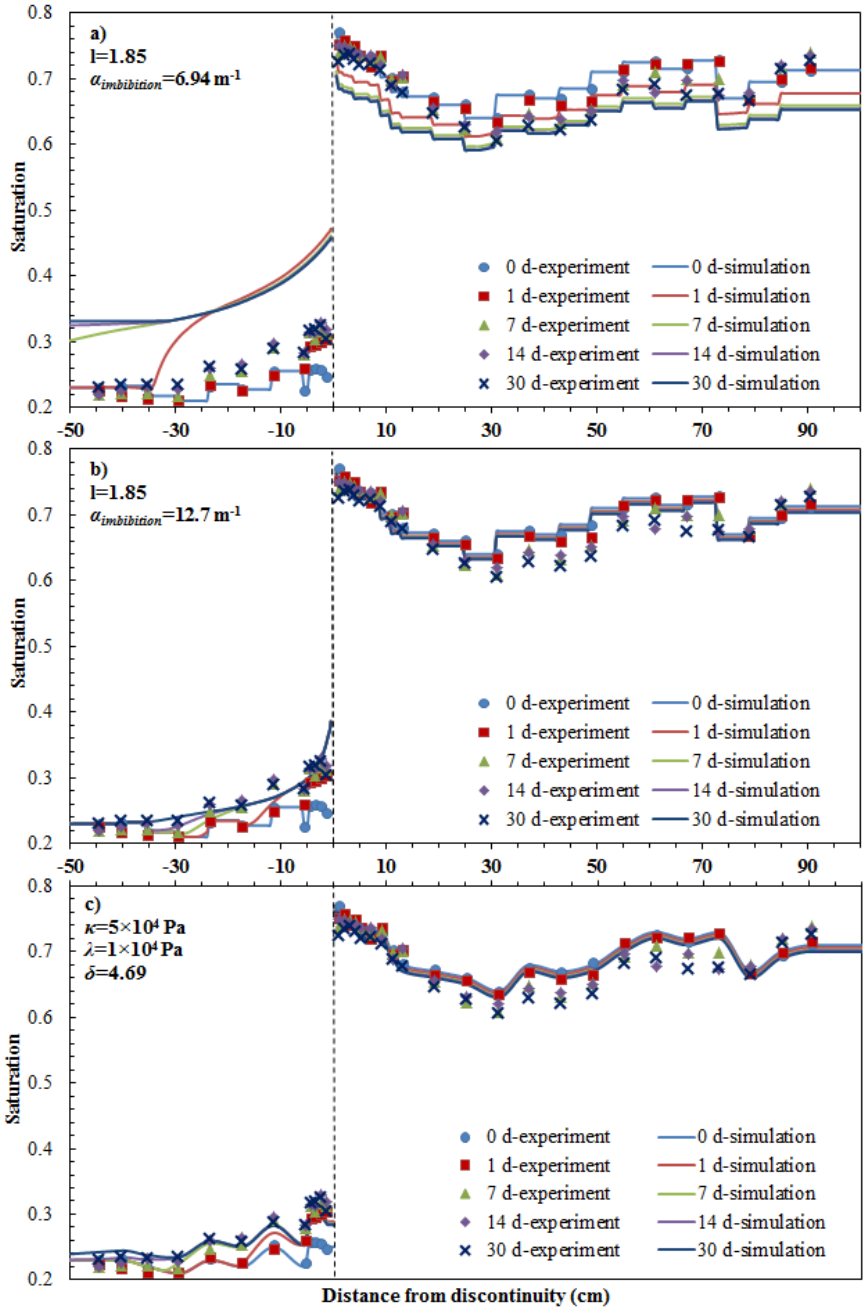

Figure 2.9 Observed saturation profiles and fitted curves using the standard Richards equation with adjusted values of *l* (a), *l* and *α-imbibition* (b), and the interfacial area model (c)

Darcy's equation, Equation (2.9); the exponent δ of the relative permeability function, Equation (2.10); and the coefficient κ of interfacial area production term in Equation (2.13).

Calculated saturation profiles and measured data at different measurement times with the interfacial area model are shown in Figure 2.9c. The model was found to perform best using fitted values of κ=5×10^4 Pa, δ=4.69, and λ=10^4 Pa. Results compared well with the experimental data in the dry side, including the now much slower progression towards equilibrium and the spatial distribution of saturation observed (see Figure 2.9c).

2.5 Discussion, conclusions, and outlook

In this study we have simulated a horizontal water redistribution experiment recently conducted by Feuring et al. (2014). Two different models, the standard Richards equation and an interfacial area model, were employed and compared in terms of their ability to reproduce the experimental data. The Richards equation was used with and without accounting for hysteresis, while for the interfacial area model we used two different formulations for Darcy's law.

As expected, the standard model without hysteresis gives results that were at odds with the observations. In particular, the Richards equation produced a full redistribution of water and the complete disappearance of the saturation discontinuity between the two sides of the experimental setup. The hysteretic Richards model did lead to non-uniform saturation distribution and properly simulate the saturation discontinuity. However, the flow process was found to be much faster than observed, while saturation values in the dry side were severely over-predicted. The differences could be minimized only if unrealistic values were assigned to some of the soil hydraulic parameters.

The interfacial area model produced better agreement with the observed spatial and temporal saturation distributions. To some extent this was expected since this model contains a larger number of parameters. Nevertheless, the fact that the interfacial area model predicted the persistence of the discontinuity in saturation, using the same set of hydraulic properties for both sides, is encouraging.

Compared with having eight possible parameters in the standard model (i.e., φ, K_s, *α-imbibition*, *α-drainage*, *n-imbibition*, *n-drainage*, S_{ir}^{w}, l), the interfacial area model contains eleven parameters (i.e., φ, K_s, γ_1, γ_2, γ_3, δ, S_{ir}^{w}, λ, Ω, k^{wa}, κ). The interfacial area

model hence has more flexibility in fitting the observed data. We must point out that in the case of the standard model, only *α-imbibition* and *l* were determined by fitted the experimental data, and in the case of the interfacial area model, only three parameters, namely δ, λ, and κ were determined. The other parameters were either measured or determined indirectly. Both models were able to describe the experimental data versus time and spatially after optimization. The unrealistic adjustment of some of the values of the soil hydraulic properties needed for the Richards equation, however, is a concern. At the same time, while the interfacial area model provided an excellent description of the data, it is still unclear how realistic the adopted values of κ and λ were. Additional experiments are very much needed to determine the appropriateness of these values.

The detailed comparisons of the classical Richards model, the interfacial area model, and the experimental data provided much insight into the fundamentals of the two models. The introduction of the specific interfacial area eliminated the need for knowing the historical path of water flow and its dynamics. Meanwhile, it is clear that the interfacial area model still contains several assumptions and uncertainties, requiring further evaluation before this model can be more widely applied in practical application of multiphase flow.

Finally, we acknowledge that additional horizontal (and vertical) redistribution experiments and analysis of the interfacial area model are needed in the future. First, like in our study, better controlled experiments must be performed to ensure homogeneous soil packing and direct measurement of initial conditions. This will reduce uncertainties in the experimental data and theoretical analysis. Second, independent experimental measurements should be conducted to obtain the p_c-S_w-a_{wa} surfaces, the interfacial permeability, and the interfacial area production term. Also, several material properties appearing in the interfacial mass balance equation and the generalized Darcy's law should be determined. Finally, long-term experiments should be conducted until full equilibrium is reached.

2.6 Appendix A: Production rate term of the specific interfacial area

A constitutive equation is needed for the rate of production (or destruction) of the specific interfacial area E^{wa}, in Equation (2.8). We know that the interfaces will be created or destroyed if capillary equilibrium is not reached. As explained in Hassanizadeh and Gray (1993a), capillary equilibrium will be disturbed if the

difference in average fluid pressures deviates from the average capillary pressure. This is implicit in the dynamic capillarity equation (Hassanizadeh and Gray, 1993a),

$$p^a - p^w = p^c - \tau \frac{\partial S^w}{\partial t} \tag{A1}$$

where τ, often called the dynamic capillarity coefficient, is a material property which may depend on saturation. One way to parametrize E^{wa} is to relate this parameter to the degree of the deviation from capillarity equilibrium. Thus, we proposed that E^{wa} is proportional to the difference in the amount of interfacial area, a^{wa}, under dynamic and static conditions. Since a^{wa} is a function of S^w and p^c (see Equation (2.5)), we postulate the following linear relationship for E^{wa}

$$E^{wa} = \kappa_1 \left[a^{wa}(S^w, p^a - p^w) - a^{wa}(S^w, p^c) \right] \tag{A2}$$

where κ_1 is a material coefficient. We next expand the function $a^{wa}(S^w, (p^a\text{-}p^w))$ in a Taylor series around p^c to obtain

$$a^{wa}(S^w, p^a - p^w) \approx a^{wa}(S^w, p^c) + \frac{\partial a^{wa}(S^w, p^c)}{\partial p^c}\left(p^a - p^w - p^c \right) \tag{A3}$$

Substitution of Equations (A1) into (A3) and combination of the results with (A2) will lead to

$$E^{wa} = -\kappa_1 \tau \frac{\partial a^{wa}}{\partial p^c}\frac{\partial S^w}{\partial t} = -\kappa \frac{\partial a^{wa}}{\partial p^c}\frac{\partial S^w}{\partial t} \tag{A4}$$

where $\partial a^{wa}/\partial p^c$ can be obtained from Equation (2.5) and κ has to be determined experimentally. In this study, we estimated the value of κ by fitting this parameter to the observed data.

2.7 Appendix B: Gibbs free energy for the specific interfacial area

As explained in the main text, at the contact surface between dry and wet domains, we require continuity in the Gibbs free energy of air-water interfaces. The Gibbs free energy for air-water interfaces G^{wa}, is defined as (e.g., Hassanizadeh and Gray, 1993b; Equation 50b)

$$G^{wa} = A^{wa} - \frac{\sigma^{wa}}{\Gamma^{wa}} \tag{B1}$$

where Γ^{wa} and A^{wa} are the average mass density and macroscopic Helmholtz free energy of air-water interfaces, respectively. The Helmholtz free energy is known to be a function of S^w, a^{wa} and Γ^{wa} (if the latter is not constant). In particular, the macroscopic interfacial tension, Γ^{wa}, is related to the change in the Helmholtz free energy due to a change in the specific interfacial area (see e.g., Hassanizadeh and Gray, 1993b; Equation 26)

$$\sigma^{wa} = -a^{wa}\Gamma^{wa}\left(\frac{\partial A^{wa}}{\partial a^{wa}}\right) \tag{B2}$$

The differential of G^{wa} is found next from Equation (B1) to be

$$dG^{wa} = \frac{\partial A^{wa}}{\partial a^{wa}}da^{wa} + \frac{\partial A^{wa}}{\partial S^w}dS^w - \frac{1}{\Gamma^{wa}}d\sigma^{wa} \tag{B3}$$

where we have considered the average mass density of interfaces to be constant. Substituting Equation (B2) into (B3) and collection of terms results in

$$dG^{wa} = -\frac{d(a^{wa}\sigma^{wa})}{a^{wa}\Gamma^{wa}} + \frac{\partial A^{wa}}{\partial S^w}dS^w \tag{B4}$$

From Hassanizadeh and Gray (1993b) and the definition of coefficient Ω in Equation (2.12), we find:

$$\Omega = -\frac{\Gamma^{wa}a^{wa}}{\sigma^{wa}}\frac{\partial A^{wa}}{\partial S^w} \tag{B5}$$

Substitution of Equation (B5) into (B4) gives:

$$dG^{wa} = -\frac{d(a^{wa}\sigma^{wa})}{a^{wa}\Gamma^{wa}} - \frac{\Omega\sigma^{wa}}{a^{wa}\Gamma^{wa}}dS^w \tag{B6}$$

An approximate integration of this relationship yields:

$$G^{wa} = -\frac{\sigma^{wa}}{\Gamma^{wa}}\left(\ln a^{wa} + \Omega\frac{S^w}{a^{wa}}\right) + G_0 \tag{B7}$$

where G_0 is a constant of integration. Here again we have assumed that Γ^{wa} is a constant. Thus, the continuity in the Gibbs free energy of air-water interfaces across the contact surface requires continuity in $ln a^{wa} + \Omega S^w/a^{wa}$.

Acknowledgements

The first author is funded by the China Scholarship Council. The authors are thankful to Robert Schwartz and two anonymous reviewers for their suggestions and comments that helped to improve the manuscript.

References

Always, F.J., and V.L. Clark. 1911. A study of the movement of water in a uniform soil under artificial conditions. Annual Report 25, p. 246-287, Nebraska Exp. Station, Lincoln, NE.

Biswas, T.D., D.R. Nielsen, and J.W. Biggar. 1966. Redistribution of soil water after infiltration. Water Resour. Res. 2(3): 513–524.

Chen, L. and T.C.G. Kibbey. 2006. Measurement of air-water interfacial area for multiple hysteretic drainage curves in an unsaturated fine sand. Langmuir 22(16): 6874–6880.

Chen, D., L.J. Pyrak-Nolte, J. Griffin, and N.J. Giordano. 2007. Measurement of interfacial area per volume for drainage and imbibition. Water Resour. Res. 43(12): W12504.

COMSOL. 2014. COMSOL Multiphysics 4.4. COMSOL Inc., Burlington, MA, USA.

Dane, J.H., and P.J. Wierenga. 1975. Effect of hysteresis on the prediction of infiltration, redistribution and drainage of water in layered soil. J. Hydrol. 25: 229-242.

Everett, D.H. 1954. A general approach to hysteresis, part 3: A formal treatment of the independent domain model of hysteresis. Trans. Faraday Soc. 50: 1077-1096.

Feuring, T. 2010. Horizontal redistribution of two fluid phases in a porous medium. Stuttgart University, M. Sc thesis.

Feuring, T., J. Braun, B. Linders, G. Bisch, S.M. Hassanizadeh, and J. Niessner. 2014. Horizontal redistribution of two fluid phases in a porous medium: Experimental investigations. Transp. Porous Media. 105(3): 503–515.

Haines, W.B. 1930. Studies in the physical properties of soil. V. The hysteresis effect in capillary properties and the modes of moisture distribution associated herewith. J. Agric. Sci. 20: 97-116.

Hassanizadeh, S.M., M. A. Celia, and H. K. Dahle. 2002. Dynamic effect in the capillary pressure-saturation relationship and its impacts on unsaturated flow. Vadose Zone J. 1: 38-57.

Hassanizadeh, S.M., and W.G. Gray. 1990. Mechanics and thermodynamics of multiphase flow in porous media including interphase boundaries. Adv. Water Resour. 13(4): 169–186.

Hassanizadeh, S.M., and W.G. Gray. 1993a. Thermodynamic basis of capillary pressure in porous media. Water Resour. Res. 29(10): 3389–3405.

Hassanizadeh, S.M., and W.G. Gray, 1993b. Toward an improved description of the physics of two-phase flow. Adv. Water Resour. 16(1): 53–67.

Held, R.J., and M.A. Celia. 2001. Modelling support of functional relationships between capillary pressure, saturation, interfacial area and common lines. Adv. Water Resour. 24(2001): 325–343.

Jaynes, D.B. 1984. Comparison of soil-water hysteresis models. J. Hydrol. 75: 287-299.

Joekar-Niasar, V., S.M. Hassanizadeh, and A. Leijnse. 2007. Insights into the relationships among capillary pressure, saturation, interfacial area and relative permeability using pore-network modeling. Transp. Porous Media. 74(2): 201–219.

Joekar-Niasar, V., and S.M. Hassanizadeh. 2011. Specific interfacial area: The missing state variable in two-phase flow equations? Water Resour. Res. 47(5): W05513.

Joekar-Niasar, V., and S.M. Hassanizadeh. 2012. Uniqueness of specific interfacial area-capillary pressure-saturation relationship under non-equilibrium conditions in two-phase porous media flow. Transp. Porous Media. 94(2): 465-486.

Karadimitriou, N.K., S.M. Hassanizadeh, V. Joekar-Niasar, and P.J. Kleingeld. 2014. Micro-model study of two-phase flow under transient conditions: Quantifying effects of specific interfacial area. Water Resour. Res. 50(10): 8125-8140.

Kona, S. 1997. Experimental investigation of horizontal redistribution of water in unsaturated porous media. University of Minnesota, M. Sc thesis.

Kool, J.B., and J.C. Parker. 1987. Development and evaluation if closed-form expression for hysteretic soil hydraulic properties. Water Resour. Res. 23(1): 105-114.

Lenhard, R.J., and J. C. Parker. 1991. Comparing simulated and experimental hysteretic two-phase transient fluid flow phenomena. Water Resour. Res. 27(8): 2113–2124.

Luckner, L., M. Th. van Genuchten, and D.R. Nielsen. 1989. A consistent set of parametric models for the two-phase flow of immiscible fluids in the subsurface. Water Resour. Res., 25(10): 2187-2193.

Marshall, F. 2009. Numeric solution of Philip's redistribution problem. Stuttgart University, M. Sc thesis.

Mualem, Y. 1974. A conceptual model of hysteresis. Water Resour. Res. 10: 514-520.

Mualem, Y. 1984. A modified dependent domain theory of hysteresis. J. Soil Sci. 137: 283-291.

Niemet, M. R., M. L. Rockhold, N. Weisbrod, and J. S. Selker. 2002. Relationships between gas-liquid interfacial surface area, liquid saturation, and light transmission in variably saturated porous media. Water Resour. Res. 38(8): 1135.

Niessner, J., and S. M. Hassanizadeh. 2008. A model for two-phase flow in porous media including fluid-fluid interfacial area. Water Resour. Res. 44(8): W08439.

Parker, J.C., and R.J. Lenhard. 1987. A model for hysteretic constitutive relations governing multiphase flow: 1. Saturation pressuer relations. Water Resour. Res. 23: 2187-2196.

Peck, A.J. 1971. Redistribution of soil water after infiltration. Soil Res. 9(2): 59–71.

Pham, H.Q., D.G. Fredlund and S.L. Barbour. 2005. A study of hysteresis models for soil-water characteristic curves. Can. Geotech. J. 42: 1548-1568.

Philip, J.R. 1964. Similarity hypothesis for capillary hysteresis in porous materials. J. Geophys. Res. 69(8): 1553-1562.

Philip, J.R. 1991. Horizontal redistribution with capillary hysteresis. Water Resour. Res. 27(7): 1459-1469.

Polouvassilis, A. 1962. Hysteresis of pore water – An application of the concept of independent domains. J. Soil Sci. 92: 405-412.

Polouvassilis, A., and W.M. El-Ghamry. 1978. The dependent domain theory applied to scanning curves of any order in hysteretic soil water renationships. J. Soil Sci. 126: 1-8.

Pop, I.S., C.J. van Duijn, J. Niessner, and S.M. Hassanizadeh. 2009. Horizontal redistribution of fluids in a porous medium: The role of interfacial area in modeling hysteresis. Adv. Water Resour. 32(3): 383–390.

Šimůnek, J., M. Šejna, H. Saito, M. Sakai, and M.T. van Genuchten. 2009. The HYDRUS-1D software package for simulating the one-dimensional movement of water, heat and multiple solutes in variably-saturated media.

Scott, P.S., G.J. Farquhar, and N. Kouwen. 1983. Hysteretic effects on net inffiltration. Advances in Infiltration 11-83: 163-170, Am. Soc. Agric. Eng., St. Joseph, MI.

Staple, W.J. 1969. Comparison of computed and measured moisture redistribution following infiltration. Soil Sci. Soc. Am. J. 33(6): 840–847.

Talsma, T. 1974. The effect of initial moisture content and infiltration quantity on redistribution of soil water. Soil Res. 12(1): 15–26.

Topp, G.C. 1971. Soil-water hysteresis: The domain theory extended to pore interaction conditions. Soil Sci. Soc. Am. Proc. 35: 219-225.

Vachaud, G. 1969. Étude d'une redistribution après l'arrêt d'une infiltration horizontale. Int. Symp. Water in Unsaturated Soils, Wageningen, June 19-25, 1969. Int. Assoc. of Sci. Hydrology and UNESCO, Belgium.

Vachaud, G., and J. Thony. 1971. Hysteresis during infiltration and redistribution in a soil column at different initial water contents. Water Resour. Res. 7(1): 111–127.

van Genuchten, M.T. 1980. A closed-form equation for predicting the hydraulic conductivity of unsaturated soils. Soil Sci. Soc. Am. J. 44(5): 892–898.

Werner, A.D. and Lockington. 2006. Artificial pumping errors in the Kool-Parker scaling model of soil moisture hysteresis. J. Hydrol. 325(1–4): 118–133.

Youngs, E.G. 1958. Redistribution of moisture in porous materials after infiltration: 2. Soil Sci., 86(4): 202–207.

Youngs, E.G., and A. Poulovassilis. 1976. The different forms of moisture profile development during the redistribution of soil water after infiltration. Water Resour. Res. 12(5): 1007–1012.

Chapter 3

Analysis of the Hysteretic Hydraulic Properties of Unsaturated Soil

Submitted to Vadose Zone Journal, Zhuang, L., C.R. Bezerra, S.M. Hassanizadeh, and M.Th. van Genuchten.

Abstract

Knowledge of the unsaturated soil hydraulic properties is essential for modelling water flow and solute transport processes in variably-saturated subsurface systems. There exist various experimental setups for the measurement of such properties. We have devised a relatively simple setup for simultaneous measurement of the water retention and unsaturated hydraulic conductivity curves using multistep flux (MSF) and multistep outflow (MSO) experiments. Our focus was especially on medium- and coarse-textured sands having relatively narrow particle-size distributions, which find their manifestation in the van Genuchten-Mualem (VGM) hydraulic parameter *n*. We also measure the soil properties using the HYPROP evaporation method. MSF and MSO results showed excellent agreement, but deviated slightly from independent data obtained with the HYPROP. The values of VGM parameter *n* for the sands we used were as high as 15. Some discrepancy was found between the MSO, MSF and HMS retention data, presumably because of the assumed linear distribution of the water content versus depth in the HMS approach.

Abbreviations: MSF, Multistep flux method; MSO, Multistep outflow method; VGM, van Genuchten-Mualem model; HMS, HYPROP measurement system

3.1 Introduction

Quantifying the unsaturated soil hydraulic properties is essential to the understanding and modeling of fluid flow and contaminant transport in the vadose zone, as well as for other variably-saturated multiphase flow systems. The constitutive relationships for air-water systems generally involve the water content, θ, as a function of the pressure head, h, and the hydraulic conductivity, K, as a function of pressure head or water content. A range of laboratory methods have been developed over the years for estimating the soil hydraulic properties (cf. Klute, 1986; van Genuchten et al., 1997; Dane and Hopmans, 2002; Durner and Lipsius. 2005). This includes not only direct measurement of θ and/or K at specific pressure heads or water contents, but also the use of inverse procedures to estimate the complete $\theta(h)$ and/or $K(\theta)$ curves (Durner et al., 1999; Hopmans et al., 2002).

Following Becher (1970) and Wind (1968), the evaporation method is a widely-used method to water retention and the unsaturated hydraulic conductivity simultaneously. The method has seen many improvements over the years (e.g., Halbertsma, 1996; Wendroth et al., 1993, Peters and Durner, 2005; Schindler and Muller, 2006; Peters et al. 2015), leading to a semi-automated version (referred to here as the HYPROP measurement system, HMS) that is now being commercialized by Decagon Devices (Pullman, WA) and UMS GmbH (Munich, Germany). The method uses values of the pressure head measured at two depths within a 5-cm soil sample, along with the weight of the soil sample during the evaporation process, to estimate the soil hydraulic data. While very reliable results have been reported for the HMS approach, one inherent drawback of evaporation methods is that results hold only for the drainage branches of the soil hydraulic properties.

An alternative simultaneous direct approach is the multistep flux (MSF) method based on a vertically uniform flow (Dirksen and Matula, 1994; Weller et al., 2011; Weller and Vogel, 2012). The method allows measurements of $K(h)$ assuming unit pressure gradient conditions during steady-state downward flow in a soil column. Water inflow and outflow rates are measured and adjusted to be the same, while pressure heads are also adjusted to be the same when measured at two vertical positions. The fluid flow rate becomes then equal to the unsaturated hydraulic conductivity, K, at the measured pressure head, h. Repeating the measurements at various flow rates and corresponding pressure heads will produce the desired hydraulic data points.

In this study, we constructed a relatively simple setup using a small cell. We report here the measured hysteretic hydraulic properties of two soil samples having relatively narrow pore-size distributions, and compare results with the more standard hydrostatic hanging-water column approach, carried out here in the form of multistep outflow (MSO) experiments. The studies were motivated in part to have reliable soil hydraulic data for more theoretical studies of hysteresis phenomena using alternative thermodynamics-based interfacial area approaches (Zhuang et al., 2016b). Moreover, there have been a few experimental and numerical studies carried out on clean sands (e.g., Weller et al., 2011; Weller and Vogel, 2012; Bezerra et al. 2016; Mahmoodlu et al., 2016; Wang et al., 2016; Zhuang et al., 2016a).

3.2 Materials and methods

3.2.1 Sand materials

We investigated two types of sands. One sand, labeled as S1, was obtained from a sand mining site (Sibelco, Antwerp, Belgium) with particles ranging from 0.1 to 0.5 mm. The other sand (S2), having grain sizes from 0.1 to 1 mm, was obtained from a riverbed. Prior to use, the two sandy soils were rinsed with deionized water and then air dried. Saturated hydraulic conductivities of the two samples were measured using a constant-head method (Reynolds et al., 2002) with the same sand cell holder as used for the multistep outflow and multistep flux experiments (Figure 3.1). Selected properties of the two sand samples are shown in Table 3.1.

Table 3.1 Properties of the two samples in experiments

Properties	**S1**	**S2**
Mean particle diameter, d_{50} (mm)	0.20	0.28
Particle density, ρ_s (g cm^{-3})	2.56	2.55
Saturated conductivity, (cm h^{-1})	61.2	75.6
Average porosity, φ, (-)	0.39	0.36

3.2.2 Multistep outflow (MSO) experiments

Figure 3.1 shows a schematic of our MSO experimental setup. A custom-built Plexiglas cell for holding sand sample was employed for the multistep outflow

experiments. The dimensions of cell were 3 cm (height) by 3 cm (length) by 2 cm (width). A valve at the top of sandbox (Valve 1) was connected to a balloon filled with moist air to keep constant atmospheric pressure. At the bottom of sand cell, a 5μm hydrophilic nylon membrane was held by a stainless-steel porous plate to serve as a capillary barrier. The water reservoir at the bottom of the setup was connected to a small hanging water column; the latter was used to control the pressure head at the outlet. Water in the small hanging column could overflow during drainage, while extra water was added to keep the water head in the column constant during imbibition. Silicone tapes were used at all joints to avoid any leakage.

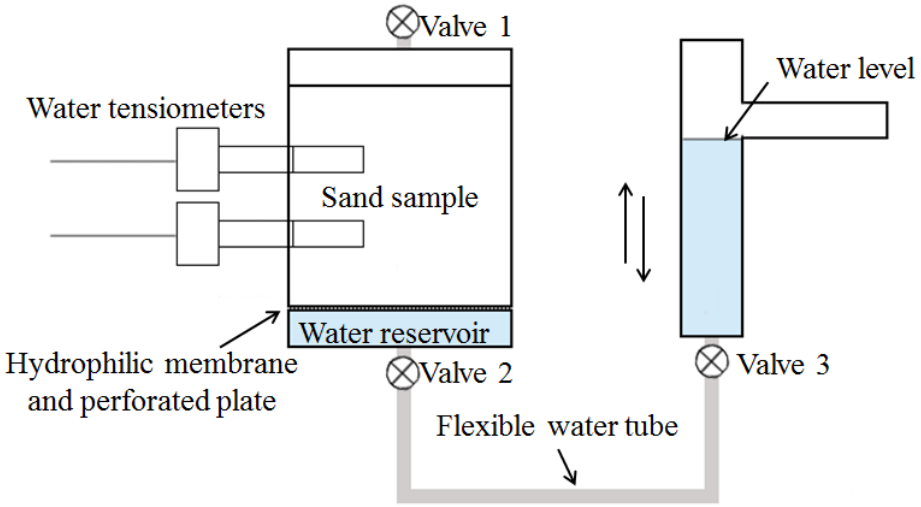

Figure 3.1 Schematic view of the experimental setup for the multistep outflow (MSO) experiments

Two mini-tensiometers (Rhizo Instruments, Wageningen, Netherlands) were installed at depths of 1 and 2 cm in the sand sample cell. The tensiometers consisted of a ceramic cup, 1 cm long and 4 mm in diameter, and a small pore pressure transducer. An air permeable but water impermeable plastic hollow fiber was used to connect the ceramic cup to a vacuum in order to remove air from the tensiometers. Prior to use, the tensiometers were saturated with deionized water, while during the experiments, tensiometers were always connected to an automatic vacuum system. This ensured that the tube between the ceramic cup and the transducer remained filled with water. The pressure transducers were connected to a CR1000 data logger (Campbell Scientific, Shepshed, UK). Tensiometer readings were collected every 5 min.

The water content in the middle of the sand sample was measured using gamma ray transmission method. When a beam of gamma radiation passes through a sample of thickness x, the transmission of photons can be described using Beer-Lambert's law, which for an unsaturated soil sample can be written as:

$$I = I_0 \exp(-\mu_s x_s - \mu_w x_w) \tag{3.1}$$

where I and I_0 are measured and corresponding reference intensities, respectively, μ_s and μ_w (L^{-1}) are the soil and water attenuation coefficients, and x_s and x_w denote the length of the soil and water along the path of the gamma-ray beam. Values of the porosity (φ) of the sand and its water content (θ) can be calculated from x_s and x_w using

$$\varphi = \frac{x - x_s}{x} \quad \text{and} \quad \theta = \frac{x_w}{x} \tag{3.2}$$

respectively where x is the total thickness of the soil sample (i.e. 2 cm, being the width of our experimental setup).

In our study, we used a dual energy gamma ray system. The gamma-ray sources consisted of ^{241}Am, with an energy peak of 59 keV, and ^{137}Cs, with an energy peak of 662 keV. The diameter of the gamma-ray beam was 6 mm. Measured intensities hence were average values over the cross-section of the beam and the sample thickness x.

The attenuation coefficients μ_s and μ_w for both ^{241}Am and ^{137}Cs were measured and calculated beforehand. Details of the calibration procedures and the dual gamma ray system are given by Fritz (2012). We chose the intensities of the empty cell as the reference I_0 for both ^{241}Am and ^{137}Cs. Intensities for ^{241}Am and ^{137}Cs can be collected simultaneously for each gamma-transmission measurement, while x_s and x_w can be calculated from Equation (3.1), written for Am and Cs separately. Once x_s and x_w are know the sand porosity (φ) and water content (θ) can be calculated for every gamma-transmission measurement. Water contents were measured after the equilibrium of the soil sample at each imposed water level (and hence pressure head).

The experimental setup was first mounted with the bottom reservoir and the cell full of water and without the top lid. Some deionized and degassed water was used to minimize air entrapment. The cell was packed by pouring dry sand continuously into the water filled cell through a funnel, and regularly tapping the sand. A small comb was used to mix the sand in water to avoid layering. The top cover was installed after packing the sand uniformly. All experiments were conducted at a constant-temperature room at 21±0.5ºC.

3.2.3 Multistep flux (MSF) experiments

We modified the MSO setup for performing multistep outflow experiments. This allowed us to measure unsaturated conductivities directly and the water retention curve. Water flow in the porous medium was described using the standard Darcy-Buckingham equation

$$q = -K(\theta)\left(\frac{\partial h}{\partial x} - 1\right) \tag{3.3}$$

where q is fluid flux, and x is vertical spatial coordinate. For unit-gradient flow in the vertical direction (i.e., when $\partial h/\partial x=0$), the flux becomes equal to the hydraulic conductivity, $K(h)$. Different hydraulic conductivity values can be obtained by changing the inflow rate and the height of the hanging water column (and thus changing h).

A sketch of the MSF experimental setup is shown in Figure 3.2. Six injection needles (two in the lateral direction and three in the longitudinal direction) were used to obtain a spatially uniform water inflow rate. Each needle was connected to a tube with an inner diameter of 2 mm. The six tubes were connected to a peristaltic pump that controlled the injected flow rate. The tips of needles were contacted to a 200-μm hydrophilic nylon membrane (hydrophilic membrane 1 in Figure 3.2) to establish a homogenous water flow rate into the sand sample.

A continuous water flow was established during the experiments, i.e., starting from primary drainage, to scanning imbibition, and then to main drainage. After packing the saturated sand samples into the cell, a water flow rate, slightly smaller than the measured saturated hydraulic conductivity (as obtained with the constant-head method), was applied to the top of the sample. The hanging water column was then kept at the same level as the bottom of the sand sample.

Readings of the two tensiometers were collected continuously and outflow was measured when the readings of two tensiometers became identical, in which case the measured outflow was assumed to be equivalent to the value of hydraulic conductivity at the pressure head obtained from the tensiometer readings. The process was reversed when the water flow rate became too small for the peristatic pump. The level of the hanging column after each step was moved to a new elevation prior to decreasing the flow rate using the pump during drainage, while it was in an opposite manner during imbibition.

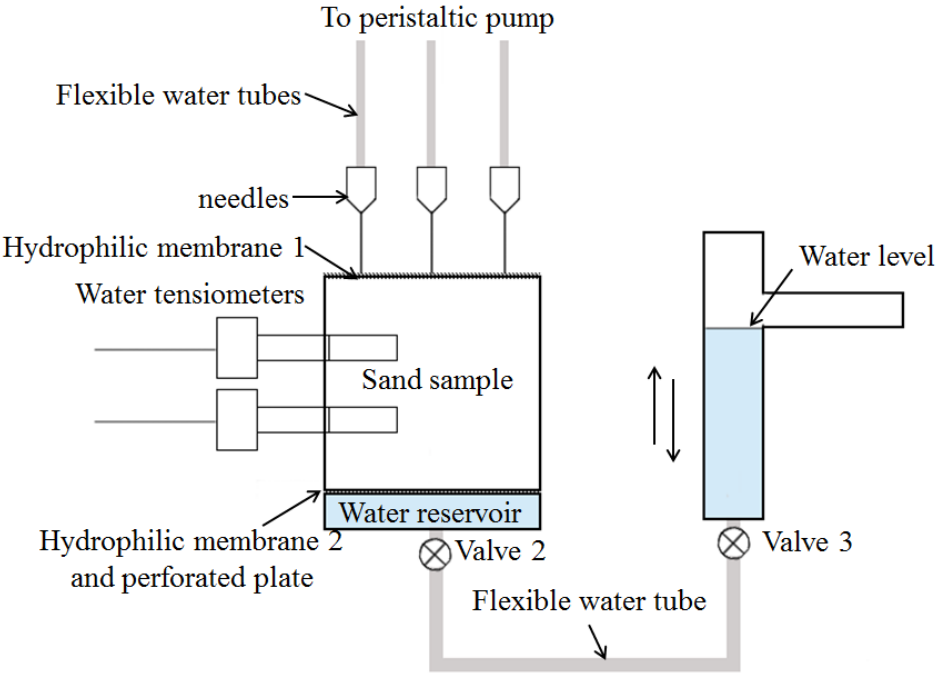

Figure 3.2 Schematic view of the experimental setup for the multistep flux (MSF) experiments

3.2.4 HYPROP experiments

We employed the HYPROP commercial device (UMS GmbH, Munich, Germany) to carry out the HMS evaporation experiments. Saturated HMS soil samples (250 cm^3, 5 cm in height) were for this purpose sealed at the bottom and exposed at the top for evaporation. Values of the pressure head were monitored continuously at two depths (1.25 and 3.75 cm). The weight loss of the sample was measured simultaneously, so that values of the water content would be calculated volumetrically. The geometric mean values of measured water pressure heads at two depths were calculated. At any given time, the values of water content, water pressure head and hydraulic conductivity were calculated using the HYPROP software as documented by Pertassek et al. (2015).

3.3 Soil hydraulic functions

Measured soil water retention and unsaturated conductivity data were analysed in terms of the van Genuchten-Mualem (VGM) equations (van Genuchten, 1980) given by:

$$\theta(h) = \theta_r + \frac{\theta_s - \theta_r}{\left[1 + |\alpha h|^n\right]^m} \tag{3.4}$$

$$K(\theta) = K_s (S_e)^l \left[1 - \left(1 - S_e^{1/m}\right)^m\right]^2 \tag{3.5}$$

$$S_e = \frac{\theta - \theta_r}{\theta_s - \theta_r} \tag{3.6}$$

where θ_s and θ_r are the saturated water content and residual water content, respectively, S_e is effective saturation, K_s is the saturated hydraulic conductivity, α, m, n and l are fitting parameters, with m=1-1/n.

3.4 Results and discussion

Three replicates were conducted for all experiments. Because of the close overlap of the replicates, only one measurement set is shown here for each sand.

3.4.1 MSO and MSF experiments

Water retention data of the two sands as obtained with the multistep outflow (MSO) experiments are shown in Figures 3.3a and 3.3b. The different symbols represent MSO measured retention data during primary drainage, main imbibition and main drainage processes. The shapes of the retention curves are very much consistent with the particle size distribution ranges of the two sands; the retention curve of sand S1 with its narrow particle distribution range is flatter for both drainage and imbibition processes.

Figure 3.3 also includes the VGM retention functions (dashed lines) as fitted to the experimental data. The fitted parameter values are listed in Table 3.2. The residual water content θ_r was iteratively fitted to the same value for all MSO experiments. The saturated water content θ_s for main drainage and imbibition curves was fixed at a value less than porosity due to air entrapment (leading to a non-zero residual air content).

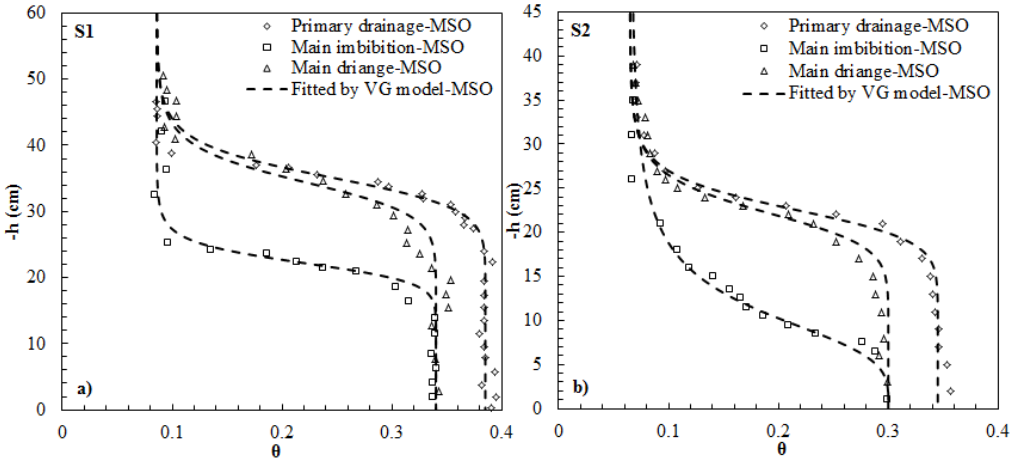

Figure 3.3 Water retention data obtained with MSO experiments for sands S1 and S2

Figures 3.4a and 3.4b show observed water retention data of the two sands as measured using the MSF experiments. Different symbols are used for the primary drainage, scanning imbibition and main drainage data points. Fitted VGM curves of the MSF experiments are shown by solid lines. Also included for comparison are the fitted curves of the MSO experiments (dashed lines; the same curves as in Figure 3.3). The retention curves of sand S1 obtained from the MSF method lie slightly lower than the MSO data for both drainage and imbibition. It is probably because of micro heterogeneity and non-uniform water configuration in the sand sample during drainage process, and non-equilibrium dynamic effect. This deviation has also been observed and discussed by Weller et al. (2011).

Unsaturated hydraulic conductivities obtained using MSF method are shown in Figures 3.4c and 3.4d. The conductivity data versus water content showed very little or no hysteresis between the main drainage, primary wetting and main wetting branches (Poulovassilis, 1969; Tzimas, 1979). Unsaturated conductivities of the two sands at high water content were close to the saturated conductivity as measured with the constant-head method.

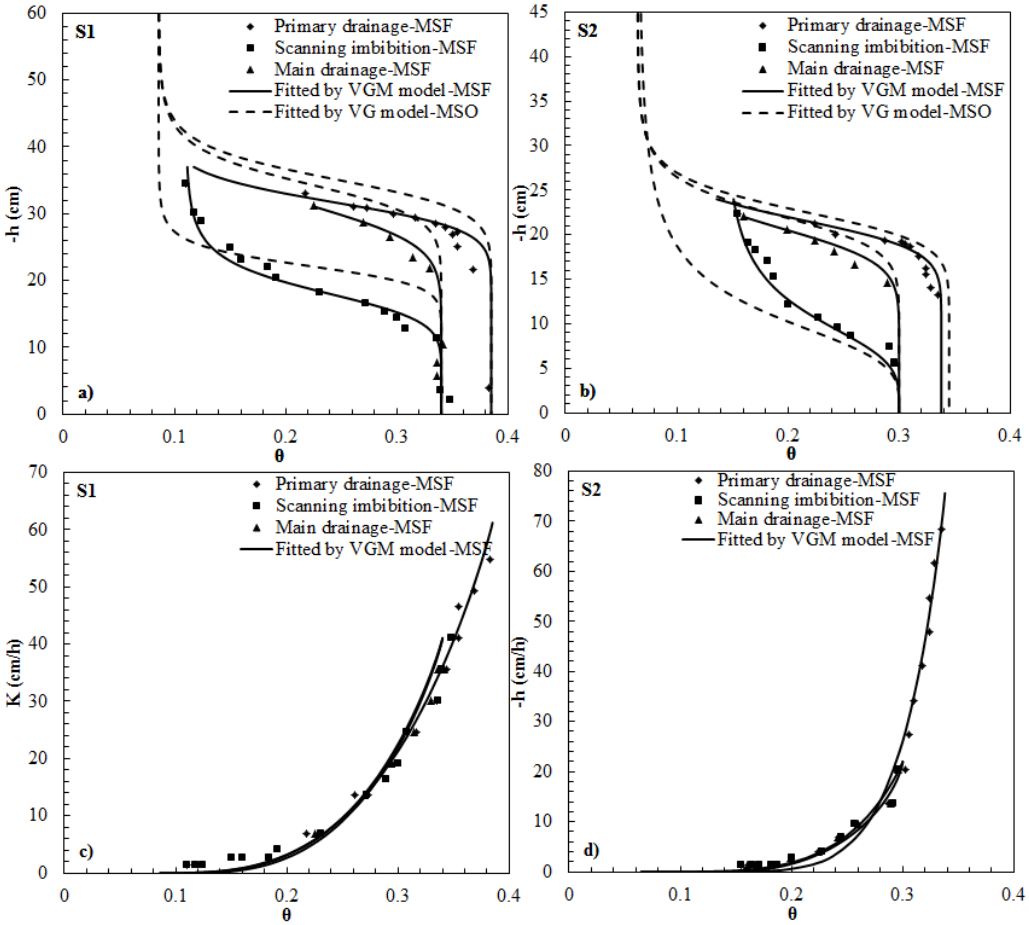

Figure 3.4 Water retention data (top) and unsaturated hydraulic conductivities (bottom) obtained with the multistep flux (MSF) experiments for sands S1 and S2.

We used the VGM model to obtain a simultaneous fit of the MSF measured water retention and unsaturated conductivity data. Resulting curves are shown as solid lines in Figure 3.4. Values of the residual water content θ_r for primary and main drainage processes were fixed at those obtained with the MSO experiments, while its value was fitted for the scanning imbibition process. The value of saturated conductivity K_s for primary drainage was taken to be the value measured using the constant-head method, while K_s for the scanning and main drainage branches was fixed at the largest measured value. The fitted values are shown in Table 3.2. Small differences in the fitting parameter values existed between the MSO and MSF data points of primary and main drainage processes. The values of the pore connectivity parameter l showed some

variation between the various curves. However, fixing the value at 0.5 as suggested by Mualem (1976) did not have a major effect on the plotted curves, except for the MSF primary drainage and scanning imbibition curves of S1 and S2 (results not further shown here). This was not overly surprising since many (not all) of the soils used in the analysis by Mualem were relatively coarse-textured disturbed porous media like in our study.

Table 3.2 Values of the fitted VGM hydraulic parameters for the different experiments

Sample	**Experiment**	α (cm^{-1})	n (-)	θ_r ($cm^3\,cm^{-3}$)	θ_s ($cm^3\,cm^{-3}$)	K_s ($cm\,h^{-1}$)	l
S1	Primary drainage, MSO	0.0284	14.5	0.086	0.385	-	-
	Main imbibition, MSO	0.0451	14.8	0.086	0.340	-	-
	Main drainage, MSO	0.0288	13.5	0.086	0.340	-	-
	Primary drainage, MSF	0.0315	15.1	0.0868	0.385	61.2	0.81
	Scanning imbibition, MSF	0.0553	8.0	0.110	0.340	41.0	0.40
	Main drainage, MSF	0.0322	10.0	0.086	0.340	41.0	0.82
	Primary drainage, HMS	0.0219	10.0	0.047	0.410	61.2	0.20
S2	Primary drainage, MSO	0.0442	12.2	0.065	0.345	-	-
	Main imbibition, MSO	0.1003	3.9	0.065	0.300	-	-
	Main drainage, MSO	0.0453	11.1	0.065	0.300	-	-
	Primary drainage, MSF	0.0460	12.2	0.065	0.338	75.6	4.50
	Scanning imbibition, MSF	0.1007	4.0	0.141	0.300	22.0	-0.50
	Main drainage, MSF	0.0480	10.0	0.065	0.300	22.0	2.00
	Primary drainage, HMS	0.0421	5.9	0.044	0.363	75.6	0.66

3.4.2 Comparison with the Hyprop evaporation data

We compared some of the MSO and MSF primary drainage data with the Hyprop (HMS) evaporation experiments. Figures 3.5a and 3.5b show that the HMS produced very well-defined smooth retention curves, but with somewhat higher saturated water contents as compared to the MSO data, as well as lower residual water contents. The primary drainage curve for sand S1 obtained with the HMS evaporation method lies higher than the curve obtained with MSO method over the entire water content range (Figure 3.5a), while the data for sand S2 show only slight difference mostly in the drier water content range. Similar discrepancies between HMS data and especially pressure plate data were also noted by Schelle et al. (2013) for their coarse-textured samples. They offered three possible explanations for the deviations. One could be the different saturated water contents of the sand samples used for the two methods. Another possibility may be cooling effects during the evaporation experiments, which could have affected the tensiometer readings. The entire retention curve is shifted to the right (larger pressure head value). A third explanation could be possible dynamic non-equilibrium effects during the evaporation experiments as discussed by Diamantopoulos and Durner (2012) and Hassanizadeh et al. (2002), among others. We conclude that more studies of the observed differences may be needed.

Unsaturated conductivities obtained with MSF and HMS evaporation experiments are shown in Figures 3.5c and 3.5d. Values of unsaturated conductivity in this case are presented using a log scale. Results indicate several order of magnitude difference between the measured unsaturated hydraulic conductivities using the two methods were quite different. Unsaturated conductivities data points obtained with the evaporation method were mainly in the dry range, while MSF experiments measured unsaturated conductivities mainly in the wet range. Our results are consistent with other studies showing that HMS applications to soils having very narrow pore-size distributions (as reflected by van Genuchten n values above 5 or even 10) may still produce very reliable results for water retention, but not for near-saturated hydraulic conductivity values (Peters et al., 2015; Bezerra et al., 2016).

Figure 3.5 includes the fitted VGM equations for the MSF and HMS measured soil water retention and hydraulic conductivity curves. Fitted parameter values are reported in Table 3.2. Values of the saturated conductivity K_s of the two sands were fixed at those measured using the constant-head method. The fitted curves for HMS data are shown as solid lines in Figure 3.5. The fitted HMS curves showed excellent agreement with the retention data, but not with the unsaturated conductivity measurements. The

MSO experiments produced mostly higher values of the parameters α, n and θ_r as compared to the HMS experiments.

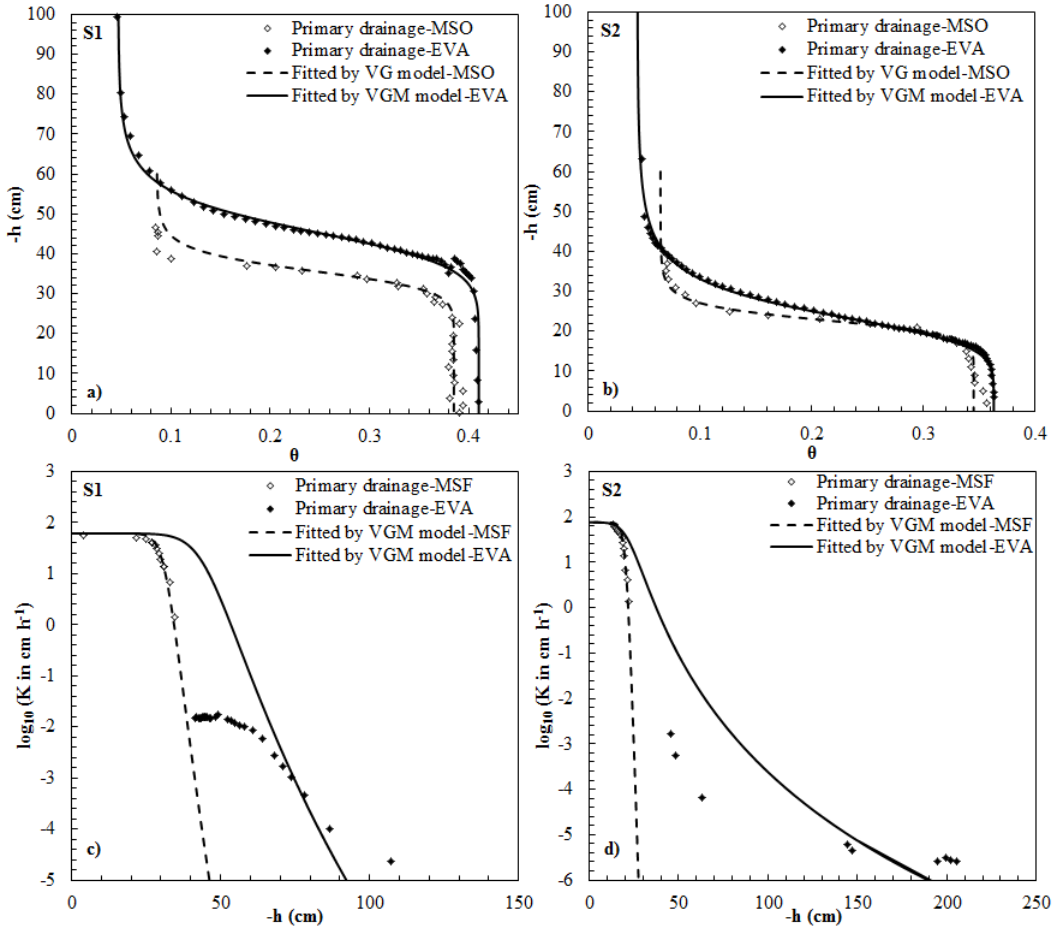

Figure 3.5 Measured and VGM fitted water retention data (top) and unsaturated hydraulic conductivity (bottom) curves obtained with the MSO and HMS evaporation experiments during primary drainage for sands S1 (left figures) and S2 (right figures).

We conclude by noting that some of the differences between the MSO, MSF and evaporation experiments may have been due to differences in measured water contents caused by different averaging volumes. Water contents in MSO and MSF experiments were measured using gamma transmission, in which case water contents were calculated based on the average volume of the gamma source opening area (6 mm in diameter) and the sample width (2 cm). By comparison, water contents during the

evaporation experiments were averaged based on the whole volume of the sample rings (250 cm^3; 5 cm in depth). Moreover, due to the narrow particle size distributions (especially for sand S1), the moisture front during evaporation becomes very sharp, leading to large differences between the water contents in the upper and lower parts of the sample. Such a situation may compromise the linearization assumptions in the HMS evaporation approach (Peters et al., 2015).

3.5 Concluding remarks

In this study, we used three laboratory methods to characterize the unsaturated soil hydraulic properties of two sands having relatively narrow particle size distributions. A small custom-built cell or box was developed to conduct multistep outflow (MSO) and multistep flux (MSF) experiments, while the commercial HYPROP (HMS) system was used for the evaporation experiments. Both drainage and imbibition curves could be obtained using MSO and MSF methods. But, the HMS method provides primary drainage curves only. The hysteretic retention data obtained with MSO and MSF experiments showed good agreement with each other for the primary drainage and main imbibition processes. MSF-measured unsaturated conductivities did not show distinct hysteretic behavior; the values for primary drainage, scanning imbibition and main drainage processes showed very little difference when plotted versus the water content.

We also compared the MSO and MSF measured hydraulic data with HMS results. Some discrepancy was found between the MSO and HMS retention data, presumably because of the assumed linear distribution of the water content versus depth in the HMS approach. This assumption may not be valid for our porous media having very narrow particle size distributions. Unsaturated conductivities using the HMS evaporation experiments were furthermore confined to the very dry range. Independent saturated conductivity measurements hence may be critical to obtain a good description of the complete hydraulic conductivity curve. Additional numerical and experimental studies may be needed to further clarify these issues.

Acknowledgement

The first author would like to thank the China Scholarship Council (No. 201206380076) for their financial support. The third author has received funding from

the European Research Council under the European Union's Seventh Framework Program (FP/2007-2013)/ERC Grant Agreement No. 341225.

References

Becher, H.H. 1971. Ein Verfahren zur Messung der ungesattigten Wasserleitfahigkeit, Z. Pflanzenernaehrung u. Bodenkd., 128: 1– 12,

Bezerra, C.R., L. Zhuang, S. M. Hassanizadeh, M.C. Barbosa, and M.Th. van Genuchten. Further tests of the Hyprop evaporation method for estimating the unsaturated soil hydraulic properties, Vadose Zone J., submitted.

Burdine, N. 1953. Relative permeability calculations from pore size distribution data. J. Pet. Technol. 5(3): 71–78.

Dane, J.H., and J.W. Hopmans. 2002. Water retention and storage: laboratory. p. 675–720. *In* Dane, J.H., Topp, G. (eds.), Methods of Soil Analysis: Part 4 Physical Methods. Soil Science Society of America, Madison, WI.

Diamantopoulos, E., and W. Durner. 2012. Dynamic nonequilibrium of water flow in porous media: a review. Vadose Zone J. 11(3).

Dirksen, C., and S. Matula. 1994. Automatic atomized water spray system for soil hydraulic conductivity measurements. Soil Sci. Soc. Am. J. 58: 319–325.

Durner, W., and K. Lipsius. 2005. Determining soil hydraulic properties. In: M.G. Anderson and J.J. McDonnell (eds), Encyclopedia of Hydrological Sciences. John Wiley & Sons, Chichester, UK. p. 1121–1144.

Durner, W., B. Schultze, and T. Zürmuhl. 1999. State-of-the-art in inverse modeling of inflow/outflow experiments. In: M.Th. van Genuchten, F.J. Leij, and L. Wu. (eds), Characterization and Measurement of the Hydraulic properties of Unsaturated Porous Media, Part 1, University of California, Riverside, CA. , p. 661-682.

Fritz, S. 2012. Experimental investigations of water infiltration into unsaturated Soil - analysis of dynamic capillarity effects. MSc thesis, Stuttgart University.

Halbertsma, J. 1996. Wind's evaporation method; determination of the water retention characteristics and unsaturated hydraulic conductivity of soil samples. Possibilities, advantages and disadvantages, European Workshop on Advanced Methods to Determine Hydraulic Properties of Soils, Thurnau, Germany, 10–12 June 1996, Department of Hydrology, University of Bayreuth, 107 pp.

Hassanizadeh, S.M., M.A. Celia, and H.K. Dahle. 2002. Dynamic effect in the capillary pressure-saturation relationship and its impacts on unsaturated flow. Vadose Zone J. (1): 38–57.

Hopmans, J.W., J. Šimůnek, N. Romano, and W. Durner. 2002. Inverse Modeling of Transient Water Flow. In: J. H. Dane and G. C. Topp (eds.), Methods of Soil Analysis, Part 1, Physical Methods, Third edition, p. 963-1008, SSSA, Madison, WI.

Klute, A. (ed.), Methods of Soil Analysis, part 1, Physical and Mineralogical Methods, Agronomy 401 9(1): 1025-1054. 2nd ed., Am. Soc. Agron., Madison, WI. 402.

Mahmoodlu, M.G., A. Raoof, T. Sweijen, and M. Th. van Genuchten. 2016. Effects of sand compaction and mixing on pore structure and the unsaturated soil hydraulic

properties. Vadose Zone J. 15(8).

Mualem, Y. 1976. A new model for predicting the hydraulic conductivity of unsaturated porous media. Water Resour. Res. 12(3): 513–522.

Pertassek, T., A. Peters, and W. Durner. 2015. HYPROP-FIT Software User's Manual, V.3.0, UMS GmbH, Gmunder Str. 37, 81379 München, Germany, 66 pp.

Peters, A., and W. Durner. 2008. Simplified evaporation method for determining soil hydraulic properties. J. Hydrol. 356: 147–162.

Peters, A., S.C. Iden, and W. Durner. 2015. Revisiting the simplified evaporation method: Identification of hydraulic functions considering vapor, film and corner flow. J. Hydrol. 527: 531-542.

Poulovassilis, A. 1969. The effect of hysteresis of pore-water on the hydraulic conductivity. J. Soil Sci. 20: 52–56. doi:10.1111/j.1365-2389.1969.tb01553.x

Reynolds, W.D., D.E. Elrick, E.G. Youngs, A. Amoozegar, H.W.G. Booltink, and J. Bouma. 2002. Saturated and field-saturated water flow parameters. p. 797–801. *In* Dane, J.H., Topp, G. (eds.), Methods of Soil Analysis: Part 4 Physical Methods. Soil Science Society of America, Madison, WI.

Schelle, H., L. Heise, K. Jänicke, and W. Durner. 2013. Water retention characteristics of soils over the whole moisture range: A comparison of laboratory methods. Eur. J. Soil Sci. 64(6): 814–821.

Schindler, U., and L. Muller. 2006. Simplifying the evaporation method for quantifying soil hydraulic properties. J. Plant Nutr. soil Sci. (169): 623–629.

Tzimas, E. 1979. The measurement of soil-water hysteretic relationships on a soil monolith. Eur. J. Soil Sci. 30: 529–534. doi:10.1111/j.1365-2389.1979.tb01006.x

van Genuchten, M.Th. 1980. A closed-form equation for predicting the hydraulic conductivity of unsaturated soils1, Soil Sci. Soc. Am. J., 44(5): 892–898.

van Genuchten, M.Th., F.J. Leij, and L. Wu. 1997. Characterization and measurement of the hydraulic properties of unsaturated porous media (parts 1 and 2). University fo California, Riverside.

Wang, H, T.K. Tokunaga, J. Wan,W. Dong, and Y. Kim. 2016. Capillary pressure-saturation relations in quartz and carbonate sands: Limitations for correlating capillary and wettability influences on air, oil, and supercritical CO_2 trapping. Water Resour. Res. 52(8): 6671–6690.

Weller, U., O. Ippisch, M. Köhne, and H.-J. Vogel. 2011. Direct measurement of unsaturated conductivity including hydraulic nonequilibrium and hysteresis. Vadose Zone J. 10(2): 654–661.

Weller, U., and H.-J. Vogel. 2012. Conductivity and hydraulic nonequilibrium across drainage and infiltration fronts. Vadose Zone J. 11(3).

Wendroth, O., W. Ehlers, H. Kage, J.W. Hopmans, J. Halbertsma, and J.H.M. Wösten. 1993. Reevaluation of the evaporation method for Determining hydraulic functions in unsaturated Soils. Soil Sci. Soc. Am. J. 57(6): 1436–1443.

Wind, G.P. 1968. Capillary conductivity data estimated by a simple method for determining soil hydraulic properties in the method. p. 181–191. In P.E. Rijtema and H. Wassink

(eds.) Water in the Unsaturated Zone. Vol. 1. Proc. Wageningen Symp. June 1966. Int. Assoc. Scientific Hydrol., Gentbrugge, Belgium.

Zhuang, L., S.M. Hassanizadeh, C.J. van Duijn, I. Zizina, and R. Helmig. 2016a. Numerical study of saturation overshoot during water infiltration into dry soil. Water Resour. Res. Submitted.

Zhuang, L., S.M. Hassanizadeh, M.Th. van Genuchten, A. Leijnse, A. Raoof, and C. Qin. 2016b. Modeling of horizontal water redistribution in an unsaturated soil, Vadose Zone J., 15(3).

Chapter 4

Revisiting the Horizontal Redistribution of Water in Soils; Experiments and Numerical Modeling

Submitted to Water Resources Research, Zhuang, L., S.M. Hassanizadeh, P.J. Kleingeld, and M.Th. van Genuchten.

Abstract

A series of experiments and related numerical simulations were carried out to study one-dimensional water redistribution processes in an unsaturated soil. A Plexiglas sandbox was employed to pack sand as homogeneously as possible. The sandbox was divided into separate wet and dry parts using a very thin metallic plate. The wet section was initially fully saturated, while the initial saturation in the dry section was set to 0.2, 0.4 or 0.6 in three different experiments. Redistribution between the wet and dry sections started as soon as the metallic divider was removed. The saturation discontinuity was found to persist during the entire experiments, while the observed water pressure was found to become continuous immediately after the experiments started. Two models, the standard Richards equation and an interfacial area model, were used to simulate the experiments. Both models could simulate the observed saturation distributions reasonably well for the experiment with a lower initial water saturation in the dry section. However, the interfacial area model showed better agreement between observed and calculated water saturation and pressure distributions for the experiments having higher initial saturations in the dry section.

4.1 Introduction

Moisture redistribution is an important part of many near-surface and vadose zone hydrologic processes such as infiltration, root water uptake, evaporation, tile drainage and recharge, including contaminant transport. Numerous studies over the years have focused on the underlying physical phenomena of soil moisture redistribution and related capillary hysteresis processes, both experimentally (e.g., Haines, 1930; Youngs, 1958; Biswas et al., 1966; Staple, 1966, 1969; Gardner et al., 1970; Vachaud and Thony, 1971; Peck, 1971; Talsma, 1974; Diment and Watson, 1985; van Dam et al., 1996; Wang et al., 2003) as well as through numerical analyses (Rubin, 1967; Dane and Wierenga, 1975; Youngs and Poulovassilis, 1976; Diment and Watson, 1983; Philip. 1991; van Duijn et al., 1995; van Duijn and de Neef, 1998; Wang et al., 2004). Most of these studies concerned redistribution after infiltration in vertical soil profiles or laboratory soil columns, while several experimental studies also investigated horizontal moisture redistribution and hysteresis problems (Vachaud and Thony, 1971; Kona, 1997; Feuring et al., 2014).

Various theoretical approaches have been used to account for the effects of hysteresis during moisture redistribution. Relevant models can be divided into two different approaches: i) relatively conventional hysteresis models such as those used in the numerical studies cited above, some also accounting for the effects of dynamic non-equilibrium flow (e.g., Beliaev and Hassanizadeh, 2001; Beliaev and Schotting, 2001), and ii) an interfacial area model. We refer to the former approach as standard model. The latter approach introduces the specific fluid-fluid interfacial area, and corresponding governing equations, to account for hysteresis in the capillary pressure-saturation relationship (Niessner and Hassanizadeh, 2008; Pop et al., 2009; Zhuang et al., 2016). Very few studies up to now have investigated the comparative ability of the two modeling approaches to simulate water redistribution experiments (Zhuang et al., 2016).

In this chapter we provide results of a comprehensive experimental and numerical study of horizontal water redistribution in sand. We conducted a series of water redistribution experiments in a custom-built horizontal sandbox (or a flume) filled with a medium to coarse sand having different initial water saturations. The experimental results were simulated with both the standard model and the interfacial area model. In the following, we first describe the experimental setup and procedures. We then

introduce the two modeling approaches, followed by a comparison of the experimental data with numerical simulation results.

4.2 Description of experiments

4.2.1 Sand properties

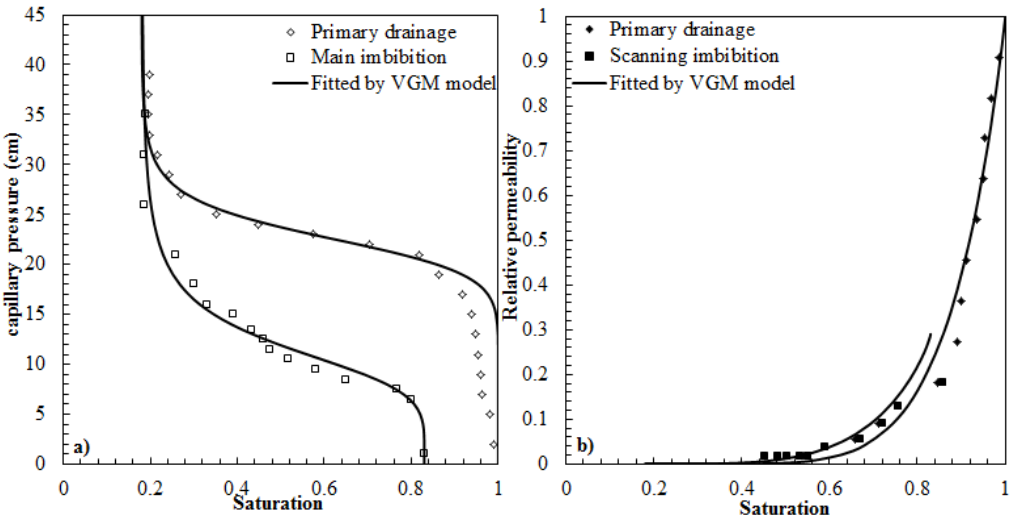

Figure 4.1 Measured and fitted a) retention curves for primary drainage and main imbibition; b) relative permeability curves for primary drainage and scanning imbibition

A medium to coarse sand (grain size 0.1-1 mm) taken from a riverbed in the Netherlands was used in the experiments. The sand had a mean particle diameter of 0.29mm. Prior to use, the sand was rinsed with deionized water to remove clay particles, and then air dried. Unsaturated hydraulic properties of the sand were measured using a small laboratory setup as described in detail in Chapter 3. The saturated conductivity was found to be 2.1×10^{-4} m/s, using the constant-head method (Reynolds et al., 2002). Capillary pressure-saturation curves for primary drainage and main imbibition were measured with the hanging water column method (Dane and Hopmans, 2002). Measured data are shown by symbols in Figure 4.1a. Simultaneously, unsaturated conductivities were measured directly for primary drainage and scanning imbibition using uniform gradient flow methods (e.g., Dirksen and Matula, 1994;

Weller et al., 2011); the data are shown in Figure 4.1b. Observed data were analyzed in terms of the standard van Genuchten-Mualem equations (Mualem, 1976; van

Table 4.1 Measured sand properties and fitted hydraulic parameter values

Parameters		**Unit**	**Value**
Particle density, ρ^S		kg m^{-3}	2.55×10^{3}
Water density, ρ^w		kg m^{-3}	1×10^{3}
Water viscosity, μ^w		Pa·s	1×10^{-3}
Saturated conductivity, K_S		m s^{-1}	2.1×10^{-4}
Intrinsic permeability, k		m^2	2.14×10^{-11}
Fitted hydraulic parameters in the van Genuchten-Mualem model			
Primary drainage	n	-	11 .4
	α	Pa^{-1}	4.4×10^{-4}
	l	-	4.3
Main imbibition	n	-	5.1
	α	Pa^{-1}	9.0×10^{-3}
	l	-	1.5
	ω	-	0.29

Genuchten, 1980) for water retention and the unsaturated hydraulic conductivity as follows:

$$p^c(S^w) = \frac{1}{\alpha}\left[S_e^{-1/m} - 1\right]^{1/n} \tag{4.1}$$

$$k^{rw}(S^w) = \omega(S_e)^l\left[1-\left(1-S_e^{1/m}\right)^m\right]^2 \tag{4.2}$$

$$S_e = \frac{S^w - S_{ir}^w}{1 - S_{ir}^w - S_r^a} \tag{4.3}$$

where S_{ir}^w, S_r^a , S^w and S_e are irreducible water saturation, residual air saturation, water saturation and effective water saturation, respectively, $p^c(S^w)$ and $k^{rw}(S^w)$ are capillary pressure and relative permeability, respectively, α, n and l are fitting parameters, and

m=1-1/n. The factor ω is introduced to account for the fact that the values of the unsaturated conductivity for main and scanning imbibition curves do not reach the saturated conductivity value. The value of ω was set equal to the ratio between the largest measured value of the unsaturated conductivity and the saturated conductivity (the latter at full saturation). The fitted curves are shown as solid lines in Figures 4.1a and 4.1b. Fitted parameter values and measured sand properties are listed in Table 4.1.

4.2.2 Experimental setup and procedure

We designed and constructed a long Plexiglas sandbox with dimensions of 2 cm (width) by 2 cm (height) by 60 cm (length) to conduct the horizontal water redistribution experiments. A schematic of the sandbox is shown in Figure 4.2. The sandbox was divided into two sections: one being 20 cm long and the other 40 cm. They were separated by a very thin metal plate (0.1 mm in thickness). This construction made it possible to pack the two sections with sand at different initial saturations. The long section ($0<x\leq40$) was filled with fully saturated sand, while the short section ($-20\leq x<0$) was filled with drier sand. The two sections were tightly closed at the top using a thin Plexiglas lid (1 mm in thickness); while silicone tapes were used to keep the whole sandbox air-tight and prevent any evaporation of water. The water redistribution experiments started by removing the thin plate. Mechanical springs were used at the two ends of the sandbox in order to push the two sections towards each other as the thin plate was being removed. This ensured full contact between the dry and wet sands at all times.

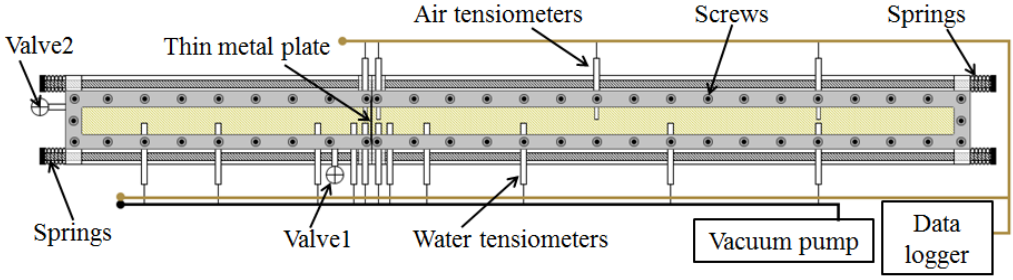

Figure 4.2 Schematic view of thin horizontal sandbox used for the experiments

Eleven water tensiometers and four air tensiometers (Rhizo Instruments, Wageningen, the Netherlands) were installed along the sandbox, as shown in Figure 4.2. They allowed the measurements of the water and air pressures every 1 min during the redistribution experiments. Locations of tensiometers are given in Table 4.2. The water

tensiometer composed of a ceramic cup, 1-cm long and 4 mm in diameter, and a small pore pressure transducer. An air permeable but water impermeable plastic hollow fiber was used to connect the ceramic cup to a vacuum in order to remove air from the tensiometer. The water tensiometers were saturated with deionized water prior to their use. The tubes between the ceramic cups and the transducers remained filled with water during the experiments. A Teflon porous cup was used for the air-selective tensiometer. A very thin tube, with a total volume of around 100 μL, was used to connect the hydrophobic porous cup with the pore transducer, while the joint between the thin tube and the transducer was sealed with a thicker silicone tube. The water and air pressure transducers were connected to a CR1000 data logger (Campbell Scientific, Shepshed, UK) to allow continuous recording of the pressure values. Readings from a few water tensiometers that malfunctioned during the experiments were not considered in the analysis.

A dual-energy gamma ray system was used to determine saturation and porosity values simultaneously at selected points along the sandbox. Coordinates of measured points are given in Table 4.2. Details of determination of saturation measurements using gamma radiation techniques are given in the Appendix C.

Table 4.2 Coordinates of tensiometer locations and gamma radiation measurement points

Devices	**Sides**	**Locations (*x* in cm)**
Water tensiometers	Dry	-0.5, -1.5,-3.5,-10,-15
	Wet	0.5, 1.5, 3.5, 10, 20, 30
Air tensiometers	Dry	-0.5
	Wet	0.5, 15, 30
Gamma radiation	Dry	-1, -2, -2.25, -2.5, -3, -4.5, -6.5, -8.5,-12.5,-18.5
	Wet	1, 2, 2.25, 2.5, 3, 4, 4.5, 6.5, 8.5, 10.5, 12.5, 14.5, 16.5, 18.5, 20.5, 22.5, 24.5, 26.5, 28.5, 30.5, 32.5, 34.5,36.5,38.5

The sandbox was fixed onto a rotatable frame between the gamma source emitter and the detector. The construction allowed us to rotate the sandbox by 90° after packing, so that gamma measurements could be made in the direction as shown in Figure 4.2. We used different procedures for filling the wet and dry sections of the sandbox. For the

wet section, clean air-dried sand was poured continuously and slowly into deionized and degassed water through a small funnel. The sand was regularly tapped and mixed using a small comb to prevent layering and promote the release of trapped gas. Sand for the dry section was first mixed with a certain amount of deionized and degassed water such that a large batch of sand with a pre-specified saturation was obtained. Then, as for the wet section, the sand was packed into the long section of the sandbox using the small comb.

Once both sections were filled, the two lids were fixed using screws and the whole sandbox was sealed. The sandbox with its mounted tensiometers was next brought into position in the gamma radiation system. Moist air was pumped slowly into the dry section through Valve 1, while Valve 2 was kept open. This was continued overnight in order to ensure moisture equilibrium in the sandbox and eliminate any potential for water evaporation during the experiments. A balloon filled with moist air was subsequently connected to Valve 2 (Figure 4.2), while Valve 1 was closed. The sandbox was then let to rest for several days, with the wet and dry sections still separated, in order to reach equilibrium. However, tensiometer and gamma radiation measurements were already collected during this period. The thin metallic plate was removed next to start the water redistribution process. As indicated earlier, the small gap between the dry and wet sections after removing the plate was eliminated by the action of springs. Moreover, silicon grease was applied around the joint to eliminate any leakage and/or water evaporation. The total weight of sand and water were recorded, before and after experiments, to verify that the overall water loss was negligible.

Table 4.3 Specifications of the experiments

Experiments	**Initial saturation of the dry section**	**Initial saturation of the wet section**
I	~0.2	1.0
II	~0.4	1.0
III	~0.6	1.0

We performed three sets of experiments, with three different initial saturation values for the dry section: 0.2, 0.4 and 0.6. Table 4.3 summarizes these initial conditions of the experiments. All experiments were conducted in a constant-temperature room at 21±0.5ºC.

4.3 1-D mathematical models

In this section, we describe the two alternative mathematical formulations that were used to simulate the horizontal redistribution process. For both models, we assumed that the air pressure was constant along the modeling domain. This assumption was supported by the air tensiometer measurements, which showed negligible spatial variations during the experiments.

4.3.1 Standard model

Simulations with the standard model were carried out using the HYDRUS-1D finite element software package (Šimůnek et al., 2009). The software uses the Richards equation for solving horizontal unsaturated flow in conjunction with hysteretic capillary pressure-saturation relationships as follows:

$$\varphi \frac{\partial S^w}{\partial t} + \frac{\partial}{\partial x}\left(-\frac{k^{rw}(S^w)k}{\mu^w}\left(\frac{\partial p^w}{\partial x} \right) \right) = 0 \tag{4.4}$$

$$-p^w = p^c(S^w) \tag{4.5}$$

where p^w denotes water pressure, p^c is the capillary pressure, t is time and x is the spatial coordinate. We note that dynamic capillarity effects are neglected when using Equation (4.5).

When using HYDRUS-1D, every numerical node in the discretized domain can be assigned its own cluster of scanning curves depending upon whether imbibition or drainage occurs. Two empirical approximations of capillary hysteresis, namely, Kool and Parker (1987) and Lenhard and Parker (1991), are included in HYDRUS-1D. In our study we used the Lenhard-Parker approach to describe the scanning curves. In this approach, all scanning curves are scaled from the main imbibition or drainage curves by adjusting the saturated water and residual water saturations, but using the same values of α and n as the main imbibition or primary drainage curves.

For the HYDRUS-1D simulations we used a grid size of 0.5 cm to obtain mesh-independent solutions. We assigned no-flow boundary conditions to both ends of the modeling domain, while water pressure and fluxes were assumed to be continuous at x=0, where wet and dry sand touch. The initial saturation of the wet section was S^w=1, while initial saturation of 0.2, 0.4 or 0.6 was assigned to the dry section.

4.3.2 Interfacial area model

The interfacial area model as used in this chapter is described in detail by Zhuang et al. (2016). Capillary hysteresis in the model is introduced by means of a new state variable, the air-water specific interfacial area (Hassanizadeh and Gray, 1990, 1993). The specific interfacial area, denoted by a^{wa}, is defined as the amount of air-water interfacial area per unit volume of the porous medium. The interfacial area model assumes that a^{wa} is a function of capillary pressure and saturation, which are now both considered to be independent variables. The set of hysteretic capillary pressure-saturation curves is replaced by a single p^c-S^w-a^{wa} surface. The projection of this surface onto the p^c-S^w plane would form all hysteretic capillary loops in the domain between the primary (or main) imbibition and drainage curves. A single p^c-S^w-a^{wa} surface under quasi-static conditions has been reported to exist by several researchers in numerical studies (Held and Celia, 2001; Joekar-Niasar et al., 2008; Joekar-Niasar and Hassanizadeh, 2011, 2012) and experimental investigations (e.g., Chen and Kibbey, 2006; Karadimitriou et al., 2013, 2014).

Table 4.4 Values of the coefficients in Equation (4.6)

Parameter	Value	Standard error
γ_1 [1/(Pa·m)]	20.7	1.40
γ_2	2.0	0.15
γ_3	1.0	0.10
R^2	0.96	

Similar to traditional p^c-S^w curves, the p^c-S^w-a^{wa} surface is a hydraulic property of a given soil. In principle, the surface should be measured experimentally. However, since measurements of the specific interfacial area were not available, we constructed the surface in this study with the aid of p^c-S^w data points. Our approach is based on a method proposed by Bradford and Leij (1997), and described in detail in Chapter 5. Despite its uncertainties and limitations (see e.g., Grant and Gerhard, 2007), we found this indirect method to be sufficient for our modeling purposes, as a first-order approximation. For our purpose it suffices that the projection of the p^c-S^w-a^{wa} surface should reproduce p^c-S^w curves in the p^c-S^w plane. The calculated p^c-S^w-a^{wa} points were fitted by the following power function, proposed by Joekar-Niasar and Hassanizadeh (2012):

$$a^{wa}\left(S^w, p^c\right) = \gamma_1 S^w \left(1 - S^w\right)^{\gamma_2} \left(p^c\right)^{\gamma_3} \tag{4.6}$$

where γ_1, γ_2 and γ_3 are fitting parameters. The fitted p^c-S^w-a^{wa} surface and its parameters are given in Figure 4.3 and Table 4.4, respectively. The black symbols in Figure 4.3 represent p^c-S^w-a^{wa} points obtained using the method of Bradford and Leij (1997).

The interfacial area model introduces an evolution equation for the air-water specific interfacial area as follows (Hassanizadeh, 2015)

$$\frac{\partial a^{wa}}{\partial t}+\frac{\partial\left(a^{wa}w^{wa}\right)}{\partial x}=E^{wa} \tag{4.7}$$

where w^{wa} is the macroscopic flux of the specific interfacial area. E^{wa} is the net production rate of the specific interfacial area, Following Chapter 5, the latter is approximated by

$$E^{wa}=-L\frac{\partial a^{wa}}{\partial p^c}\frac{\partial S^w}{\partial t} \tag{4.8}$$

in which L is a material coefficient.

Limited literature studies have shown that the flux w^{wa} is very small (Joekar-Niasar and Hassanizadeh, 2011; Karadimitriou et al., 2014). Neglecting the corresponding term in Equation (4.7) and using Equation (4.8) lead then to

$$\frac{\partial a^{wa}}{\partial t}=-L\frac{\partial a^{wa}}{\partial p^c}\frac{\partial S^w}{\partial t} \tag{4.9}$$

The term E^{wa} accounts for the creation and destruction of interfaces during water redistribution. The material coefficient L is assumed to be different during drainage and imbibition, and given by (Chapter 5):

$$L=\frac{L_{im}+L_{dr}}{2}+\frac{L_{im}-L_{dr}}{2}sign(\frac{\partial S^w}{\partial t}) \tag{4.10}$$

where L_{im} and L_{dr} denote the values of L for imbibition and drainage, respectively. They would be optimized later using experimental data.

The interfacial area model also uses the Richards equation to describe water flow. Hence, the set of equations to be solved hence are Equations (4.4), (4.6) and (4.9). As before, the relative permeability is still assumed to be given by Equation (4.2). Our measurements have shown that hysteresis in relative permeability is negligible (see

Figure 4.1b), which allows Equation (4.2) to be written as a unique function of saturation.

The full set of equations for the interfacial area model was solved in terms of two primary variables: S^w and p^c. We used for this purpose the commercial package COMSOL Multiphysics 5.0 (COMSOL, 2014). We used a numerical grid size of 0.1 cm, while residual errors were restricted to 10^{-8} in order to achieve mesh-independent solutions. As initial conditions for the various experiments we used measured values of saturation and capillary pressure. The solutions assumed continuity in the capillary pressure and water flux at x=0. No-flow boundary conditions were assigned to the two ends of the domain.

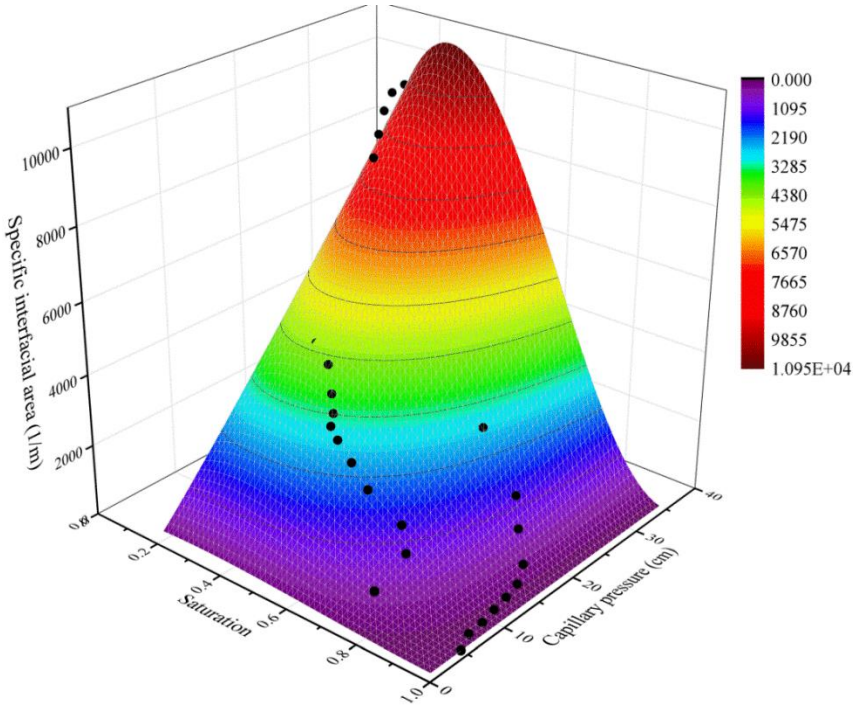

Figure 4.3 Three-dimensional p^c-S^w-a^{wa} surface; the black symbols represent p^c-S^w-a^{wa} points using the method of Bradford and Leij (1997).

4.4 Results and discussion

4.4.1 Experiments

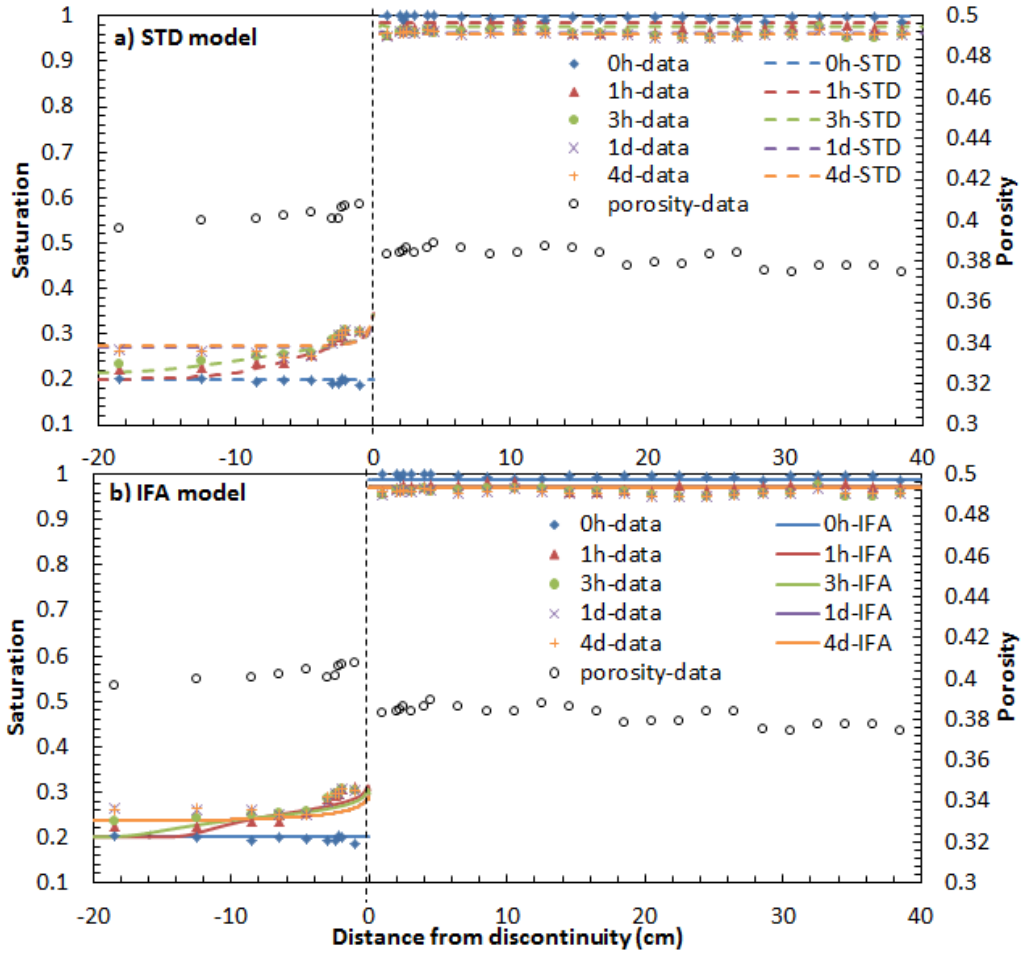

Figure 4.4 Measured porosity (open circles) and observed saturation profiles (other symbols) versus distance from the discontinuity for Experiment I, which had an initial saturation of 0.2 in the dry section. Also shown are simulated curves obtained with (a) the standard (STD) model (dashed lines) and (b) the interfacial area (IFA) model (solid lines).

Measured porosity and saturation profiles for experiments I, II and III are shown in Figures 4.4, 4.6, and 4.8, respectively. In each figure, measured porosities along the entire sandbox are shown by circles, while other symbols with different colors represent measured saturation profiles at different times. As can be seen in all figures, the sand packing along the entire sandbox was reasonably uniform, with minor fluctuations in porosities and initial water saturations. The small differences in

porosities between the dry and wet sections are probably caused by the different packing procedures we used for the two sections, as explained earlier.

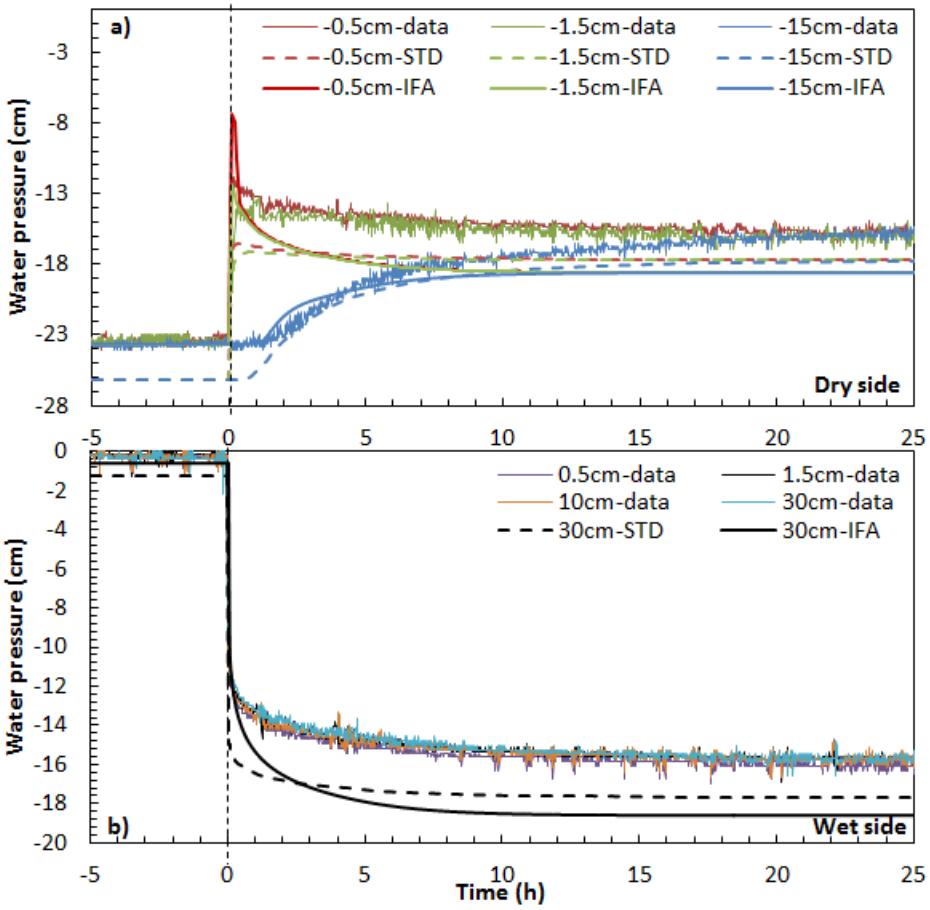

Figure 4.5 Measured water pressure vs. time (thin lines) at several locations within (a) the dry and (b) the wet sections for Experiment I, which had an initial saturation of 0.2 in the dry section. Simulated curves obtained with the standard (STD) and interfacial area (IFA) models are shown as dashed and solid lines, respectively.

For Experiment I (Figure 4.4), saturation values in the dry section (x<0) increased markedly near the discontinuity within one hour after redistribution started, but then remained almost constant afterwards. By comparison, saturation values in the wet section (x>0) decreased over the entire wetted length almost evenly. This is due to the much higher unsaturated conductivities in the wet section, which requires only very small water pressure gradients for any flow to occur. The entire redistribution process

reached the equilibrium state after about one day. The saturation discontinuity at the discontinuity (x=0) persisted at all times.

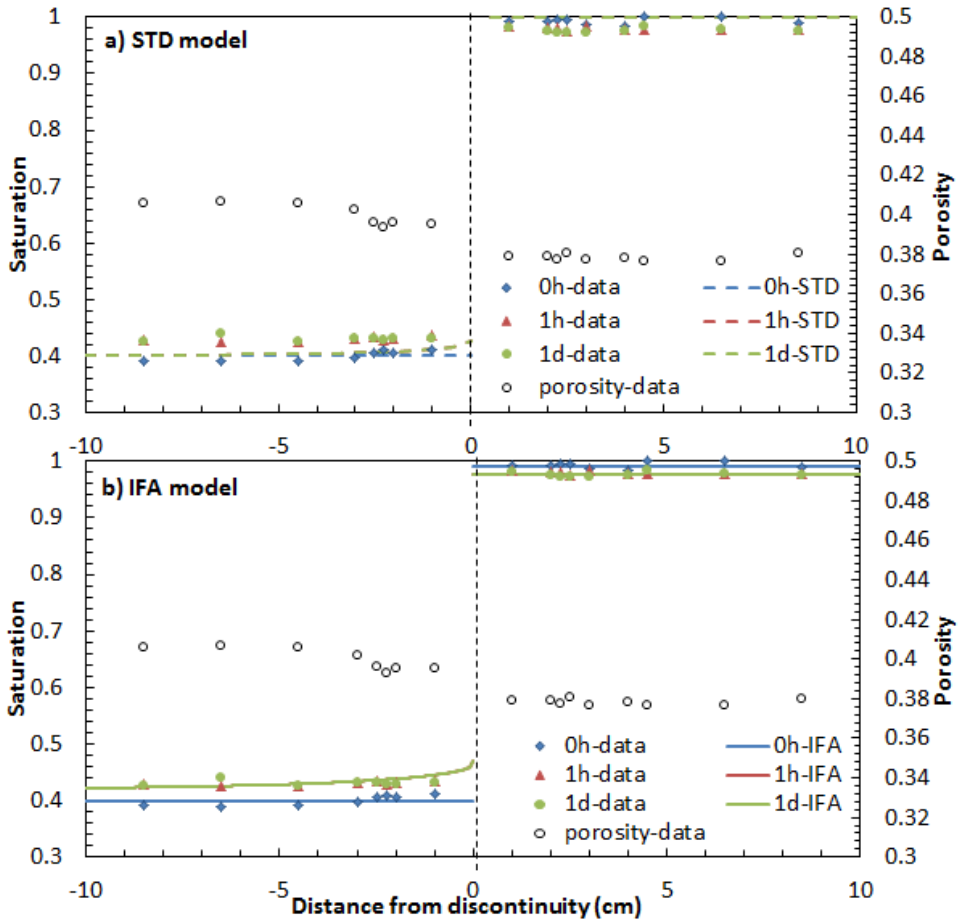

Figure 4.6 Measured porosity (open circles) and observed saturation profiles (other symbols) versus distance from the discontinuity for Experiment II, which had an initial saturation of 0.4 in the dry section. Also shown are simulated curves obtained with (a) the standard (STD) model (dashed lines) and (b) the interfacial area (IFA) model (solid lines).

Measured water pressure heads as a function of time at several locations within the dry and wet sections of Experiment I are shown in Figures 4.5a and 4.5b, respectively. Thin colored lines with small fluctuations represent the water pressure measurements. As can be seen in Figure 4.5a, at points closest to the discontinuity in the dry section (x=-0.5 cm), the pressure increased at the start of the experiment, but then went down

gradually to reach equilibrium. By comparison, the water pressure at the location farthest away from the discontinuity (x=-15 cm) increased only gradually during the redistribution process. However, water pressures in the wet section (Figure 4.5b) decreased far more uniformly along the entire domain. Pressure heads measured at -0.5 cm and 0.5 cm became the same nearly immediately and then followed similar patterns afterwards. This implies that water pressures across the discontinuity were continuous during the entire redistribution process.

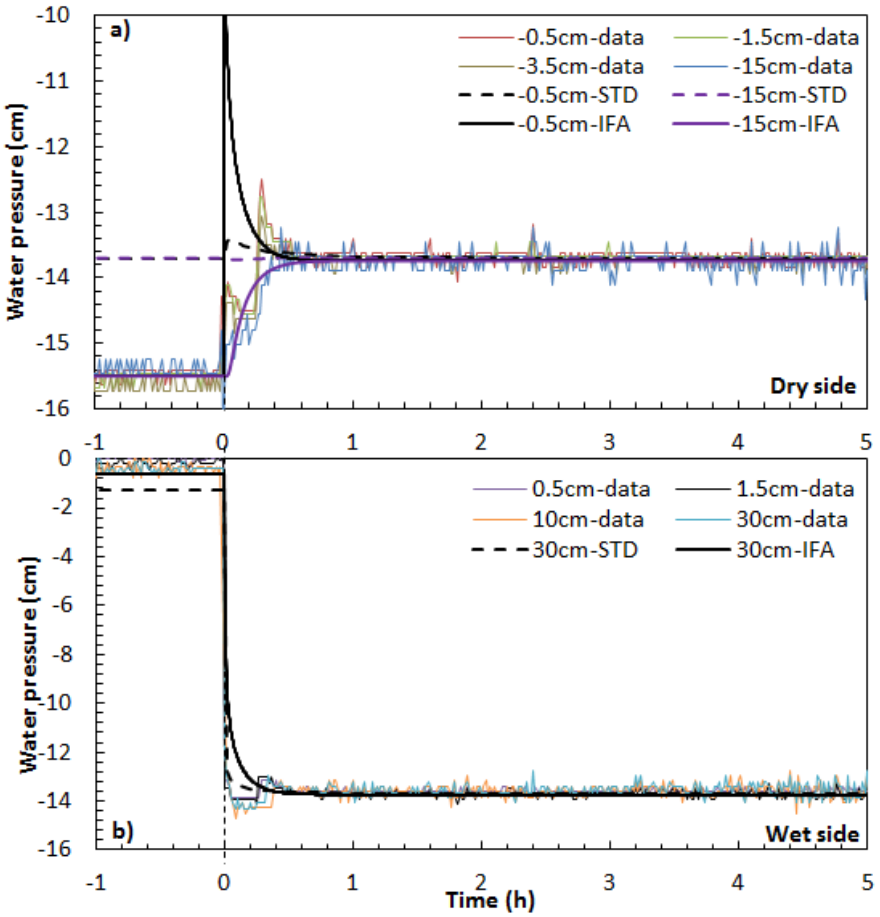

Figure 4.7 Measured water pressure vs. time (thin lines) at several locations within (a) the dry and (b) the wet sections for Experiment II, which had an initial saturation of 0.4 in the dry section. Simulated curves obtained with the standard (STD) and interfacial area (IFA) models are shown as dashed and solid lines, respectively.

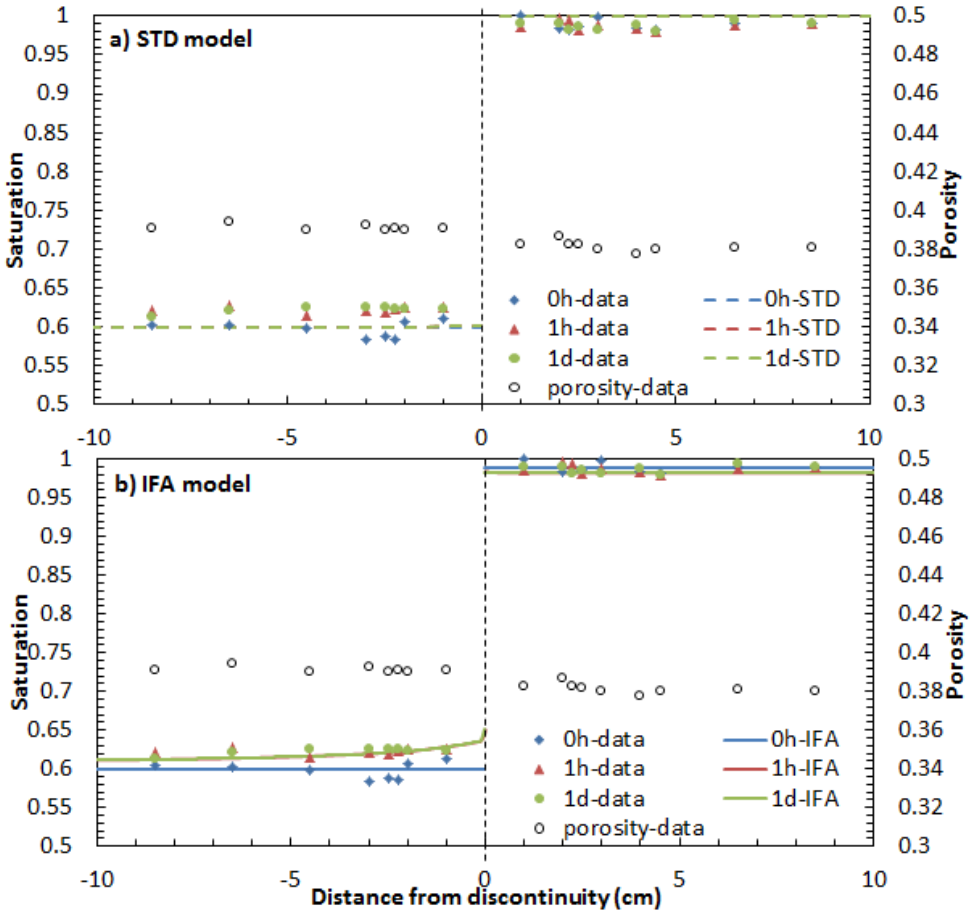

Figure 4.8 Measured porosity (open circles) and observed saturation profiles (other symbols) versus distance from the discontinuity for Experiment III, which had an initial saturation of 0.6 in the dry section. Also shown are simulated curves obtained with (a) the standard (STD) model (dashed lines) and (b) the interfacial area (IFA) model (solid lines).

For Experiments II and III, which had initial saturations of 0.4 and 0.6, respectively, measured saturation values changed monotonically in both the dry (x<0) and wet sections (x>0), as seen in Figures 4.6 and 4.8. For this reason we show here only measured data close to the discontinuity (-10<x<10). For both experiments, the magnitude of the saturation discontinuity decreased, but persisted during the entire process. Measured water pressure heads at different locations for the two experiments (II and III) are shown in Figures 4.7 and 4.9. Pressure heads at the locations near the discontinuity in the dry section exhibited again short-lived peaks for both experiments,

but now with significantly fluctuations (lower peaks) as compared to Experiment I with its lowest initial saturation of 0.2 in the dry section. Experiment III (having an initial saturation of 0.6) showed the smallest peak in the dry section after redistribution started.

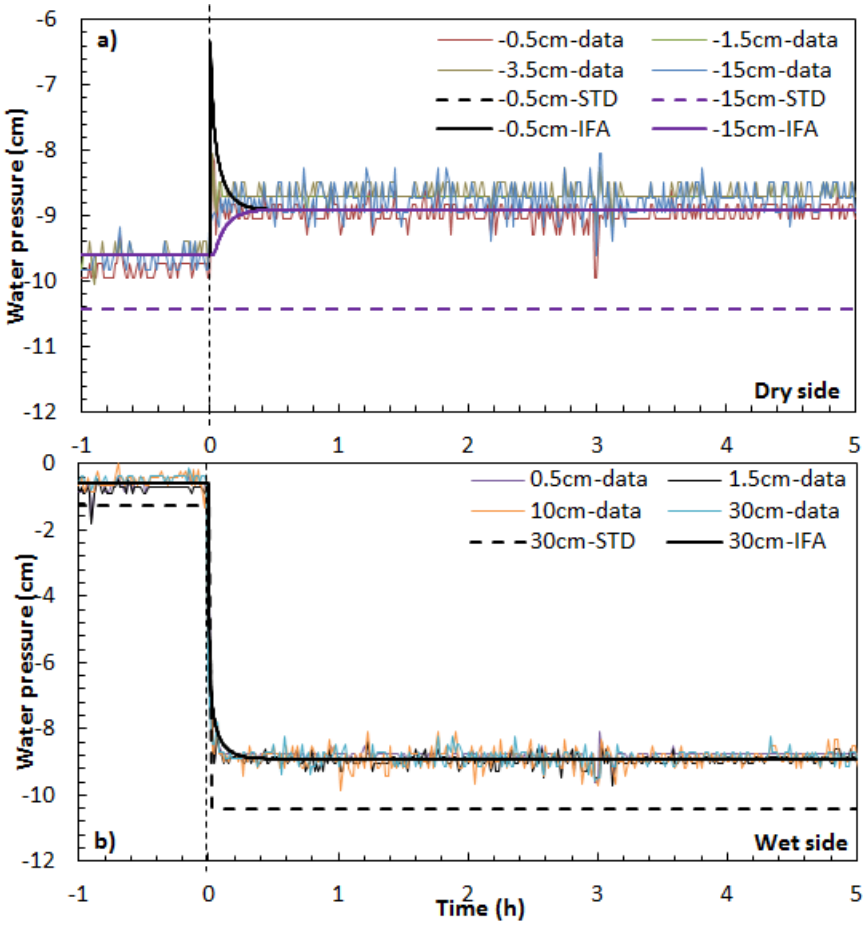

Figure 4.9 Measured water pressure vs. time (thin lines) at several locations within (a) the dry and (b) the wet sections for Experiment III, which had an initial saturation of 0.6 in the dry section. Simulated curves obtained with the standard (STD) and interfacial area (IFA) models are shown as dashed and solid lines, respectively.

4.4.2 Simulations

The three experiments were simulated using both the standard (STD) model (as programmed in HYDRUS-1D) and the interfacial area (IFA) model presented earlier.

For the simulations using the standard model, we assumed that initially the sand was in an imbibition state everywhere, consistent with the way the sandbox had been packed. Initial conditions in the HYDRUS simulations were specified in terms of saturation values (not water pressure heads). For the interfacial area model simulations, we used the measured water saturations and pressure distributions as initial conditions. A single p^c-S^w-a^{wa} surface was used for both sections. The values of L_{im} and L_{dr} in Equation (4.10) were optimized based on measured saturation and pressure data; producing the values shown in Table 4.5. Simulation results obtained with the standard (STD) model are shown as dashed lines in Figures 4.4 through 4.9, while solid lines represent results obtained with the interfacial area (IFA) model. Since water pressure heads at different locations in the wet section differed only slightly, simulated curves of the pressures versus time are shown for only one position.

Table 4.5 Fitted values of L_{im} and L_{dr} in the interfacial area model

Dry section		**Wet section**
L_{im} (Pa)	L_{dr}(Pa)	L_{dr}(Pa)
9,000	15,000	180,000

As can be seen in Figure 4.4 for Experiment I, simulation results obtained with the standard and the interfacial area models both reproduced the measured saturation distributions reasonably well. Because of a lack of experimental data of the relative permeability at the lower saturation (see Figure 4.1), the value of l in Equation (4.2) was optimized. We found a value of -0.8 using the measured data for both simulations with the initial saturation at 0.2. Figure 4.5 shows that simulated water pressures obtained with both models still deviated slightly from the measurements.

Simulations of Experiments II and III (Figures 4.6-4.9) show that the standard model predicts only minimal redistribution of water, whereas the interfacial area model captured the measured saturation and water pressure data much better.

We note that either initial saturation or the water pressure distributions can be specified as initial condition in the standard model. This led to an inconsistency in the initial saturations and water pressures (see Figures 4.5, 4.7 and 4.9). This discrepancy can be eliminated by adjusting the imbibition p^c-S^w curve (which was measured independently and is shown in Figure 4.1), based on measured initial water saturation and pressure for each experiment. However, shifting the imbibition p^c-S^w curve for each set of experiment seems to be unreasonable and nonphysical. By comparison,

both initial saturation and water pressure can be specified in the interfacial area model, thus allowing consistent initial conditions.

As shown in Table 4.5, two different values of L_{dr} were used for the dry and wet sections in the interfacial area model simulations. This indicates that the coefficient L in the production term for drainage process is still hysteretic. Moreover, micromodel studies (e.g., Karadimitriou et al., 2014) have shown that L is a material property and may depend on saturation. We emphasize that additional analyses and experiments are still needed to investigate the uncertain parameters in the interfacial area model.

4.5 Conclusions

In this study we performed a series of well-defined water redistribution experiments in an unsaturated soil. A custom-built thin Plexiglas sandbox was employed to conduct three sets of experiments with different initial water saturations in the dry section (0.2, 0.4 and 0.6). Gamma transmission method was used to measure water saturations at different locations along the sandbox, while water and air tensiometers were installed at various positions to collect pressure data. The magnitude of discontinuity in water saturation decreased but it persisted in all experiments. Water pressures near the discontinuity were found to become continuous immediately after the experiments started. We observed that the degree of water redistribution decreased when the initial water saturation in the dry section increased; i.e. smaller difference in saturation between the wet and dry sections produced less redistribution of water.

Two different models, the standard Richards equation and the interfacial area models, were employed to simulate the three sets of experiments. The standard model could simulate the water saturation distributions for the experiment with the lowest initial water saturation (around 0.2). However, contrary to observations, The Richards equation predicted almost no water redistribution for the other two experiments. The interfacial area model, however, could reproduce water saturation distributions observed in all three experiments, albeit by fitting the value of the coefficient of the area production term. We must point out that the interfacial area model still contains some adjustable parameters; hence, it has more flexibility in fitting the experimental data.

4.6 Appendix C: Simultaneous measurement of saturation and porosity

Gamma radiation attenuation in an unsaturated soil sample can be described using Beer-Lambert's equation. Our gamma system consisted of ^{241}Am, with an energy peak of 59 keV, and ^{137}Cs, with an energy peak of 662 keV. Thus, two equations can be written for the measured attenuated intensities:

$$I^{Am} = I_0^{Am} \exp(-\mu_s l_s - \mu_w l_w) \quad \text{and} \quad I^{Cs} = I_0^{Cs} \exp(-\mu_s l_s - \mu_w l_w) \qquad \text{(C1)}$$

where I and I_0, with indexes for the two sources, denote measured and corresponding reference intensities, respectively, μ_s and μ_w are the solid and water attenuation coefficients, and l_s and l_w denote the overall length of the solid and water phases along the path of the gamma-ray beam, respectively.

The diameter of the gamma-ray beam was 6 mm. Measured intensities hence were average values over the cross section of the beam and the soil thickness. The attenuation coefficients μ_s and μ_w for both ^{241}Am and ^{137}Cs were measured and calculated beforehand. Details of the calibration procedure information about the dual gamma ray system can be found in Fritz (2012). Values of the reference intensity I_0 for both ^{241}Am and ^{137}Cs was set equal to the measured intensities of the empty sandbox. At any given time and position, values of l_s and l_w could be calculated from the measured intensities for ^{241}Am and ^{137}Cs using Equation (C1). The sand porosity (φ) and water saturation (S^w) can then be calculated at any given time and position from the following equations:

$$\varphi = \frac{l - l_s}{l} \quad \text{and} \quad S^w = \frac{l_w}{l - l_s} \qquad \text{(C2)}$$

respectively, in which l is the total thickness of the soil sample (i.e. 2 cm, being the width of our sandbox).

Acknowledgements

We gratefully acknowledge Harm Gooren from Wageningen University, and Thom Claessen, Sander Deelen, and Arjen de Waal from Utrecht University for their technical support. The first author was supported by the China Scholarship Council (No. 201206380076). The second author received funding from the European Research Council under the European Union's Seventh Framework Program (FP/2007-2013)/ERC Grant Agreement No. 341225.

References

Beliaev, A.Y., and S.M. Hassanizadeh. 2001. A theoretical model of hysteresis and dynamic effects in the capillary relation for two-phase flow in porous media. Transp. Porous Media 43(1): 487–510.

Beliaev, A.Y., and R.J. Schotting. 2001. Analysis of a new model for unsaturated flow in porous media including hysteresis and dynamic effects. Comput. Geosci. 5(2): 345–368.

Biswas, T.D., D.R. Nielsen, and J.W. Biggar. 1966. Redistribution of soil water after infiltration. Water Resour. Res. 2(3): 513–524.

Bradford, S.A., and F.J. Leij. 1997. Estimating interfacial areas for multi-fluid soil systems. J. Contam. Hydrol. 27(1–2): 83–105.

Chen, L. and T.C.G. Kibbey. 2006. Measurement of air-water interfacial area for multiple hysteretic drainage curves in an unsaturated fine sand. Langmuir 22(16): 6874–6880.

COMSOL. 2014. COMSOL Multiphysics 5.0. COMSOL Inc., Burlington, MA.

Dane, J.H., and J.W. Hopmans. 2002. Water retention and storage: laboratory. p. 675–720. *In* Dane, J.H., Topp, G. (eds.), Methods of Soil Analysis: Part 4 Physical Methods. Soil Science Society of America, Madison, WI.

Dane, J.H., and P.J. Wierenga. 1975. Effect of hysteresis on the prediction of infiltration, redistribution and drainage of water in a layered soil. J. Hydrol. 25(514): 229–242.

Diment, G., and K. Watson. 1983. Stability analysis of water movement in unsaturated porous materials 2. numerical studies. Water Resour. Res. 19(4): 1002–1010.

Diment, G., and K. Watson. 1985. Stability analysis of water movement in unsaturated porous materials: 3. Experimental studies. Water Resour. Res. 21(7): 979–984.

Dirksen, C., and S. Matula. 1994. Automatic Atomized Water Spray System for Soil Hydraulic Conductivity Measurements. Soil Sci. Soc. Am. J. 58: 319–325.

van Duijn, C.J., J. Molenaar, and M.J. de Neef. 1995. The effect of capillary forces on immiscible two-Phase flow in heterogeneous porous media. Transp. Porous Media 21(1): 71–93.

van Duijn, C.J., and M.J. de Neef. 1998. Similarity solution for capillary redistribution of two phases in a porous medium with a single discontinuity. Adv. Water Resour. 21(6): 451–461.

Feuring, T., J. Braun, B. Linders, G. Bisch, S.M. Hassanizadeh, and J. Niessner. 2014. Horizontal redistribution of two fluid phases in a porous medium: experimental investigations. Transp. Porous Media: 1–13.

Fritz, S. 2012. Experimental investigations of water infiltration into unsaturated Soil - analysis of dynamic capillarity effects.

Gardner, W.R., D. Hillel, and Y. Benyamini. 1970. Post-irrigation movement soil water 1. redistribution. Water Resour. Res. 6(3): 851–861.

Grant, G.P., and J.I. Gerhard. 2007. Simulating the dissolution of a complex dense nonaqueous phase liquid source zone: 1. Model to predict interfacial area. Water Resour. Res. 43(12): 1–14.

Haines, W.B. 1930. Studies in the physical properties of soil. V. The hysteresis effect in capillary properties, and the modes of moisture distribution associated therewith. J. Agric. Sci. 20(1): 97–116.

Hassanizadeh, S.M. 2015. Advanced theories of two-phase flow in porous media. p. 47–62. *In* Handbook of Porous Media, Third Edition. CRC Press.

Hassanizadeh, S.M., and W.G. Gray. 1990. Mechanics and thermodynamics of multiphase flow in porous media including interphase boundaries. Adv. Water Resour. 13(4): 169–186.

Hassanizadeh, S.M., and W.G. Gray. 1993. Thermodynamic basis of capillary-pressure in porous-media. Water Resour. Res. 29(10): 3389–3405.

Held, R.J., and M.A. Celia. 2001. Modelling support of functional relationships between capillary pressure, saturation, interfacial area and common lines. Adv. Water Resour. 24: 325–343.

Joekar-Niasar, V., and S.M. Hassanizadeh. 2011. Specific interfacial area: The missing state variable in two-phase flow equations? Water Resour. Res. 47: W05513.

Joekar-Niasar, V., and S.M. Hassanizadeh. 2012. Uniqueness of specific interfacial area-capillary pressure-saturation relationship under non-equilibrium conditions in two-phase porous media flow. Transp. Porous Media 94: 465–486.

Joekar-Niasar, V., S.M. Hassanizadeh, and A. Leijnse. 2008. Insights into the Relationships among capillary pressure, saturation, interfacial area and relative permeability using pore-network modeling. Transp. Porous Media 74: 201–219.

Karadimitriou, N.K., S.M. Hassanizadeh, V. Joekar-Niasar, and P.J. Kleingeld. 2014. Micromodel study of two-phase flow under transient conditions: Quantifying effects of specific interfacial area. Water Resour. Res. 50(10): 8125–8140.

Karadimitriou, N.K., M. Musterd, P.J. Kleingeld, M.T. Kreutzer, S.M. Hassanizadeh, and V. Joekar-Niasar. 2013. On the fabrication of PDMS micro-models by rapid prototyping, and their use in two-phase flow studies. Water Resour. Res. 49 (4), 2056-2067.

Kona, S. 1997. Experimental Investigation of Horizontal Redistribution of Water in Unsaturated Porous Media.

Kool, J.B., and J.C. Parker. 1987. Development and evaluation of closed-form expressions for hysteretic soil hydraulic properties. 23(1): 105–114.

Lenhard, R.J., and J.C. Parker. 1991. Comparing simulated and experimental hysteretic two-phase transient fluid flow phenomena. Water Resour. Res. 27(8): 2113–2124.

Mualem, Y. 1976. A new model for predicting the hydraulic conductivity of unsaturated porous media. Water Resour. Res. 12(3): 513–522.

Niessner, J., and S.M. Hassanizadeh. 2008. A model for two-phase flow in porous media including fluid-fluid interfacial area. Water Resour. Res. 44(8): W08439.

Peck, A.J. 1971. Redistribution of soil water after infiltration. Soil Res. 9(2): 59–71.

Philip, J.R. 1991. Horizontal redistribution with capillary hysteresis. Water Resour. Res. 27(7): 1459–1469.

Pop, I.S., C.J. van Duijn, J. Niessner, and S.M. Hassanizadeh. 2009. Horizontal redistribution of fluids in a porous medium: The role of interfacial area in modeling hysteresis. Adv. Water Resour. 32(3): 383–390.

Reynolds, W.D., D.E. Elrick, E.G. Youngs, A. Amoozegar, H.W.G. Booltink, and J. Bouma. 2002. Saturated and field-saturated water flow parameters. p. 797–801. *In* Dane, J.H., Topp, G. (eds.), Methods of Soil Analysis: Part 4 Physical Methods. Soil Science Society of America.

Rubin, J. 1967. Numerical method for analyzing hysteresis-affected post-infiltration redistribution of soil moisture. Soil Sci. Soc. Am. Proc. 31(1): 13–20.

Šimůnek, J., M. Šejna, H. Saito, M. Sakai, and M.Th. van Genuchten. 2008. The Hydrus-1D software package for simulating the movement of water, heat, and multiple solutes in variably saturated media. Version 4.0. HYDRUS Software Series 3. Department of Environmental Sciences, University of California Riverside, Riverside, CA, 315 p. (http://www.pc-progress.com/en/Default.aspx?hydrus-1d)

Staple, W.J. 1966. Infiltration and redistribution of water in vertical columns of loam soil. Soil Sci. Soc. Am. J. 30: 553.

Staple, W.J. 1969. Comparison of computed and measured moisture redistribution following infiltration. Soil Sci. Soc. Am. J. 33(6): 840–847.

Talsma, T. 1974. The effect of initial moisture content and infiltration quantity on redistribution of soil water. Soil Res. 12(1): 15–26.

Vachaud, G., and J. Thony. 1971. Hysteresis during infiltration and redistribution in a soil column at different initial water contents. Water Resour. Res. 7(1): 111–127.

van Dam, J.C., J.H.M. Wösten, and a. Nemes. 1996. Unsaturated soil water movement in hysteretic and water repellent field soils. J. Hydrol. 184(3–4): 153–173.

van Genuchten, M.T. 1980. A closed-form equation for predicting the hydraulic conductivity of unsaturated soils1. Soil Sci. Soc. Am. J. 44(5): 892–898.

Wang, Z., W.A. Jury, A. Tuli, and D.-J. Kim. 2004. Unstable flow during redistribution. Vadose Zone J. 3(2): 549–559.

Wang, Z., A. Tuli, and W.A. Jury. 2003. Unstable Flow during Redistribution in Homogeneous Soil. Vadose Zone J. 2(1): 52–60.

Weller, U., O. Ippisch, M. Köhne, and H.-J. Vogel. 2011. Direct measurement of unsaturated conductivity including hydraulic nonequilibrium and hysteresis. Vadose Zone J. 10(2): 654–661.

Youngs, E.G. 1958. Redistribution of moisture in porous materials after infiltration: 2. Soil Sci. 86(4): 202–207.

Youngs, E.G., and A. Poulovassilis. 1976. The different forms of moisture profile development during the redistribution of soil water after infiltration. Water Resour. Res. 12(5): 1007–1012.

Zhuang, L., S.M. Hassanizadeh, M.T. van Genuchten, A. Leijnse, A. Raoof, and C. Qin. 2016. Modeling of horizontal water redistribution in an unsaturated soil. Vadose Zone J. 15(3).

Chapter 5

Numerical Study of Saturation Overshoot during Water Infiltration into Dry Soil

Prepared for submission to Water Resources Research, Zhuang, L., S.M. Hassanizadeh, C.J. van Duijn, S. Zimmermann, I. Zizina, and R. Helmig.

Abstract

Two mathematical models, a conventional hysteretic unsaturated flow model and an interfacial area model, were employed to simulate non-monotonic saturation behavior during water infiltration into dry soil. Both models are based on the Richards equation and include dynamic capillarity effects. The conventional hysteretic model accounts for hysteresis in both the relative permeability and capillary pressure relationships. In the interfacial area model, the specific interfacial area was introduced to simulate hysteresis in capillary pressure-saturation relationship. This was done by including a constitutive equation for the specific interfacial area, as a function of saturation and capillary pressure, as well as an equation for its evolution. The two models were used to simulate a set of one-dimensional water infiltration experiments. In those experiments, saturation breakthrough curves were measured at a point below the inlet. Saturation changes with time showed a clear non-monotonic behavior, i.e., an overshoot. Parameter values were determined in order to obtain the best fitting of experimental data, and, in particular, to model the saturation overshoot. The interfacial area model provided much better agreement with the data.

5.1 Introduction

It is known that when water infiltrates into soil, under some certain initial and boundary condition, it forms wetting fingers instead of moving as a smooth front (see Figure 5.1). The unstable fingering front was first observed by Hill and Parlange (1972) in a layered soil. Later studies by Diment and Watson (1985) showed that unstable fronts also appeared in non-layered dry soils. During the last few decades, many 1D, 2D or 3D experiments have been carried out to investigate the factors that cause the appearance of fingers and affect their width and speed (Glass et al., 1989a, 1990; Baker and Hillel, 1990; Selker et al., 1992; Liu et al., 1994a; Lu et al., 1994b). Experimental measurements showed that a characteristic saturation overshoot occurred at the tip of each finger (Glass et al., 1989a; Liu et al., 1994a; Lu et al., 1994a), as well as non-monotonic water pressure profiles (Baker and Hillel, 1990; Selker et al., 1992; Lehmann et al., 1998; Bauters et al., 2000). Recently, comprehensive 1D experiments were conducted to show the occurrence of overshoot in saturation (DiCarlo, 2004; Fritz, 2012) and/or pressure (Stonestrom and Akstin, 1994; Geiger and Durnford, 2000; DiCarlo, 2007; Fritz, 2012) under different conditions.

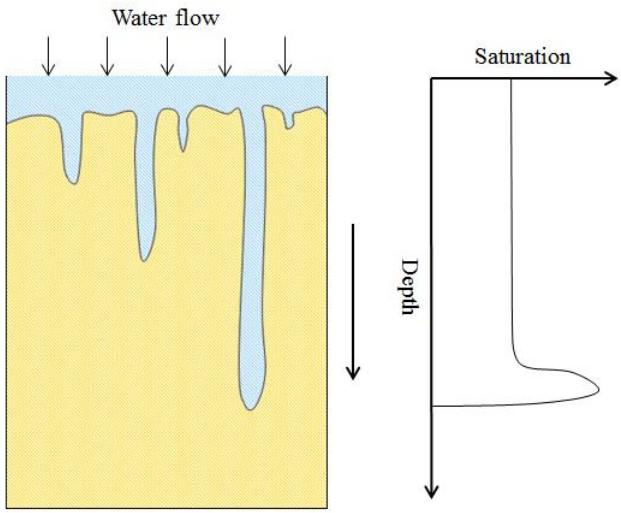

Figure 5.1 Schematic of fingering flow (left) and the water distribution in a finger (right)

Initial attempts to simulate fingering flow were all based on models using the Richards equation (Glass et al., 1989b; Liu et al., 1994b; Nieber, 1996; Eliassi and Glass, 2001). However, these models were not able to reproduce fingering phenomena since the

Richards equation is unconditionally stable, even if hysteresis in the hydraulic properties is included (Otto, 1997; Eliassi and Glass, 2001; Egorov et al., 2002). Many improvements or modifications have been proposed to extend Darcy scale formulations (Wang et al., 1998; Egorov et al., 2002; Eliassi and Glass, 2002; Nieber et al., 2003; Cueto-Felgueroso and Juanes, 2008). Among these is the concept of dynamic capillarity proposed by Hassanizadeh and Gray (1993b). They showed that the difference in fluid pressures is not only a function of saturation, but also depends on the time rate of change of saturation. Dynamic capillarity effects have been observed experimentally as early as in 1978 by Stauffer (1978). For a review of experimental works on dynamic effects, see Hassanizadeh et al. (2002). The dynamic capillarity term has been included in mathematical models of unsaturated flow, based on traditional Darcy's law as shown to be conditionally unstable and may result in non-monotonic saturation profiles (see e.g., Egorov et al., 2002; Cuesta and Hulshof, 2003; van Duijn et al., 2004). Numerical solutions of these models have been compared with experimental data by DiCarlo (2005). Also, numerical models including capillary hysteresis, were developed by Nieber et al. (2003), and were compared to experiments later on by Sander et al. (2008) and Chapwanya and Stockie (2010).

In addition to conventional hysteretic models combined with dynamic capillarity effects, an alternative model has been proposed by Hassanizadeh and Gray (1990) based on introducing the specific interfacial area. In that model, the full set of hysteretic capillary pressure-saturation curves (including all scanning curves) is replaced by a single interfacial area-capillary pressure-saturation surface. The existence of such a surface has been shown using computational pore-scale models (e.g., Reeves and Celia, 1996; Held and Celia, 2001; Joekar-Niasar et al., 2008; Porter et al., 2009; Joekar-Niasar and Hassanizadeh, 2012), as well as experimentally (Chen and Kibbey, 2006; Karadimitriou et al., 2014). The full interfacial area model has been used for simulating hypothetical problems (Niessner and Hassanizadeh, 2008; Pop et al., 2009), as well as experiments of horizontal redistribution of moisture in sand (Zhuang et al., 2016).

In this work, we have employed two alternative models to simulate saturation overshoot observed during one-dimensional downward infiltration of water into dry sand (Fritz, 2012). Both models employ the Richards equation, which is a combination of standard Darcy's law and the continuity equation, to describe the movement of the water phase. Also, in both models the dynamic capillarity equation is employed to give the relationship between water pressure and saturation. In the first model the

traditional hysteretic capillary pressure-saturation curves are used, whereas in the second model the interfacial area-capillary pressure-saturation surface is used to model hysteresis. We performed a series of sensitivity analyses to determine the effects of various parameters on the magnitude and extent of saturation overshoot. In the following sections, we first describe the two models used in this study, and then compare results of the two models with experimental data.

5.2 Mathematical models

First, we present common elements of the two models, namely the Richards equation and the dynamic capillarity equation. The conventional hysteresis model and the interfacial area model are described next.

5.2.1 1D-Richards equation

The mass balance equation for the water phase, combined with the Darcy-Buckingham equation, is usually used to model multiphase flow in porous media. Known as the Richards equation in one-dimensional form, the model can be written as follows:

$$\varphi \frac{\partial S^w}{\partial t} + \frac{\partial}{\partial x}\left(-\frac{k^{rw}(S^w)k}{\mu^w}\left(\frac{\partial p^w}{\partial x} - \rho^w g \right) \right) = 0 \tag{5.1}$$

where S^w is water saturation, φ is porosity, μ^w is water viscosity, ρ^w is water density, g is gravity, p^w is water pressure, k^{rw} and k denote relative and intrinsic permeabilities, respectively, t is time, and x is the vertical coordinate, assumed to be positive downward.

5.2.2 Dynamic capillarity equation

In soil physics the difference between air and water pressures is considered to be capillary pressure, given as a function of saturation. The air pressure is commonly assumed to be almost constant throughout the modelling domain. Then, taking air pressure as the reference pressure, the capillary pressure-saturation relationship is usually written as:

$$-p^w = p^c(S^w) \tag{5.2}$$

However, in this study we replace this equation with the dynamic capillarity relationship. A linear approximation for such a relationship can be formulated as follows (Hassanizadeh et al, 2002):

$$-p^w = p^c(S^w) - \tau \frac{\partial S^w}{\partial t} \tag{5.3}$$

where τ is the dynamic capillarity coefficient. Many studies have shown that τ itself may be a function of saturation. Examples are the experimental works of Bottero et al. (2011), Hou et al. (2012), Mirzaei and Das (2013), O'Carroll et al. (2005) and Goel and O'Carroll (2011) and numerical studies of Manthey et al. (2008), Bottero (2009), and Joekar-Niasar and Hassanizadeh (2011). Equation (5.3) should in principle replace Equation. (5.2), with the $p^c(S^w)$ relationship given below.

5.2.3 Conventional hysteretic model

The governing equations for this model comprise Equations (5.1) and (5.3) in combination with the full set of hysteretic capillary pressure-saturation curves. The relative permeability-saturation relationship is in principle also hysteretic. For the basic formulas we have employed van Genuchten-Mualem equations (van Genuchten, 1980) :

$$p^c(S^w) = \frac{1}{\alpha}\left[S_e^{-1/m} - 1\right]^{1/n} \tag{5.4}$$

$$k^{rw}(S^w) = (S_e)^l \left[1 - \left(1 - S_e^{1/m}\right)^m\right]^2 \tag{5.5}$$

$$S_e = \frac{S^w - S_{ir}^w}{1 - S_{ir}^w - S_r^a} \tag{5.6}$$

where S_{ir}^w, S_r^a and S_e are irreducible water saturation, residual air saturation, and effective water saturation, respectively, α and n are fitting parameters, m=1-1/n, and l was set equal to 0.5 for most simulations. The relationships for the main drainage and imbibition curves of the capillary pressure, denoted by p_{dr}^c and p_{im}^c, respectively, and the relative permeability curves, denoted by k_{dr}^{rw} and k_{im}^{rw}, are obtained by inserting corresponding values of the parameters α and n in Equations (5.4) and (5.5).

Many different approximate models have been developed for the scanning curves (cf., Kool and Parker, 1987; Parker and Lenhard, 1987). In this study, a simple play-type hysteresis model (Beliaev and Hassanizadeh, 2001; Rätz and Schweizer, 2014) was employed for both the relative permeability and capillary pressure curves. The following equations were used

$$k^{rw} = \frac{k_{im}^{rw} + k_{dr}^{rw}}{2} + \frac{k_{im}^{rw} - k_{dr}^{rw}}{2} sign(\frac{\partial S^w}{\partial t}) \tag{5.7}$$

$$p^c = \frac{p_{im}^c + p_{dr}^c}{2} + \frac{p_{im}^c - p_{dr}^c}{2} sign(\frac{\partial S^w}{\partial t}) \tag{5.8}$$

where

$$sign(\frac{\partial S^w}{\partial t}) = \begin{cases} 1 & when \frac{\partial S^w}{\partial t} > 0 \\ [-1,1] & when \quad \frac{\partial S^w}{\partial t} = 0 \\ -1 & when \frac{\partial S^w}{\partial t} < 0 \end{cases}$$

For numerical convenience we replaced the equation above by a smooth function $H_\varepsilon(\partial S^w/\partial t)$. This function was chosen so that

$$H_\varepsilon(\frac{\partial S^w}{\partial t}) = \begin{cases} 1 \quad when \frac{\partial S^w}{\partial t} > \varepsilon \\ -1 \quad when \frac{\partial S^w}{\partial t} < \varepsilon \end{cases} \tag{5.9}$$

Furthermore, $H_\varepsilon(0)=0$ and H_ε has a positive slope in the interval $(-\varepsilon, \varepsilon)$. Here ε is a small parameter that controls the way in which H_ε approximates the sign function. Since the sign function and H_ε have no physical dimension, the small parameter ε has the dimension of s^{-1}. How close are the sign function and H_ε for a given ε? To see this one needs to introduce a dimensionless time t_d by setting $t_d=t/t_{ref}$, where t_{ref} is a characteristic reference time. One has to replace ε and t in Equation (5.9) by $\varepsilon_d = \varepsilon t_{ref}$ and t_d, respectively. The scaled parameter ε_d was found to be around 10^{-4}-10^{-3}. Using H_ε in Equations (5.7) and (5.8) implies that k^{rw} and p^c vary continuously from imbibition to drainage (or vice versa).

When solving the full set of equations of the conventional hysteretic model, the value of effective saturation is not constrained. Large τ values may lead to large saturation overshoots. If effective saturation exceeds unity, Equations (5.4) and (5.5) become

meaningless. To ensure that large τ values will lead to saturation (e.g., $S^w = 1 - S_r^a$) locally in the column, we extended Equations (5.4) and (5.5) in the following way:

$$p^c(S^w) = \frac{\alpha^*}{\varepsilon_d}(1 - S_r^a - S^w) \quad k^{rw}(S^w) = 1 \tag{5.10}$$

for $S^w > 1 - S_r^a$. In Equation (5.10), α^* represents the averaged parameter of the drainage-imbibition relationship (see Table 5.1).

In summary, in the conventional hysteretic model, the governing equations consist of Equations (5.1), (5.3) and (5.8)-(5.10), combined with auxiliary Equations (5.4)-(5.7).

5.2.4 Interfacial area model

For this model we still employ Equations (5.1) and (5.3). However, Equations (5.4)-(5.9) for capillary pressure and relative permeability as given in the previous section, are now replaced by a new constitutive equation in terms of the air-water specific interfacial area, denoted by a^{wa} (Hassanizadeh and Gray, 1993b). This new variable is defined as the amount of air-water interfacial area per unit volume of the porous medium. It has been shown that each equilibrium p^c-S^w point (primary, main, or scanning) corresponds to a point on a unique p^c-S^w-a^{wa} surface (Chen and Kibbey, 2006; Joekar-Niasar and Hassanizadeh, 2011, 2012; Karadimitriou et al., 2014). This means that multiple p^c-S^w loops are replaced by a single three-dimensional p^c-S^w-a^{wa} surface. Similarly, the hysteretic relationship between relative permeability (k^{rw}) and saturation (S^w) can be replaced by a k^{rw}-S^w-a^{wa} surface (Joekar-Niasar et al., 2008).

Since there were no experimental data available for the set of infiltration experiments modelled here, we employed a numerical approach proposed by Bradford and Leij (1997) to generate the p^c-S^w-a^{wa} surface. A similar method was used to generate the k^{rw}-S^w-a^{wa} surface. Details are given in Appendix D. For the p^c-S^w-a^{wa} surface, the following power function proposed by Joekar-Niasar and Hassanizadeh (2012) was used:

$$a^{wa}\left(S^w, p^c\right) = \gamma_1 S^w \left(1 - S^w\right)^{\gamma_2} \left(\alpha p^c\right)^{\gamma_3} \tag{5.11}$$

where γ_1, γ_2 and γ_3 are fitting parameters. Here, α is the same parameter as in the van Genuchten-Mualem model. This parameter is used here to make the last term on the right-hand side dimensionless. For our fitting purposes, we used the value of α of the primary imbibition curve.

For the k^{rw}-S^{w}-a^{wa} surface, the following formula was employed:

$$k^{rw}\left(S^{w}, a^{wa}\right) = S^{w\left(-\lambda_1 a^{wa}+\lambda_2\right)} \tag{5.12}$$

where λ_1 and λ_2 are fitting parameters. Equation (5.12) was proposed based on the formula for k^{rw} in the Brooks-Corey-Burdine model (Brooks and Corey, 1964), which is simply a power function of saturation, with the value of the exponent being different for drainage or imbibition. In Equation (5.12), different values of specific interfacial area (a^{wa}) during imbibition and drainage result in different values of the exponent for different paths.

For the air-water specific interfacial area, an evolution equation must be provided. Assuming that the air-water interfacial mass density is constant, the following equation can be given (Hassanizadeh, 2015):

$$\frac{\partial a^{wa}}{\partial t} + \frac{\partial\left(a^{wa} w^{wa}\right)}{\partial x} = E^{wa} \tag{5.13}$$

where w^{wa} is the macroscopic flux of the specific interfacial area. This flux is given by a Darcy-type equation (Hassanizadeh, 2015):

$$w^{wa} = -k^{wa}\left(\frac{\partial a^{wa}}{\partial x} + \Omega\frac{\partial S^{w}}{\partial x}\right) \tag{5.14}$$

in which k^{wa} is the interfacial permeability, including surface tension, and Ω is another material coefficient. E^{wa} is the net production rate of the specific interfacial area, for which the following approximation was developed by Zhuang et al. (2016):

$$E^{wa} = -L\frac{\partial a^{wa}}{\partial p^{c}}\frac{\partial S^{w}}{\partial t} \tag{5.15}$$

where L is a material coefficient.

Recent numerical and experimental studies by Joekar-Niasar and Hassanizadeh (2011) and Karadimitriou et al. (2014) have shown that the value of the interfacial permeability coefficient is very small. As a result, w^{wa} and the corresponding term in Equation (5.13) attain small values and can be disregarded. This means that combination of Equations (5.13) and (5.15) yields:

$$\frac{\partial a^{wa}}{\partial t} = -L\frac{\partial a^{wa}}{\partial p^{c}}\frac{\partial S^{w}}{\partial t} \tag{5.16}$$

For a fixed point x, Equation (5.16) indicates that the relationship between p^c and S^w is specified for a given set of initial conditions (p_0^c, S_0^w), and remains unchanged at all later times during the imbibition or drainage processes (Pop et al., 2009).

To introduce hysteretic behavior in the interfacial area model, the value of L in Equation (5.15) was assumed to depend on the sign($\partial S^w/\partial t$) as well. As in Equations (5.7) and (5.8), we considered

$$L = \frac{L_{im} + L_{dr}}{2} + \frac{L_{im} - L_{dr}}{2} sign(\frac{\partial S^w}{\partial t}) \tag{5.17}$$

where L_{im} and L_{dr} denote L values for imbibition and drainage, respectively. As before, we used the approximation $H_\varepsilon(\partial S^w/\partial t)$ in Equation (5.17). Values for L_{im} and L_{dr} were fitted to the experimental data.

In summary, we solved the set of Equations (5.1), (5.3) and (5.16) for the interfacial area model, combined with auxiliary Equations (5.11), (5.12), and (5.17).

5.3 Description of experiments

Here, we describe 1D water infiltration experiments performed by Fritz (2012). The experiments were designed to characterize saturation overshoot behavior during water infiltration into relatively dry sand. Clean sand was uniformly packed into a Plexiglas column of 50-cm length and 1.0 cm in diameter. Water was delivered to the top of the vertical column at a pre-specified constant flow rate. Saturation at a position 20 cm below the inlet was measured using gamma transmission during the entire experiments. Water pressures were measured simultaneously at multiple locations along the domain using electrical sensors. The influence of initial conditions and applied water flowrates were investigated for three different types of sand. In this work we mainly focus on experiments performed on coarse sand, with d_{50}=0.79 mm, at different inflow rates.

The capillary pressure saturation curves of the sand were measured using a multistep hanging water column method. Figure 5.2 shows the measured primary imbibition and main drainage curves, as well as the fitted curves based on van Genuchten formula, Equation (5.4). Saturated conductivity was measured by the constant head method, and an average value of 5.61×10^{-3} m/s was found. We have summarized all hydraulic parameters in Table 5.1.

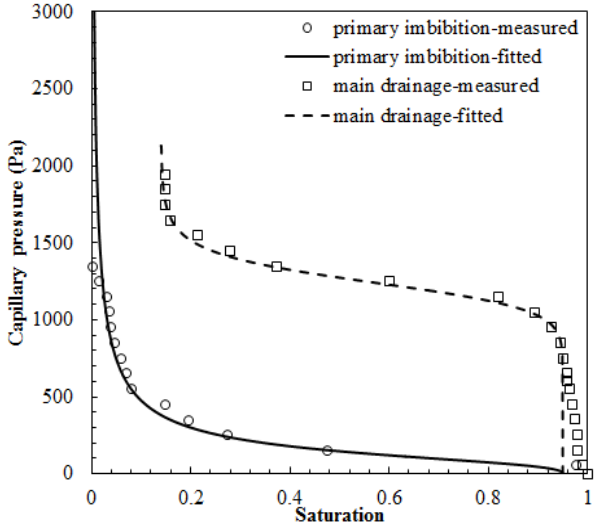

Figure 5.2 Measured and fitted van Genuchten primary imbibition and main drainage curves (Fritz, 2012).

Table 5.1 Measured soil properties and parameter values

Parameters	Unit	Value
Porosity, φ	-	0.4
Water density, ρ^w	kg m^{-3}	1×10^{3}
Water viscosity, μ^w	Pa·s	1×10^{-3}
Intrinsic permeability, k	m^2	6.43×10^{-10}
Main drainage retention exponent, n	-	13.84
Main drainage retention parameter, α	Pa^{-1}	8.0×10^{-4}
Primary imbibition retention exponent, n	-	2.58
Primary imbibition retention parameter, α	Pa^{-1}	8.6×10^{-3}
Irreducible water saturation, S_{ir}^{w}	-	0.14
Residual air saturation, S_{r}^{a}	-	0.05

Different experiments were conducted with different constant inflow rates, ranging from 7.5×10^{-6} to 4.3×10^{-5} m/s, and different initial saturations. Figure 5.3a shows saturation breakthrough curves for three different inflow rates at zero initial saturation.

Figure 5.3b presents saturation curves for three different initial saturation values and a fixed inflow rate of 4.3×10^{-5} m/s. As can be seen, saturation overshoot existed, even for a relatively small flow rate, when the soil was initially dry. For small flow rates, the peak showed a distinct plateau, while the fast flow rates exhibited only sharp peaks (Figure 5.3a). The overshoot height decreased for higher initial saturations and vanished for an initial saturation of 0.1, close to irreducible saturation (Figure 5.3b).

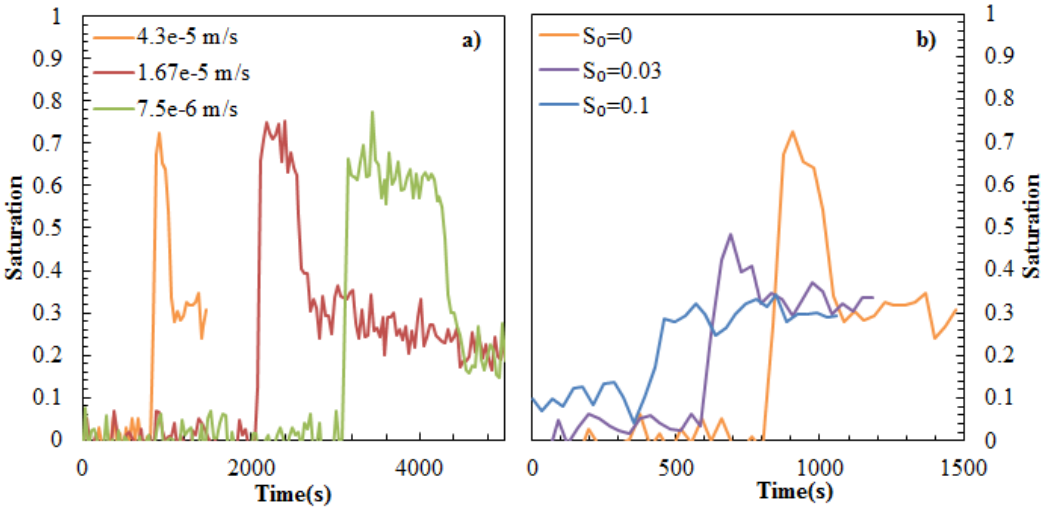

Figure 5.3 Measured saturation breakthrough curves at 20 cm, in initially dry soil with different flow rates (a) and different initial saturations at flow rate of 4.3×10^{-5} m/s (b) (Fritz, 2012).

5.4 Numerical results

The equations for both the conventional and interfacial area models were solved using the commercial simulation package COMSOL Multiphysics 5.0. A small grid size of 1×10^{-4}m and a maximum time step of 0.1s were chosen to obtain mesh-independent solutions. A residual error of 1×10^{-8} was used to achieve accurate solutions. The modelling domain was 0.5 m long. The upper boundary condition was specified to be a constant inflow rate, while the lower boundary condition was set equal to the initial saturation. For the cases with initially dry sand, a very small value of 0.01 was assigned as the initial saturation. For the interfacial area model simulations we took the initial value of the capillary pressure from the primary imbibition curve corresponding to the initial saturation value. For all numerical simulations, we used saturation breakthrough curves at 20 cm in order to compare with experimental data. The

experiments were simulated using the fitted parameters given in Tables 5.1 and 5.2. The corresponding p^c-S^w-a^{wa} and k^{rw}-S^w-a^{wa} surfaces are shown in Figure 5.4.

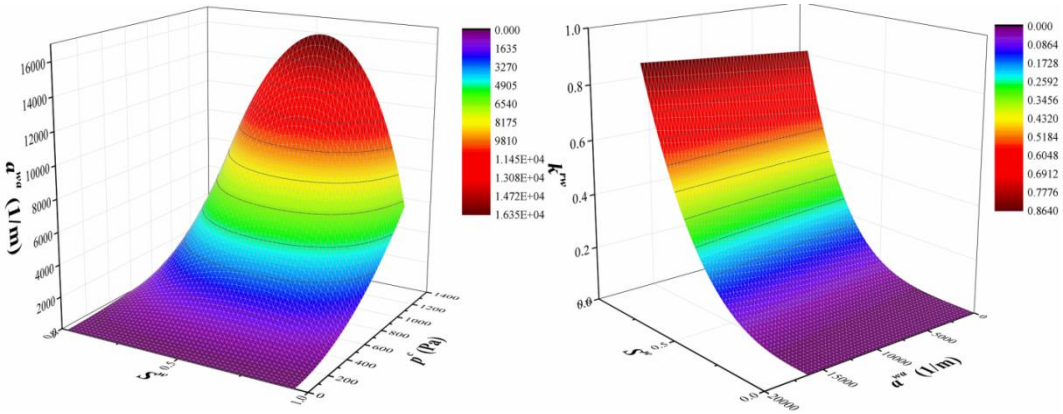

Figure 5.4 Three-dimensional surfaces of p^c-S^w-a^{wa} (left) and k^{rw}-S^w-a^{wa} (right)

Table 5.2 Values of the coefficients in Equations (5.11) and (5.12)

Parameter	Value	Standard error
γ_1 (1/m)	582	21
γ_2	0.7	0.05
γ_3	1.9	0.02
R^2, Equation (5.11)	0.95	
λ_1 (m)	7.0×10^{-5}	6.7×10^{-6}
λ_2	4.0	0.14
R^2, Equation (5.12)	0.96	

5.4.1 Sensitivity analysis

First we performed a sensitivity analysis of the basic model, i.e., the 1D Richards equation with dynamic capillarity effects, in order to investigate the effects of various parameters. These were the dynamic capillarity coefficient τ, the exponent l appearing in Equation (5.5) for the relative permeability, and initial saturation. We compared all results mainly in terms of two aspects: the shape (width and height) of saturation overshoot, and the arrival time of the water front. Results of the sensitivity analyses are presented in Figure 5.5.

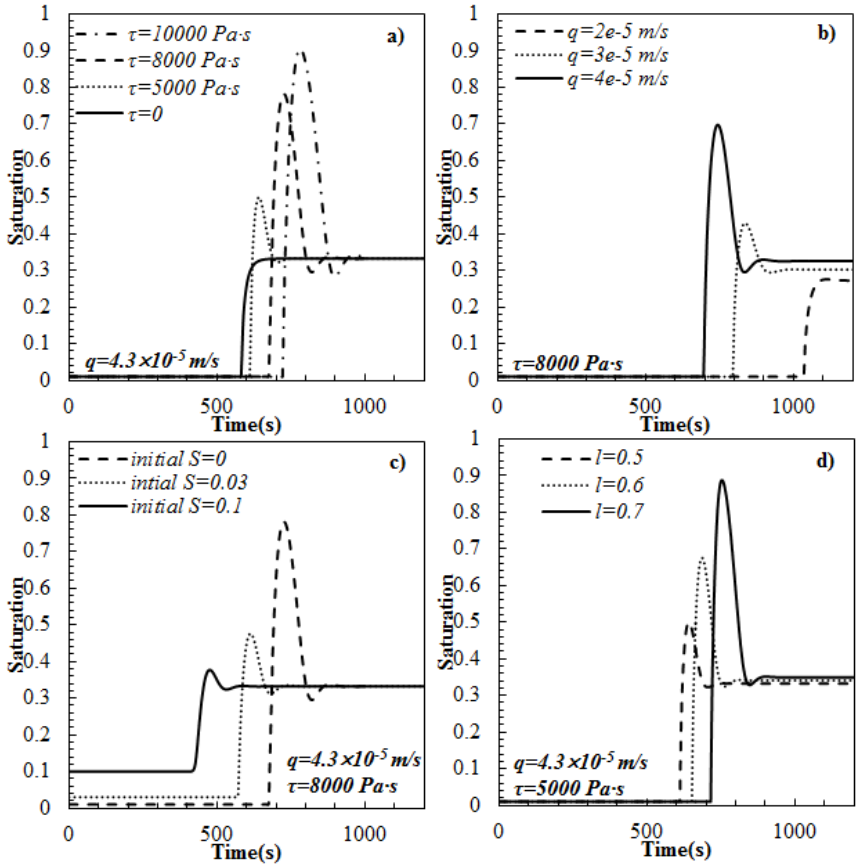

Figure 5.5 Saturation breakthrough curves for different parameters

As can be seen in Figure 5.5a, the dynamic capillarity coefficient τ has a strong effect on the shape and arrival time of saturation overshoot. Obviously, a monotonic front was found for τ=0. It is evident that the conventional equilibrium theory of capillarity is not capable to capture the observed non-monotonic saturation behavior, thus echoing previous mathematical analyses and numerical studies. The coefficient τ plays the role of a damping factor. Increasing the value of τ leads to more overshoot and a delay in arrival time (see Figure 5.5a). As indicated by experiments, the inflow rate and initial saturation also impact the non-monotonicity. For this reason we performed a series of simulations using inflow rates ranging from 2×10^{-5} to 4×10^{-5} m/s (see Figure 5.5b), and initial saturations 0, 0.03 and 0.1 (see Figure 5.5c). For a constant τ value, reducing the inflow rate leads to a less saturation overshoot (see Figure 5.5b). The increase in initial saturation resulted in an earlier arrival of the front and a lower saturation overshoot, consistent with the experiments of Frits (2012). We also varied

the value of the exponent l in the relative permeability Equation (5.5). Results are shown in Figure 5.5d. Decreasing the relative permeability k^{rw} (i.e., increasing the value of exponent l) leads to higher saturation overshoot and later arrival of the front, a damping effect similar to the effect of τ.

Next we studied the effect of including hysteresis in the capillary pressure p^c and/or the relative permeability k^{rw}. Figure 5.6 shows saturation breakthrough curves obtained with the conventional model. As can be seen, including hysteresis has no effect on the results if τ=0. The reason is that when τ=0, a monotonous saturation distribution will be obtained; i.e. the domain will undergo imbibition only. For τ=10000 Pa·s, a sharp saturation overshoot is obtained if no hysteresis is included. When we account for hysteresis in capillary pressure and/or relative permeability, the overshoot shows a plateau (see Figure 5.6).

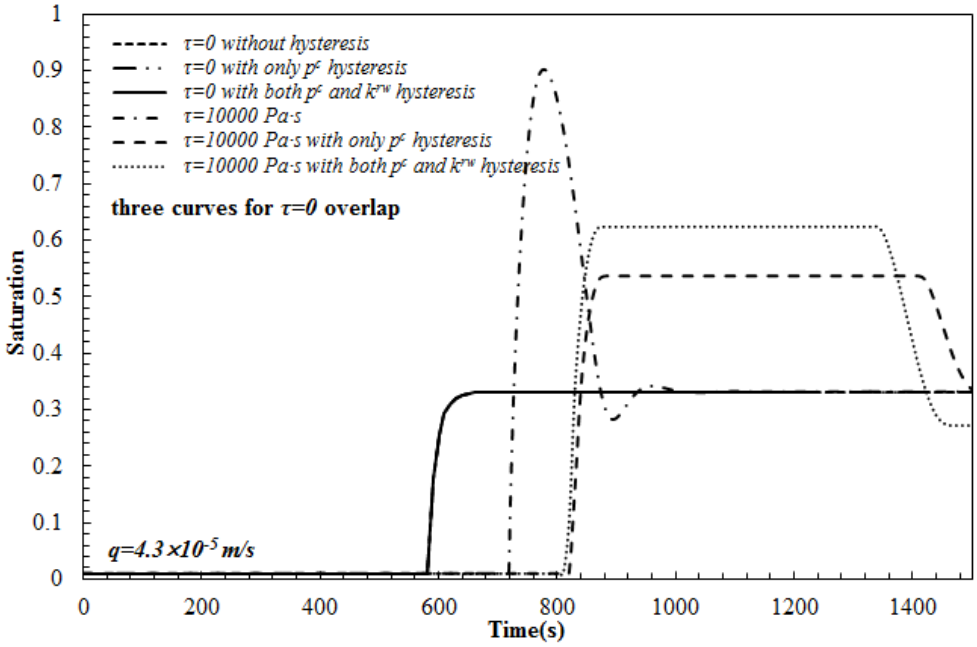

Figure 5.6 Saturation breakthrough curves simulated with the conventional model, with or without hysteresis

Finally, we compared the conventional model (with hysteresis) to the interfacial area model. Typical results are shown in Figure 5.7. The three breakthrough curves for the conventional model are the same as those in Figure 5.6 (with τ=10000 Pa·s). The interfacial area model (employing a p^c-S^w-a^{wa} surface) shows a sharp overshoot. If instead of a single k^{rw}-S^w curve, a k^{rw}-S^w-a^{wa} surface is used (i.e., to account for

hysteresis in k^{rw}), then the overshoot height decreases and the moisture front arrives earlier. This is because we effectively allow for a higher relative permeability value for the imbibition stage, when hysteresis is included.

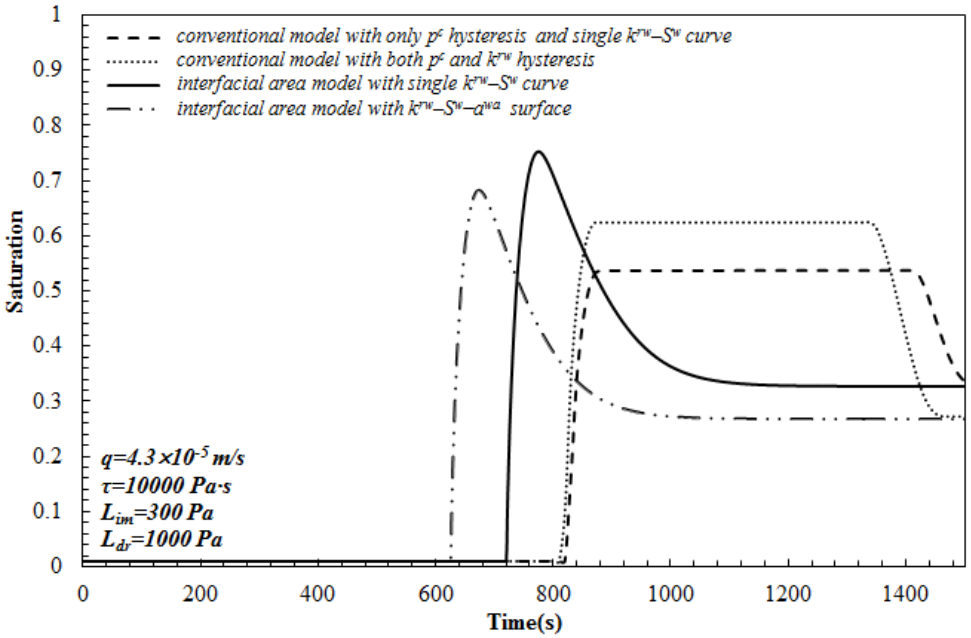

Figure 5.7 Breakthrough curves simulated with different models, but with the dynamic capillarity equation

The difference in results obtained with the conventional and interfacial area models can be partly explained by different scanning curves being followed in the two models. Figure 5.8 shows scanning curves for the capillary pressure for breakthrough curves at x=20 cm (results shown in Figure 5.7). The solid and dashed lines are primary imbibition and main drainage curves, respectively, as measured experimentally. According to the simulations, saturation at x=20 cm starts from the initial saturation, and increases along the primary imbibition curve until the moisture front passes. Saturation then decreases along the drainage scanning curve, which is shown by diamond shaped symbols. In case of the conventional model, the primary drainage curve is followed exactly and the scanning curve is a straight vertical line, and then the main drainage is followed. In case of the interfacial area model, a path almost parallel to primary imbibition is followed (shown by + symbols in Figure 5.8b), but then a totally different drainage scanning curve is followed (shown by diamond symbols in Figure 5.8b).

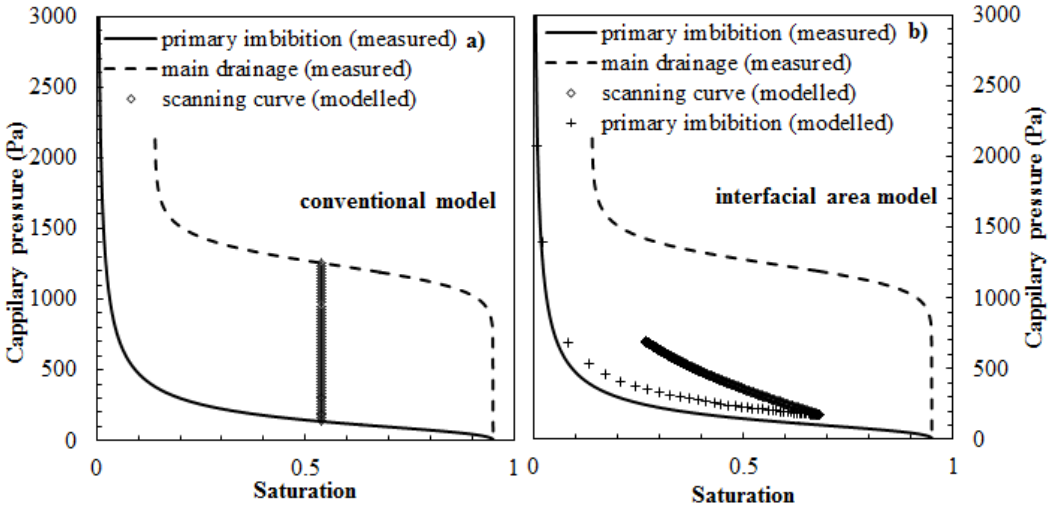

Figure 5.8 Corresponding capillary curves in the conventional model (a) and the interfacial area model (b)

5.4.2 Comparison with experiments

Next we employed the two models to simulate the experiments by Fritz (2012). Simulation results from the two models were compared with experimental data for an inflow rate of 4.3×10^{-5} m/s. The combination that fitted the data best (i.e. the conventional model with both p^c and k^{rw} hysteresis, and the interfacial area model with a p^c-S^w-a^{wa} surface) was chosen to simulate other experiments with different conditions. For the interfacial area model, the inflow rate q was adjusted as well, to obtain a good fit of the arrival time of saturation overshoot as measured in the experiments.

Both simulated and experimental results are shown in Figure 5.9. Experimental data are shown by symbols, while simulated results from the conventional and interfacial area models are presented by dashed and solid lines, respectively. Values of all fitting parameters in the simulations are given in Table 5.3. Results obtained with the conventional model deviated substantially from the data, whereas results from the interfacial area model show much better agreement, albeit with adjustment of the inflow rate. Values of L_{im} and L_{dr} in Equation (5.17) were fixed in all simulations, thus obtaining a similar primary imbibition curve as measured and reasonable scanning curves with the interfacial area model.

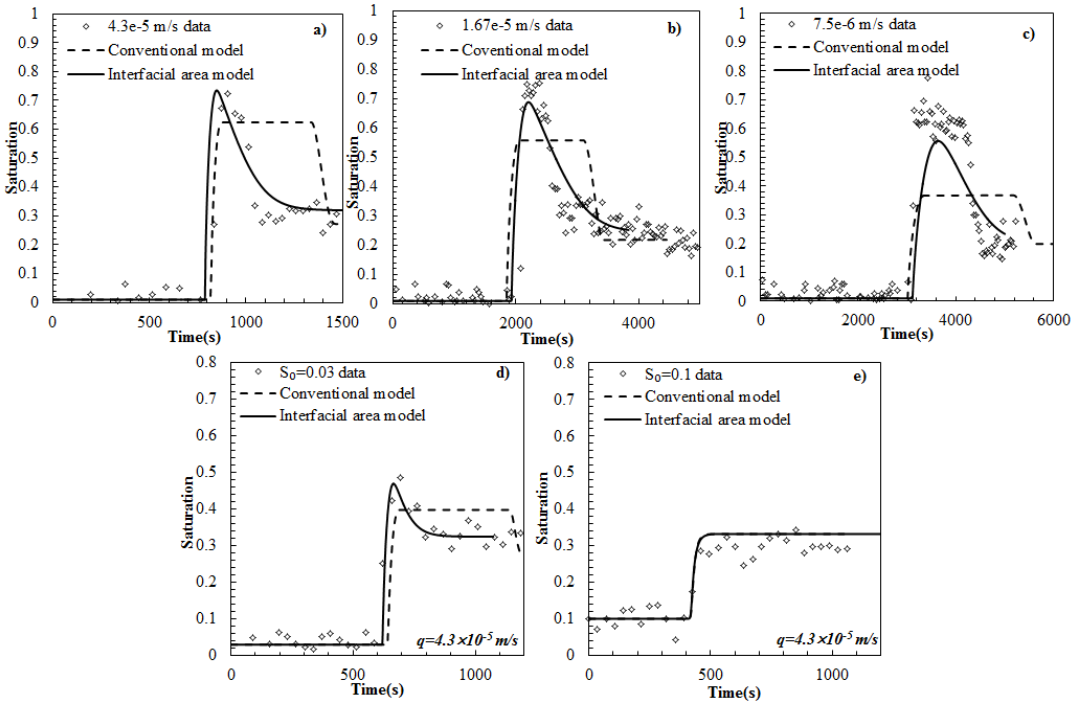

Figure 5.9 Observed saturation breakthrough curves at 20 cm (diamonds) and fitted curves obtained with the conventional model (dashed line) and the interfacial area model (solid line)

Table 5.3 Values of parameters in the conventional and interfacial area model

Boundary conditions	**Initial saturation**	**Conventional model**	**Interfacial area model**			
Flowrate (m/s)	S_0 (-)	τ (Pa·s)	Flowrate adjusted by	τ (Pa·s)	L_{im} (Pa)	L_{dr} (Pa)
4.30×10^{-5}	0	1×10^{4}	-7%	1.3×10^{4}	390	1300
1.67×10^{-5}	0	6×10^{4}	-7%	1×10^{5}	390	1300
7.50×10^{-6}	0	1.4×10^{5}	0	2.5×10^{5}	390	1300
4.30×10^{-5}	0.03	8×10^{3}	-7%	1×10^{4}	390	1300
4.30×10^{-5}	0.1	1×10^{3}	0	1×10^{3}	390	1300

5.5 Discussion and conclusions

In this work, we employed two different unsaturated flow models to simulate results of a laboratory experiment on water infiltration into an almost dry soil. The two models are both based on the Richards equation and a dynamic capillarity equation. In one model, traditional hysteresis equations for capillary pressure and relative permeability curves were used; we referred to this model as "conventional hysteretic model". The other model was based on using three-dimensional surfaces of p^c-S^w-a^{wa} and k^{rw}-S^w-a^{wa}; this model was referred to as "interfacial area model".

Results of all simulations with the conventional model deviated substantially from experimental data. Without the dynamic capillarity term, completely monotonic saturation profiles were obtained, regardless of what type of hysteresis formulation was included. This is consistent with previous studies by other researchers. When including the dynamic term, the conventional model gave a sharp saturation overshoot if no hysteresis was included. When accounting for hysteresis in capillary pressure and/or relative permeability, then the overshoot showed a plateau structure. With a wide saturation overshoot, the results obtained with the conventional model never showed good agreement with data.

The interfacial area model could capture saturation overshoots observed in the experiments with different conditions very well. By fitting the values of L_{im} and L_{dr} in Equation (5.17), the projected capillary curve for primary imbibition, as obtained with the interfacial area model, gave good agreement with measured values. To some extent, this indicates that the coefficient L in the production term is determined by material properties and the history of the flow processes involved, similar to the capillary curves.

We emphasize that still some uncertainties exist in the interfacial area model. The coefficients γ_1, γ_2 and γ_3 in Equation (5.11) of the interfacial area model were somehow pre-determined, owing to fitting of calculated data derived from the measurements. Different values were given to the coefficient L in Equation (5.15) to create different projected capillary curves (imbibition or drainage). Further investigations are also needed to understand the best parametrization of the production term

The value of the dynamic capillarity τ was obtained by fitting experimental data using both models. The fitted values of τ were found to vary between 10^3 and 2.5×10^5 Pa·s. In our work, the value of τ was assumed to be a constant. Further studies are needed to determine the dependence of τ on saturation.

5.6 Appendix D: Reconstruction of interfacial area surface

The specific interfacial area was never measured as part of the experiments used in our simulations. Our assumption was that the projection of the interfacial area surface onto the p^c-S^w plane should give the full set of curves found in the hysteresis loops. Hence, the inverse argument would be that hysteretic capillary pressure curves should provide the p^c-S^w-a^{wa} surface.

Procedures for estimating the p^c-S^w-a^{wa} surface from p^c-S^w curves have been proposed, among others, by Leverett (1941), Bradford and Leij (1997) and Grant and Gerhard (2007). The underlying assumption in these approaches is that, during quasi-static drainage or imbibition processes, changes in interfacial area are brought about by mechanical work done (e.g. by fluid pressures) on the system. The magnitude of this mechanical work is related to the area under the p^c-S^w curves. This can only be an approximation and other effects may need to be included (e.g., Grant and Gerhard, 2007). But the approximation suffices for our purposes in that the approximate reconstruction of p^c-S^w-a^{wa} surface is done such that measured primary imbibition and main drainage curves can be reproduced from that surface.

In an air-water system, the external work needed to effectuate a change ΔS^w=-ΔS^a, can be written as:

$$\Delta W_{ex} = p^a \varphi V \Delta S^a + p^w \varphi V \Delta S^w = -p^c \varphi V \Delta S^w \tag{D1}$$

where W_{ex} is the external work, V is the bulk volume of the porous medium, and p^a and S^a are air pressure and air saturation, respectively.

Assuming that the solid interface is perfectly wetted by water, external work will be spent on creating air-water interfaces. The energy associated with the change of air-water interfaces is:

$$\Delta E = \sigma^{wa} \Delta A^{wa} \tag{D2}$$

which should be equal to ΔW_{ex}.

This leads to the following equation for the specific interfacial area a^{wa}=A^{wa}/V:

$$a^{wa} = \frac{\varphi}{\sigma^{wa}} \int_{S^w}^{1-S_r^a} p_c(z) dz \tag{D3}$$

where σ^{wa} is air-water interfacial tension, and z is a dummy variable.

We have fitted measured capillary pressure curves with the van Genuchten formula, Equation (5.4). Substitution of that equation in Equation (D3) allowed us to calculate a^{wa} as a function of S^w and p^c. We chose 50 saturation values with equal intervals, from 0 to 0.95 ($= 1 - S_r^a$) for imbibition, and from 0.14 ($= S_{ir}^w$) to 0.95 ($= 1 - S_r^a$) for main

drainage. Values of the specific interfacial area a^{wa} and capillary pressure p_c based on Equation (D3) and Equation (5.4), respectively, were calculated subsequently. Next we fitted the resulting p^c-S^w-a^{wa} array with the power function of Equation (5.11), to obtain the corresponding p^c-S^w-a^{wa} surface for this sand.

The corresponding values of relative permeability k^{rw} were calculated based on Equation (5.5) for the same set of saturation values. The k^{rw}-S^w-a^{wa} array was fitted with Equation (5.12) to obtain k^{rw}-S^w-a^{wa} surface.

Acknowledgements

We gratefully acknowledge M.Th. van Genuchten, A. Leijnse and A. Raoof for helpful discussions. The first author is supported by the China Scholarship Council (No. 201206380076). The second author has received funding from the European Research Council under the European Union's Seventh Framework Program (FP/2007-2013)/ERC Grant Agreement No. 341225.

References

Baker, R.S., and D. Hillel. 1990. Laboratory tests of a theory of fingering during infiltration into layered soils. Soil Sci. Soc. Am. J. 54(1): 20–30.

Bauters, T.W.J., T.S. Steenhuis, D.A. DiCarlo, J.L. Nieber, L.W. Dekker, C.J. Ritsema, J.-Y. Parlange, and R. Haverkamp. 2000. Physics of water repellent soils. J. Hydrol. 231–232: 233–243.

Beliaev, A.Y., and S.M. Hassanizadeh. 2001. A theoretical model of hysteresis and dynamic effects in the capillary relation for two-phase flow in porous media. Transp. Porous Media 43(1): 487–510.

Bottero, S. 2009. Advances in the theory of capillarity in porous media. Ph.D. thesis, Utrecht University, Geologica Ultreietina, 314, 200 pp.

Bottero, S., S.M. Hassanizadeh, P.J. Kleingeld, and T.J. Heimovaara. 2011. Nonequilibrium capillarity effects in two-phase flow through porous media at different scales. Water Resour. Res. 47: W10505.

Bradford, S.A., and F.J. Leij. 1997. Estimating interfacial areas for multi-fluid soil systems. J. Contam. Hydrol. 27(1–2): 83–105.

Brooks, R., and A. Corey. 1964. Hydraulic properties of porous media. Hydrol. Pap. Colo. State Univ. 3, 37 pp.

Chapwanya, M., and J.M. Stockie. 2010. Numerical simulations of gravity-driven fingering in unsaturated porous media using a nonequilibrium model. Water Resour. Res. 46: W09534.

Chen, L., and T.C.G. Kibbey. 2006. Measurement of air-water interfacial area for multiple hysteretic drainage curves in an unsaturated fine sand. Langmuir 22(16): 6874–6880.

COMSOL. 2014. COMSOL Multiphysics 5.0. COMSOL Inc., Burlington, MA.

Cuesta, C., and J. Hulshof. 2003. A model problem for groundwater ow with dynamic capillary pressure : stability of travelling waves. 52: 1199–1218.

Cueto-Felgueroso, L., and R. Juanes. 2008. Nonlocal interface dynamics and pattern formation in gravity-driven unsaturated flow through porous media. Phys. Rev. Lett. 101(24): 244504.

DiCarlo, D.A. 2004. Experimental measurements of saturation overshoot on infiltration. Water Resour. Res. 40: W04215.

DiCarlo, D.A. 2005. Modeling observed saturation overshoot with continuum additions to standard unsaturated theory. Adv. Water Resour. 28(10): 1021–1027.

DiCarlo, D.A. 2007. Capillary pressure overshoot as a function of imbibition flux and initial water content. Water Resour. Res. 43: W08402.

Diment, G., and K. Watson. 1985. Stability analysis of water movement in unsaturated porous materials: 3. Experimental studies. Water Resour. Res. 21(7): 979–984.

van Duijn, C.J., G.J.M. Pieters, and P.A.C. Raats. 2004. Steady flows in unsaturated soils are stable. Transp. Porous Media 57(2): 215–244.

Egorov, A.G., R.Z. Dautov, J.L. Nieber, and A.Y. Sheshukov. 2002. Stability analysis of traveling wave solution for gravity-driven flow. Dev. Water Sci. 47(C): 121–128.

Eliassi, M., and R.J. Glass. 2001. On the continuum-scale modeling of gravity-driven fingers in unsaturated porous media : The inadequacy of the Richards equation with standard monotonic constitutive relations and hysteretic equations of state. Water Resour. Res. 37(8): 2019–2035.

Eliassi, M., and R.J. Glass. 2002. On the porous-continuum modeling of gravity-driven fingers in unsaturated materials: Extension of standard theory with a hold-back-pile-up effect. Water Resour. Res. 38(11): 16-1-16–11.

Fritz, S. 2012. Experimental investigations of water infiltration into unsaturated Soil - analysis of dynamic capillarity effects.

Geiger, S.L., and D.S. Durnford. 2000. Infiltration in homogeneous sands and a mechanistic model of unstable flow. Soil Sci. Soc. Am. J. 64(2): 460–469.

van Genuchten, M.T. 1980. A closed-form equation for predicting the hydraulic conductivity of unsaturated soils1. Soil Sci. Soc. Am. J. 44(5): 892–898.

Glass, R.J., S. Cann, J. King, N. Baily, J.-Y. Parlange, and T.S. Steenhuis. 1990. Wetting front instability in unsaturated porous media: A three-dimensional study in initially dry Sand. Transp. Porous Media 5(3): 247–268.

Glass, R.J., T.S. Steenhuis, and J.-Y. Parlange. 1989a. Wetting front instability 2.

Experimental determination of relationships between system behavior in initially dry porous media. Water Resour. Res. 25(6): 1195–1207.

Glass, R.J., T.S. Steenhuis, and J.-Y. Parlange. 1989b. Mechanism for finger persistence in homogeneous, unsaturated, porous media: Theory and verification. Soil Sci. 148(1): 60–70.

Goel, G., and D.M. O'Carroll. 2011. Experimental investigation of nonequilibrium capillarity effects: Fluid viscosity effects. Water Resour. Res. 47(9): 1–15.

Grant, G.P., and J.I. Gerhard. 2007. Simulating the dissolution of a complex dense nonaqueous phase liquid source zone: 1. Model to predict interfacial area. Water Resour. Res. 43(12): 1–14.

Hassanizadeh, S.M. 2015. Advanced Theories of Two-Phase Flow in Porous Media. p. 47–62. *In* Handbook of Porous Media, Third Edition. CRC Press.

Hassanizadeh, S.M., M.A. Celia, and H.K. Dahle. 2002. Dynamic effect in the capillary pressure-saturation relationship and its impacts on unsaturated flow. Vadose Zone J. 1(1): 38–57.

Hassanizadeh, S.M., and W.G. Gray. 1990. Mechanics and thermodynamics of multiphase flow in porous media including interphase boundaries. Adv. Water Resour. 13(4): 169–186.

Hassanizadeh, S.M., and W.G. Gray. 1993a. Thermodynamic basis of capillary pressure in porous media. Water Resour. Res. 29(10): 3389–3405.

Hassanizadeh, S.M., and G.W. Gray. 1993b. Toward an improved description of the physics of two-phase flow. Adv. Water Resour. 16: 53–67.

Hill, D.E., and J.-Y. Parlange. 1972. Wetting Front Instability in Layered Soils. Soil Sci. Soc. Am. J. 36(October): 697–702.

Hou, L., L. Chen, and T.C.G. Kibbey. 2012. Dynamic capillary effects in a small-volume unsaturated porous medium: Implications of sensor response and gas pressure gradients for understanding system dependencies. Water Resour. Res. 48: W11522.

Joekar-Niasar, V., and S.M. Hassanizadeh. 2011. Specific interfacial area: The missing state variable in two-phase flow equations? Water Resour. Res. 47: W05513.

Joekar-Niasar, V., and S.M. Hassanizadeh. 2012. Uniqueness of specific interfacial area-capillary pressure-saturation relationship under non-equilibrium conditions in two-phase porous media flow. Transp. Porous Media 94: 465–486.

Joekar-Niasar, V., S.M. Hassanizadeh, and A. Leijnse. 2008. Insights into the Relationships among capillary pressure, saturation, interfacial area and relative permeability using pore-network modeling. Transp. Porous Media 74: 201–219.

Karadimitriou, N.K., S.M. Hassanizadeh, V. Joekar-Niasar, and P.J. Kleingeld. 2014. Micromodel study of two-phase flow under transient conditions: Quantifying effects of specific interfacial area. Water Resour. Res. 50(10): 8125–8140.

Kool, J.B., and J.C. Parker. 1987. Development and evaluation of closed-form expressions for hysteretic soil hydraulic properties. Water. Resour. Res. 23(1): 105–114.

Lehmann, P., F. Stauffer, C. Hinz, O. Dury, and H. Fluhler. 1998. Effect of hysteresis on water flow in a sand column with a fluctuating capillary fringe. J. Contam. Hydrol. 33: 81–100.

Leverett, M. 1941. Capillary behavior in porous solids. Trans. AIME 142(1): 152–169.

Liu, Y., T.S. Steenhuis, and J.-Y. Parlange. 1994a. Formation and persistence of fingered flow fields in coarse grained soils under different moisture contents. J. Hydrol. 159(1–4): 187–195.

Liu, Y., T.S. Steenhuis, and J.-Y. Parlange. 1994b. Closed-form solution for finger width in sandy soils at different water contents. Water Resour. Res. 30(4): 949–952.

Lu, T.X., J.W. Biggar, and D.R. Nielsen. 1994a. Water movement in glass bead porous media: 2. Experiments of infiltration and finger flow. Water Resour. Res. 30(12): 3283–3290Available at http://doi.wiley.com/10.1029/94WR00998.

Lu, T.X., J.W. Biggat, and D.R. Nielsen. 1994b. Water movement in glass bead porous media 1. Experiments of capillary rise and hysteresis. Water Resour. Res. 30(12): 3275–3281.

Manthey, S., S.M. Hassanizadeh, R. Helmig, and R. Hilfer. 2008. Dimensional analysis of two-phase flow including a rate-dependent capillary pressure–saturation relationship. Adv. Water Resour. 31: 1137–1150.

Mirzaei, M., and D.B. Das. 2013. Experimental investigation of hysteretic dynamic effect in capillary pressure-saturation relationship for two-phase flow in porous media. AIChE J. 59(10): 3958–3974.

Nieber, J.L. 1996. Modeling finger development and persistence in initially dry porous media. Geoderma 70(2–4): 207–229.

Nieber, J., A. Sheshukov, A. Egorov, and R. Dautov. 2003. Non-equilibrium model for gravity-driven fingering in water repellent soils: Formulation and 2D simulations. p. 245–257. *In* Soil Water Repellency: Occurrence, Consequences, and Amelioration. Elsevier Sci.

Niessner, J., and S.M. Hassanizadeh. 2008. A model for two-phase flow in porous media including fluid-fluid interfacial area. Water Resour. Res. 44(8): W08439.

O'Carroll, D.M., T.J. Phelan, and L.M. Abriola. 2005. Exploring dynamic effects in capillary pressure in multistep outflow experiments. Water Resour. Res. 41(11): 1–14.

Otto, F. 1997. L1-Contraction and uniqueness for unstationary saturated-unsaturated porous media flow. Adv. Math. Sci. Appl. 7: 537–553.

Parker, J.C., and R.J. Lenhard. 1987. A model for hysteretic constitutive relations governing multiphase flow 1. Saturation-pressure relations. Water Resour. Res. 23(12): 2187–2196.

Pop, I.S., C.J. van Duijn, J. Niessner, and S.M. Hassanizadeh. 2009. Horizontal redistribution of fluids in a porous medium: The role of interfacial area in modeling hysteresis. Adv. Water Resour. 32(3): 383–390.

Rätz, A., and B. Schweizer. 2014. Hysteresis models and gravity fingering in porous media. ZAMM - J. Appl. Math. Mech. / Zeitschrift für Angew. Math. und Mech. 94(7–8): 645–654.

Sander, G.C., O.J. Glidewell, and J. Norbury. 2008. Dynamic capillary pressure, hysteresis and gravity-driven fingering in porous media. J. Phys. Conf. Ser. 138: 12023.

Selker, J.S., P. Leclerq, J.-Y. Parlange, and T.S. Steenhuis. 1992. Fingered flow in two

dimensions 1. Measurement of matric potential. Water Resour. Res. 28(9): 2513–2521.

Stauffer, F. 1978. Time dependence of the relations between capillary pressure, water content and conductivity during drainage of porous media. p. 3–35. *In* IAHR symposium on scale effects in porous media, Thessaloniki, Greece.

Stonestrom, D.A., and K.C. Akstin. 1994. Nonmonotonc matric pressure histories during constant flux infiltration into homogeneous profiles. Water Resour. Res. 30(1): 81–91.

Wang, Z., J. Feyen, and E.D. Elrick. 1998. Prediction of fingering in porous media. Water Resour. Res. 34(9): 2183–2190.

Zhuang, L., S.M. Hassanizadeh, M.T. van Genuchten, A. Leijnse, A. Raoof, and C. Qin. 2016. Modeling of horizontal water redistribution in an unsaturated soil. Vadose Zone J. 15(3).

Chapter 6

Analysis of Dynamic Capillarity Effects in Modeling Saturation Overshoot during Infiltration

Prepared for submission to Transport in Porous Media, Zhuang, L., C.J. van Duijn, and S.M. Hassanizadeh.

Abstract

It is known that during downward infiltration of water into dry sand, fingers are formed. Moreover, the water saturation profile within each finger is non-monotonic, with a saturation overshoot at the finger tip. The Richards equation cannot simulate the occurrence of fingers and non-monotonic saturation behavior. In this work, we analyze an extended form of the Richards equation where dynamic capillarity effects are included. In this model, the pressure difference between two phases is related to the standard capillary pressure plus a term depending on the time rate of change of saturation. The coefficient of proportionality, denoted by τ, is called the dynamic capillarity coefficient. This coefficient controls the extent of saturation overshoot in a finger. Experimental and numerical studies have shown that the value of τ may depend on saturation. Based on reviews of numerical and experimental studies as well as mathematical analyses, we investigated four typical relationships between the coefficient τ and water saturation. We performed traveling wave calculations and compared numerical simulations with a recent water infiltration laboratory experiment. Different functional types were found to have a crucial impact on the saturation profiles.

6.1 Introduction

Traditionally, in two-phase flow systems, the difference between the non-wetting phase pressure and the wetting phase pressure, denoted as p^n-p^w, is assumed to be equivalent to the capillary pressure p^c. The relationship between capillary pressure (p^c) and water saturation (S^w) is fundamental for the characterization of unsaturated flow in porous media. This relationship is usually measured under static conditions and is commonly assumed to be independent of the fluid flow rate. However, it has been reported that the relation between p^n-p^w and S^w during dynamic processes differs from the equilibrium p^c-S^w relationship (e.g., Topp and Peters, 1967; Smiles et al., 1971; Vachaud et al., 1972; Elzeftawy and Mansell, 1975; Stauffer, 1978; Wildenschild et al., 2001; O'Carroll et al., 2005; Oung et al., 2005; Bottero et al., 2011; Weller et al., 2011). Stauffer (1978) proposed the use of a dynamic capillary pressure, in addition to the standard static capillary pressure. Through experimental studies, he found that the difference between the dynamic and static capillary pressures depends linearly on the temporal rate of change of saturation.

Following Hassanizadeh and Gray (1990) and Kalaydjian (1992), we choose a different conceptual approach. The approach assumes the presence of only one capillary pressure, notably the one that is measured under quasi-static conditions. What is measured under dynamic conditions is not capillary pressure but the difference between the two fluid pressures. Based on a thermodynamic approach, Hassanizadeh and Gray (1990) and Kalaydjian (1992) showed that the difference in fluid phase pressures under dynamic conditions is not just equal to the standard capillary pressure, but it includes a dynamic term, depending upon the temporal rate of saturation change. A linearized approximation may be written as (Hassanizadeh and Gray, 1993):

$$p^n - p^w - p^c = -\tau \frac{\partial S^w}{\partial t} \tag{6.1}$$

where p^n and p^w are non-wetting and wetting phase pressures, respectively, and where p^c is the capillary pressure. The approximation is defined as the difference between the non-wetting and wetting pressures under quasi-static condition. Furthermore, S^w in Equation (6.1) is the wetting phase saturation, and τ is non-equilibrium (or dynamic) capillarity coefficient. Recent studies have suggested that the dynamic coefficient τ varies with saturation (e.g., Dahle et al., 2005; Manthey et al., 2005; Camps-Roach et al., 2010; Joekar-Niasar et al., 2010; Goel and O'Carroll, 2011; Bottero et al., 2011). Comprehensive reviews on experimental and numerical research related to the effect

of dynamic capillarity are given in Hassanizadeh et al. (2002), Diamantopoulos and Durner (2011) and Joekar-Niasar and Hassanizadeh (2012).

A number of studies have quantified the value of the dynamic capillarity coefficient τ at different saturation values. However, the functional relationship between saturation and τ is still unclear. Different studies have produced different or even contradictory trends. In laboratory experiments with sand columns, Oung et al. (2005) and Bottero et al. (2011) found that the variation of τ with saturation was not significant. However, most numerical and experimental investigations have shown that τ generally decreases with increasing saturation. Rapid primary drainage experiments performed in PCE-water porous systems (Hassanizadeh et al., 2004; Bottero et al., 2006; Das and Mirzaei, 2012) and in air-water porous systems (Sakaki et al., 2010; Goel and O'Carroll, 2011) have shown that τ varies as a negative logarithmic function of saturation in the range $0.4<S^w<1$. Furthermore, O'Carroll (2005, 2010) determined the value of τ through inverse modeling of multistep outflow PCE-water experiments, and proposed a negative linear τ-S^w relationship. A similar decreasing τ-S^w relationship has been reported in various numerical studies based both on pore-scale (Dahle et al., 2005; Twan, 2007; Joekar-Niasar and Hassanizadeh, 2011) and continuum-scale (Manthey et al., 2005; Berentsen et al., 2006; Mirzaei and Das, 2007; Fučík et al., 2010) Simulations. A totally opposite trend was found by Camps-Roach et al. (2010) and Sakaki et al. (2010), who did primary drainage and main imbibition experiments, respectively. They reported that τ increases with increasing saturation.

Addition of the dynamic capillarity Equation (6.1) to the standard equations for two-phase flow (or unsaturated flow) leads to a totally different mathematical model. While standard equations are known to be unconditionally stable and give monotonic saturation profiles (Egorov et al., 2002), the dynamic capillarity model has shown to be conditionally unstable and may result in non-monotonic saturation profiles (van Duijn et al., 2004). There are only a few studies providing a mathematical analysis of the dynamic capillarity effect. Moreover, most of these studies have considered a constant value for τ (e.g., Cuesta and Hulshof, 2003; Cuesta et al., 2006; van Duijn et al., 2007, 2013a,b, 2015; Cuesta and Pop, 2009; Peszynska and Yi, 2008; Fan and Pop, 2013; Cao and Pop, 2016).

In this work, we analyze the effect of including the dynamic capillarity equation in the unsaturated flow model. We consider various forms of the relationships between τ and S^w, and provide traveling wave solutions of the full set of equations. Parameter values

for the model are based on a recent experimental study by Fritz (2012) of downward infiltration of water into a relatively dry one-dimensional sand column.

6.2 Description of experiments by Fritz (2012)

Gravity-driven fingering in unsaturated porous media has been observed experimentally and simulated numerically in many studies (e.g., Hill and Parlange, 1972; Glass et al., 1989, 1990; Baker and Hillel, 1990; Stonestrom and Akstin, 1994; Nieber et al., 2000; Eliassi and Glass, 2003; DiCarlo, 2004, 2007; Wang et al., 2004; Chapwanya and Stockie, 2010). Comprehensive reviews of theories, models and experiments have been carried out by DiCarlo (2013) and Xiong (2014).

Recently, well-defined one-dimensional water infiltration experiments in unsaturated sand have been performed by Fritz (2012). The experiments were designed to characterize saturation overshoot in a finger. A thin column with dimensions of 50 cm (height) by 1 cm (inner diameter) was employed. Clean coarse sand was packed into the column uniformly, while water was applied at the top of the vertical column. Saturation was measured at 20 cm from the inlet during all experiments. A series of experiments was conducted under different, but constant, water inflow rates and different, but constant, initial saturations. Results of the experiments with dry sand at three different inflow rates and a fixed initial saturation (S^w=0) are shown by means of the corresponding breakthrough curves in Figure 6.1a. As can be seen, saturation overshoot existed for all three inflow rates. The height of overshoot varied little, while the overshoot became wider with a decreasing inflow rate. Figure 6.1b presents saturation breakthrough curves obtained for three different initial saturations and a fixed inflow rate (4.3×10^{-5} m/s). As the value of initial saturation increased, the overshoot height decreased and even vanished for the largest initial saturation.

The aforementioned experiments have been simulated by Zhuang et al. (2016), employing different models of capillary hysteresis. In this work, we mainly focus on the mathematical analysis of the dynamic capillarity effect. We are not considering detailed simulation of experimental data. However, for the sake of choosing values for various physical quantities, we use for our analysis data of the experiment at and inflow rate of 4.3×10^{-5} m/s into dry sand. Measured quantities and characteristic parameters are listed in Table 6.1.

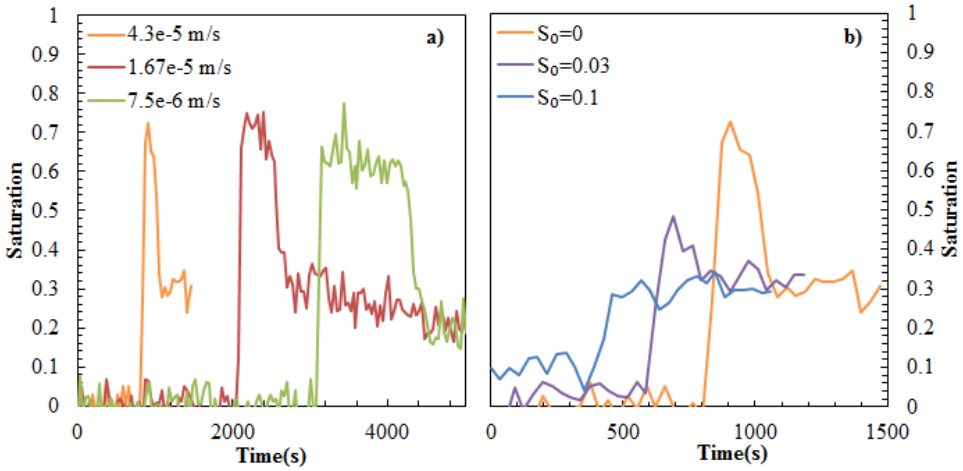

Figure 6.1 Measured saturation breakthrough curves at 20 cm, (a) in and initially dry soil with three different flow rates, and (b) at three different initial saturations at a flow rate of 4.3×10^{-5} m/s (Fritz, 2012).

Table 6.1 Experimental and reference values of parameters

Parameters	Unit	Value
Porosity, φ	-	0.4
Water density, ρ^w	kg m^{-3}	1×10^{3}
Water viscosity, μ^w	Pa·s	1×10^{-3}
Primary imbibition retention exponent, n	-	2.58
Primary imbibition retention parameter, α	Pa^{-1}	8.6×10^{-3}
Residual air saturation, S_r^a	-	0.05
Intrinsic permeability, k	m^2	6.43×10^{-10}
Inflow water flux, q_{in}	m s^{-1}	4.3×10^{-5}
Length of column, L	m	0.5

6.3 Governing equations

Consider a homogenously-packed sand with porosity φ and intrinsic permeability k. The continuity equation for the water phase is:

$$\varphi \frac{\partial S^w}{\partial t} + \frac{\partial}{\partial x}\left(-\frac{k^{rw}\left(S^w\right)k}{\mu^w}\left(\frac{\partial p^w}{\partial x} - \rho^w g\right)\right) = 0 \tag{6.2}$$

with

$$p^a - p^w = p^c\left(S^w\right) \tag{6.3}$$

Here p^a, S^w, $k^{rw}(S^w)$, p^w and ρ^w denote air pressure, water saturation, relative permeability, water pressure and water density, respectively, x is the vertical coordinate with positive direction pointing downwards, t is time, g is the gravitational constant and φ is porosity. In Equation (6.3), $p^c(S^w)$ is the capillary pressure, defined as the difference between air pressure and water pressure under equilibrium conditions. The van Genuchten-Mualem model (van Genuchten, 1980) was used for the relationships describing capillary pressure and relative permeability in terms of water saturation:

$$p^c\left(S^w\right) = \frac{1}{\alpha}\left[S_e^{-1/m} - 1\right]^{1/n} \tag{6.4}$$

$$k^{rw}\left(S^w\right) = S_e^{0.5}\left[1 - \left(1 - S_e^{1/m}\right)^m\right]^2 \tag{6.5}$$

$$S_e = \frac{S^w}{1 - S_r^a} = \frac{S^w}{S_{\mathrm{m}}} \tag{6.6}$$

where S_e, S_r^a and S_m=(1-S_r^a) denote effective water saturation, residual air saturation, and maximum water saturation, respectively; α and n are fitting parameters and m=1-1/n. We disregard any hysteresis in the capillary pressure and relative permeability. Hence, a single curve based on the capillary pressure-saturation relationship for primary imbibition was used.

When the dynamic capillarity effect is relevant, Equation (6.3) should be replaced by Equation (6.1). In an air-water system this becomes then:

$$p^a - p^w = p^c(S^w) - \tau(S^w)\frac{\partial S^w}{\partial t} \tag{6.7}$$

where $\tau(S^w)$ is the dynamic capillarity coefficient, which is a function of water saturation.

6.4 Initial and boundary conditions

The initial condition being considered here is a small and constant value of saturation, which we denote by S_B. The lower boundary of the domain is assumed to remain at this initial saturation. The upper boundary is an inflow boundary with a prescribed inflow rate, denoted by q_{in}. As a unit hydraulic head gradient is established at the inlet, soon after the inflow starts, we obtain $q_{in} \approx k^{rw}(S_T)k/\mu^w$. This means that one can calculate a saturation $S=S_T$ corresponding to q_{in}. This saturation remains constant as long as q_{in} does not change.

6.5 Dimensionless equations

A first step in the analysis is to make the equations dimensionless. For this purpose, characteristic reference values for length (x_R), time (t_R) and pressure (p_R) are introduced. With these values, we consider the dimensionless variables

$$\hat{t} = \frac{t}{t_R},\ \hat{x} = \frac{x}{x_R},\ u = \frac{p^a - p^w}{p_R} \text{ and } p^{c*}(S^w) = \frac{p^c(S^w)}{p_R}$$

where u denotes the dimensionless pressure difference.

The choice for x_R is the column length L and for p_R the factor $1/\alpha$ from Equation (6.4). For t_R we choose the transport time

$$t_R = \frac{\varphi L}{q_{in}} \tag{6.8}$$

The dimensionless forms of Equations (6.2) and (6.7) are then

$$\frac{\partial S^w}{\partial \hat{t}} + \frac{\partial}{\partial \hat{x}}\left[k^*(S^w)\left(\delta \frac{\partial u}{\partial \hat{x}} + 1 \right)\right] = 0 \tag{6.9}$$

$$u = p^{c*}(S^w) - \frac{\alpha q_{in}}{\varphi L}\tau(S^w)\frac{\partial S^w}{\partial \hat{t}} \tag{6.10}$$

where

$$\delta = \frac{1}{\alpha \rho^w g L} \text{ and } k^*(S^w) = \frac{k^{rw}(S^w)\ k\rho^w g}{\mu^w q_{in}}$$

Next, we eliminate the factor δ from Equation (6.9) by setting

$$x^* = \frac{\hat{x}}{\delta} \text{ and } t^* = \frac{\hat{t}}{\delta}$$

This gives the following dimensionless flow equations

$$\frac{\partial S^w}{\partial t^*}+\frac{\partial}{\partial x^*}\left[k^*(S^w)\left(\frac{\partial u}{\partial x^*}+1\right)\right]=0 \tag{6.11}$$

$$u=p^{c*}(S^w)-\tau^*(S^w)\frac{\partial S^w}{\partial t^*} \tag{6.12}$$

where $\tau^*\left(S^w\right)=\dfrac{\alpha^2\rho^w g q_{in}}{\varphi}\tau\left(S^w\right)$.

Suppressing all superscripts, except in p^c, yields the dimensionless form

$$\frac{\partial S}{\partial t}+\frac{\partial}{\partial x}\left[k(S)\left(\frac{\partial u}{\partial x}+1\right)\right]=0 \tag{6.13}$$

$$u=p^c(S)-\tau(S)\frac{\partial S}{\partial t} \tag{6.14}$$

Due to the dynamic term in Equation (6.14) (or in Equation (6.7)), the value of water saturation is not constrained. Large τ values may lead to large saturation overshoot. To prevent the non-physical behavior where $S_e>1$ (i.e. $S^w>S_m$), we need to extend the capillary pressure at $S_e=1$ in a way that allows for negative pressure values. Mathematically this can be achieved by considering a set-valued capillary pressure at $S_e=1$:

$$p^c(S)=\begin{cases}\left[S_e^{\,-1/m}-1\right]^{1/n} & for \quad S<S_m\\ (-\infty,0] & at \quad S=S_m\end{cases}$$

As we shall demonstrate later, this extension ensures that, no matter how large the capillarity coefficient $\tau(S)$, the resulting saturation cannot exceed $S=S_m$. In the numerical approach we replace the equation above by

$$p^c(S)=\begin{cases}\left[S_e^{\,-1/m}-1\right]^{1/n} & for \quad S\le S_m-\sigma\\ \dfrac{1}{\varepsilon}(S_m-\sigma-S)+p^c(S_m-\sigma) & for \quad S>S_m-\sigma\end{cases} \tag{6.15}$$

in which ε and σ are parameters that are chosen sufficiently small: $\varepsilon=1\times10^{-6}$ and $\sigma=1\times10^{-3}$. Furthermore

$$k(S)=\frac{k\rho^{w}g}{\mu^{w}q_{in}}S_e^{0.5}\left[1-\left(1-S_e^{1/m}\right)^{m}\right]^{2} \tag{6.16}$$

Table 6.2 Different expressions for dynamic capillarity coefficient τ (τ_0 is a constant)

Dynamic capillarity coefficient	Expressions
τ_1 (constant)	τ_0
$\tau_2(S)$ (decreasing)	$\tau_0(S_m\text{-}S)$
$\tau_3(S)$ (increasing)	$\tau_0 S$
$\tau_4(S)$ (increasing and non-integrable)	$\tau_0/(S_m\text{-}S)$

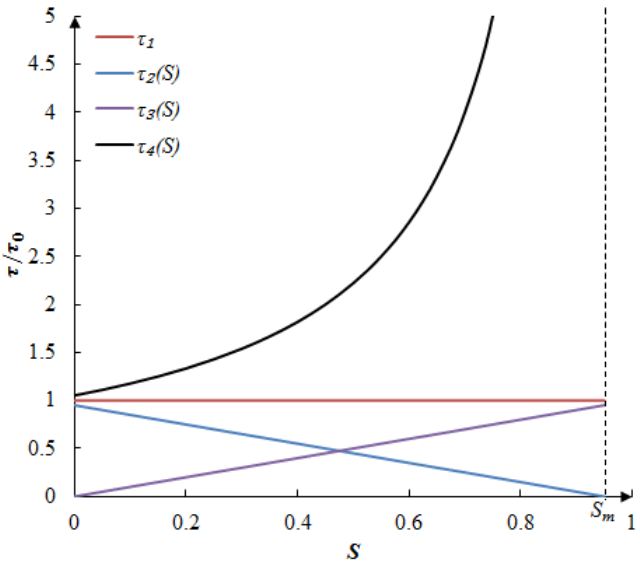

Figure 6.2 Plots of different expressions for dynamic capillarity coefficient τ

To complete the formulation of the problem, we need to specify how the dynamic capillarity coefficient τ depends on saturation. Based on experimental measurements reported in the literature, we consider four different τ-S relations, and investigate their impact on saturation behavior. The four relations are given in Table 6.2 and plotted in Figure 6.2. The first one is the constant case when $\tau_1= \tau_0$. In the second relation, $\tau_2(S)$ is a linearly decreasing function of saturation, which corresponds to the saturation dependence reported in many references cited above. The relations $\tau_3(S)$ and $\tau_4(S)$ are both increasing functions of saturation, but $\tau_4(S)$ is non-integrable at $S=S_m$. The last

two choices follow trends found in measurements by Camps-Roach et al. (2010) and Sakaki et al. (2010). Note that $\tau_2(S)$ and $\tau_3(S)$ are always smaller than τ_0, while $\tau_4(S)$ gives larger values (see Figure 6.2).

6.6 Traveling wave equations

In this section, we consider a special class of solutions of Equations (6.13) and (6.14) having the form of traveling waves. They describe the situation where saturation has reached a well-developed profile that moves through the column with a constant wave speed. Such situations generally arise after longer times, and are thus valid for relatively long domains. The waves connect an upstream saturation (here equal to the inflow saturation S_T) to a downstream saturation state (here equal to the initial saturation S_B), where $0<S_B<S_T<S_m$ (van Duijn et al., 2007). In mathematical terms, traveling waves are described by solutions having the form

$$S(x,t) = S(\eta) \text{ and } u(x,t) = u(\eta) \tag{6.17}$$

where $\eta=x-ct$. The unknowns are the saturation profile $S(\eta)$, the pressure profile $u(\eta)$ and the wave (or propagation) speed c. They are obtained from corresponding equations and boundary conditions. The boundary conditions for the traveling waves are attained at $\eta=\pm\infty$, and are given by

$$(S(-\infty), u(-\infty)) = (S_T, p^c(S_T)) \text{ and } (S(+\infty), u(+\infty)) = (S_B, p^c(S_B)) \tag{6.18}$$

Applying traveling wave form (6.17) to Equations (6.13) and (6.14), and using the chain rule of differentiation, one obtains the ordinary differential equations

$$-c\frac{dS}{d\eta} + \frac{d}{d\eta}\left[k(S)\left(\frac{du}{d\eta}+1\right)\right] = 0 \tag{6.19}$$

$$u = p^c(S) + \tau(S)c\frac{dS}{d\eta} \tag{6.20}$$

Equation (6.19) can be integrated to give

$$-cS + k(S)\left(\frac{du}{d\eta}+1\right) = C \tag{6.21}$$

where C is a constant of integration. We evaluate this equation at $\eta=\pm\infty$ and apply boundary conditions (6.18). Since the pressure difference u attains constant (but

different) values at $\eta=\pm\infty$, we must have $du/d\eta=0$ when $\eta=\pm\infty$. Using this in Equation (6.21) gives

$$\begin{cases} -cS_B + k(S_B) = C & (\eta = -\infty) \\ -cS_T + k(S_T) = C & (\eta = +\infty) \end{cases} \tag{6.22}$$

Solving these equations for c and C gives

$$c = \frac{k(S_T) - k(S_B)}{(S_T - S_B)} \tag{6.23}$$

$$C = \frac{k(S_B)S_T - k(S_T)S_B}{(S_T - S_B)} \tag{6.24}$$

Note that c is the well-known Rankine-Hugoniot speed. Substituting of Equations (6.23) and (6.24) into Equation (6.21), yields

$$\frac{du}{d\eta} = G(S) \tag{6.25}$$

where the function G is given by

$$G(S) = \frac{l(S)}{k(S)} - 1 \tag{6.26}$$

with

$$l(S) = \frac{k(S_B)(S_T - S) + k(S_T)(S - S_B)}{(S_T - S_B)} \tag{6.27}$$

The two functions $l(S)$ and $k(S)$ are plotted in Figure 6.3.

Also, Equation (6.20) can be rearranged to obtain

$$\frac{dS}{d\eta} = \frac{1}{\tau(S)c}\left[u - p^c(S)\right] \tag{6.28}$$

To find traveling wave solutions of the original system of Equations (6.13)-(6.16), one has to solve the coupled system given by Equations (6.25)-(6.28) subject to boundary conditions (6.18). A solution ($S(\eta)$, $u(\eta)$), with $-\infty<\eta<+\infty$, will be represented as a trajectory in the S-u plane. This trajectory connects the equilibrium point $E_T=(S_T, p^c(S_T))$, as $\eta\rightarrow-\infty$, to the equilibrium point $E_B=(S_B, p^c(S_B))$, as $\eta\rightarrow+\infty$.

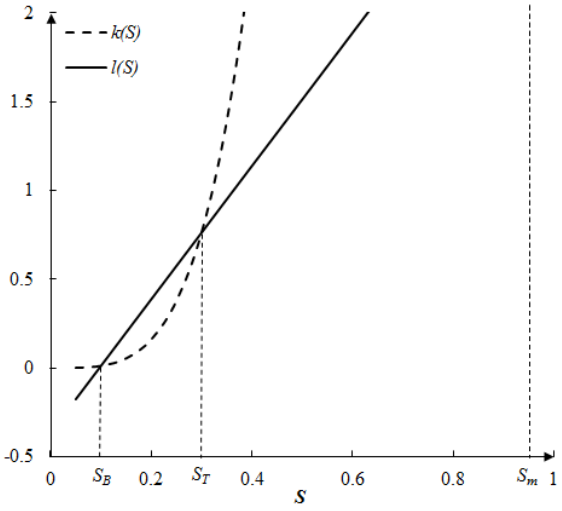

Figure 6.3 Plot of linear function $l(S)$ and relative permeability $k(S)$ as a function of saturation, for the case when S_B=0.1 and S_T=0.33.

For the construction of a trajectory (solution), it is important to know the nature of the equilibrium points. Linearizing the system at E_T and E_B, and computing the corresponding eigenvalues show that E_T is an unstable point and E_B is a saddle point. We will use this observation in the next section when computing the trajectory in the S-u plane.

6.7 Numerical results

The value of the downstream saturation S_B is specified as the initial saturation of the experiments. Instead of S_B=0, we took S_B=0.01 in the numerical simulations. The value of the water inflow rate q_{in} was transformed into the value of S_T as explained earlier. For q_{in} in Table 6.1, the corresponding value of the saturation is S_T=0.33.

We solved the traveling wave Equations (6.25)-(6.28) using MATLAB R2016a. Since the point E_B is a saddle, it is practically impossible to find the trajectory that reaches E_B, as $\eta \to +\infty$. For this reason we reversed the direction of the trajectories by setting $\xi = -\eta$, hence going from point E_B to point E_T. The direction of the trajectory leaving E_B is computed by taking the ratio of Equations (6.25) and (6.28) at S_B:

$$\left.\frac{du}{dS}\right|_{S=S_B} = \left.\frac{c\tau(S)G(S)}{p^c(S)-u}\right|_{S=S_B} = \frac{\left.\frac{d(c\tau(S)G(S))}{dS}\right|_{S=S_B}}{\left.\frac{dp^c(S)}{dS}\right|_{S=S_B} - \left.\frac{du}{dS}\right|_{S=S_B}} \tag{6.29}$$

The negative value was chosen since the difference between two phase pressures decreases as saturation increases from S_B to S_T. This gives a quadratic equation for $(du/dS)|_{S_B}$. A straightforward calculation gives a positive and negative root. We took $(du/dS)|_{S_B} < 0$ because the difference between the phase pressures decreases as the saturation increases.

Since E_B is an equilibrium point, one cannot start the computation at E_B. However, knowing the direction of the trajectory at E_B, we start the computations at a point very close to E_B in the proper direction, i.e. $S=S_B+\Delta S$ and $u = p^c\left(S_B\right) + (du/dS)|_{S=S_B}\,\Delta S$, with $\Delta S=10^{-3}$.

The focus of this chapter is on the influence of the dynamic capillarity coefficient $\tau(S)$ on saturation overshoot. In the next two sections, we show results of simulations based on experimental data for both the partial differential Equations (6.13)-(6.16) and the traveling wave Equations (6.25)-(6.28). We do this for the $\tau(S)$ relations listed in Table 6.2.

6.7.1 Numerical solutions of partial differential equations

In this section, we present numerical solutions of the dimensionless system (i.e., Equations. (6.13)-(6.16)), combined with the $\tau(S)$ relations in Table 6.2. The full set of equations was solved using the commercial software COMSOL Multiphysics 5.0. We used $\Delta x=10^{-2}$ and $\Delta t_{max}=10^{-3}$ to achieve mesh-independent solutions. The dimensionless distance and time were transformed to dimensional values to compare saturation breakthrough curves at 20 cm with the experimental data.

Results for best-fit values of τ_0 are shown in Figure 6.4. The experimental data are shown as symbols, while simulation results are presented as solid lines. The best fit was chosen to match the arrival time and shape of the overshoot as closely as possible. The black curve is for $\tau_0=0$; i.e. no dynamic effect was included. As expected, the resulting breakthrough curve is monotone, and there is no overshoot. The arrival time could be made to match the experimental arrival time only if the measured values of

porosity or inflow rate were adjusted. The red curve is for $\tau_1=\tau_0=1$. We see that neither the arrival time nor the overshoot height matched the experimental results. A decrease in τ_0 gave a lower overshoot, which was narrower and had an arrival time. An increase in τ_0 made the arrival time to become closer to the measurements and the overshoot wider (both are desirable), but the overshoot height became even larger. Hence $\tau_0=1$ provided the best compromise. Similarly, saturation curves for $\tau_2(S)$ and $\tau_4(S)$ showed higher overshoots with earlier arrival times as compared to the experimental results. For the integrable increasing function $\tau_3(S)$, we had to choose a much larger value of $\tau_0=35$ to obtain the correct arrival time right. But this led to a much wider overshoot.

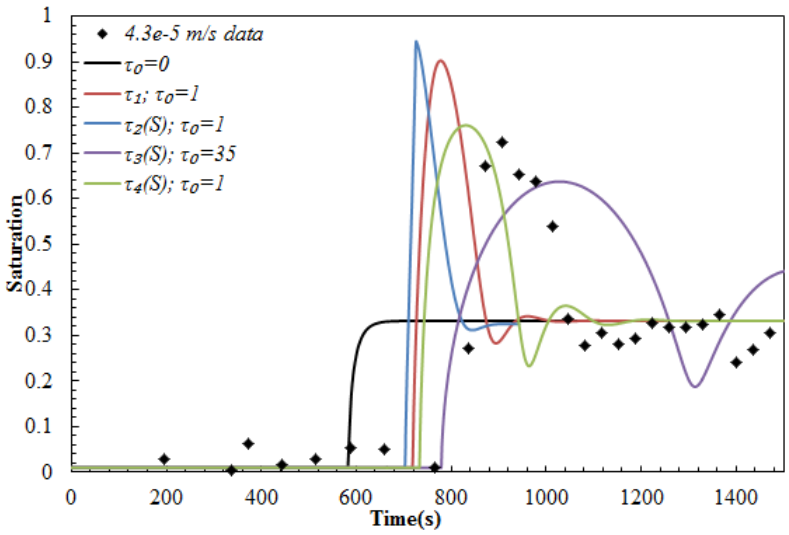

Figure 6.4 Saturation breakthrough curves at 20 cm from the inlet. Data are shown by symbols; results of simulations with different formulas for $\tau(S)$ are shown by solid lines. Values of τ_0 are normalized.

As explained earlier, we solve the travelling waves of Equations (6.25)-(6.28) by starting with an arbitrary η, say $\eta=0$, close to E_B in the proper direction. One is allowed to do so since any solution of Equations (6.25)-(6.28), subject to boundary conditions (6.18), can be shifted in η to obtain another solution: if $(S(\eta), u(\eta))$ is a solution, then so is $(S(\eta+a), u(\eta+a))$ for any $a \in R$. Therefore, we compared the S-u curves at $x=20$ cm obtained by solving Equations (6.13)-(6.16) with the traveling waves of Equations (6.25)-(6.28). Note that u is the normalized air-water pressure difference under dynamic conditions. The four plots are for the four expressions for $\tau(S)$, while the same values of τ_0 were used as those for the plots in Figure 6.4. The results are shown in Figure 6.5. In these figures, the dotted lines represent the p^c-S curve measured for

primary imbibition. Computed *S*-*u* curves at *x*=20 cm are shown in diamonds, while the travelling waves are shown as solid lines. As can be seen, the *S*-*u* curves at *x*=20 cm show qualitatively similar behavior as the traveling waves. Obviously, longer distance is needed for the *S*-*u* solutions to grow up to the traveling wave solutions, which are in principle valid for a semi-infinite domain.

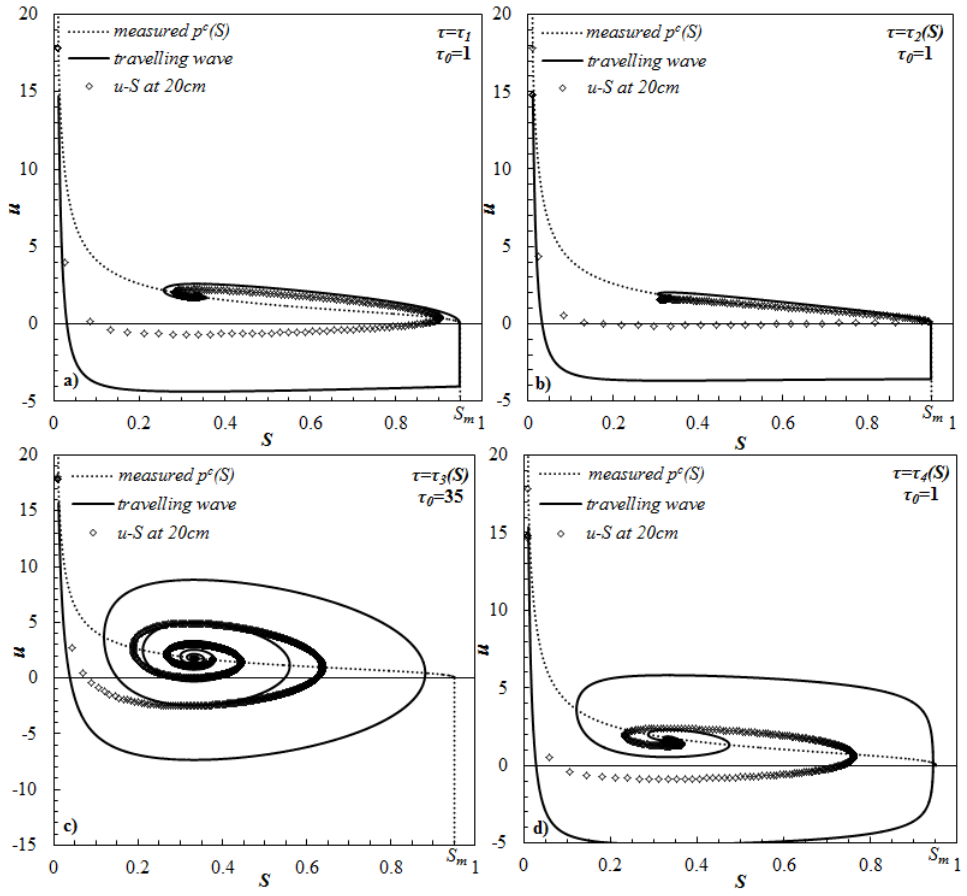

Figure 6.5 Plots of air-water pressure difference vs saturation for different τ expressions under dynamic conditions, obtained from numerical solutions of Equations (6.13)-(6.16) at *x*=20 cm (diamonds) and from numerical solutions of the traveling waves, Equations (6.25)-(6.28) (solid lines)

6.7.2 Mathematical traveling wave analysis

As shown above, traveling wave solutions can give qualitative trends in the pressure-saturation relationship. In this section we first summarize some recent mathematical

results of traveling analyses obtained by van Duijn et al. (2016). Then, we present results of computations for a series of sensitivity analyses of the traveling wave solution. As mentioned before, we shall discuss the behavior of solutions of Equations (6.25)-(6.28) in terms of the behavior of corresponding trajectories in the *S*-*u* plane. These trajectories connect the point $E_T=(S_T,\ p^c(S_T))$ as $\eta\rightarrow-\infty$ to the point $E_B=(S_B,\ p^c(S_B))$ as $\eta\rightarrow+\infty$.

First, we consider the case where $\tau(S)$ is constant, i.e. let $\tau_1=\tau_0$. Clearly, the strength of the overshoot is determined by the value of τ_0. In fact, for small values of τ_0, there is no overshoot at all. Cuesta et al. (2000) and van Duijn et al. (2007) have shown that a critical value τ_c exists such that if the dynamic capillarity coefficient $\tau_0>\tau_c$, trajectories go infinitely many times around the point E_T as they approach that point, thus implying a saturation overshoot and damped oscillations in the *S*-*u* profiles as $\eta\rightarrow-\infty$. When $0<\tau_0\leq\tau_c$, trajectories can go around the point E_T at most a finite number of times and probably in that case the trajectory approaches the point E_T in a direct and monotone way. This critical value is given by

$$\tau_c=-\frac{[p^{c\prime}(S_T)]^2}{4cG'(S_T)} \tag{6.30}$$

where $p^c(S)$ and $G(S)$ are given by Equations (6.15) and (6.26), respectively, and c is the wave speed (Equation (6.23)). Here the prime sign denotes differentiation with respect to *S*.

For all values of $\tau_0>0$, the trajectories approach the point E_B, as $\eta\rightarrow+\infty$, in a direct and monotone way. This means that the *S*-*u* profiles are monotone (i.e., *S* decreases and the pressure difference *u* increases) as $\eta\rightarrow+\infty$.

A summary of results related to the effect of τ for different values of S_T and S_B is given in Appendix E. The case where the capillarity coefficient depends on saturation is discussed in Appendix F.

6.7.3 Numerical solutions of the traveling wave equations

The influence of different inflow rates

In this section we consider the dynamic capillarity coefficient $\tau(S)=\tau_0$ (a constant). As explained in Appendix E, the critical value S_{T0} could be calculated as 0.087. Based on the value of S_{T0}, two different values of S_T, i.e. 0.08 (smaller than S_{T0}) and 0.15 (larger

than S_{T0}), were assigned in the calculations to investigate the effects of different inflow rates.

As explained earlier, the travelling waves of Equations (6.25)-(6.28) were solved. The resulting *S*-*u* trajectories are shown in Figure 6.6. The measured primary imbibition curve is shown as a dotted line, while the solid and dashed lines with different colors represent *S*-*u* curves under different dynamic conditions: i.e. for different values of τ_0. As shown in both Figures 6.6a and 6.6b, saturation overshoot always became higher as the value of τ_0 increased. When S_T=0.08 ($S_T < S_{T0}$), the *S*-*u* curve only exhibited a very small saturation overshoot, even with a relatively large value of τ_0=500 (corresponding to a dimensional value at 5×10^6 Pa·s; see Figure 6.6a). When S_T=0.15 ($S_T > S_{T0}$), the *S*-*u* curve showed a distinct saturation overshoot followed by smaller saturation oscillations for τ_0=100 (see Figure 6.6b). For S_T=0.15, the maximum value of the saturation S_β (see Appendix E) was larger than S_m, so the *S*-*u* curve could reach the extension of $p^c(S)$ (Equation (6.15)) for large values of τ_0.

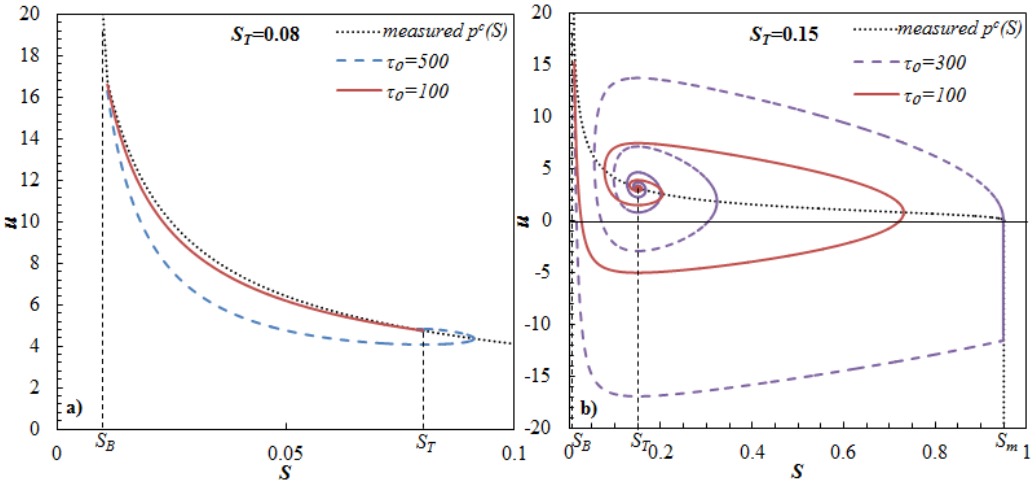

Figure 6.6 Saturation-pressure difference curves for different dynamic conditions (values of τ_0) and different values of S_T: a) $S_B<S_T<S_{T0}$ and b) $S_B<S_{T0}<S_T$. Here S_{T0} is defined in Appendix E.

Comparing corresponding *S*-*u* curves (τ_0=100) for different values of S_T, increasing the value of S_T (or the value of inflow rate) caused a dramatic increase in saturation overshoot. A similar trend was found in the experiments of DiCarlo (2004). The value of S_{T0}=0.0875 (corresponding a dimensional value of inflow rate, 3×10^{-7} m/s) is a critical value; distinct saturation overshoot will occur only if the inflow rate is larger than that value. The smallest inflow rate in the experiments of Fritz (2012) (see Figure

6.1a) was 7.5×10^{-6} m/s, which is around twenty times larger than the critical value. Such a large inflow rate results in a very large saturation overshoot, which was observed in the experiments of Fritz (2012).

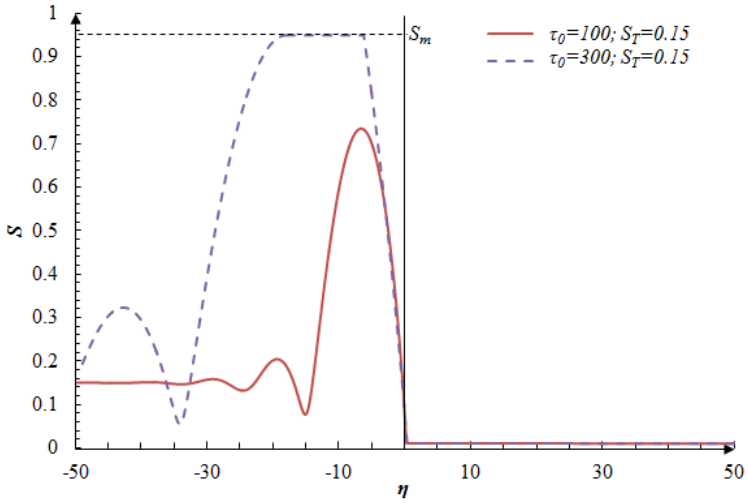

Figure 6.7 Saturation vs moving coordinate η for different dynamic conditions (values of τ_0), but with fixed S_T=0.15. Here we shifted η such that $S(0)=1/2(S_T+ S_B)$.

Figure 6.7 shows corresponding saturation values as a function of the moving coordinate η for S_T=0.15 (also shown in Figure 6.6b). One observes a distinct saturation overshoot followed by smaller oscillations when going from S_B to S_T. When saturation reached the maximum value S_m, the overshoot exhibits a plateau.

The influence of different expressions for $\tau(S)$

Here we consider an inflow rate of 4.3×10^{-5}m/s, which corresponds to a S_T value of 0.33. As explained in Appendix F (see Equation (F11), the critical value τ_c now depends on the actual form of $\tau(S)$. Corresponding to the expressions in Table 6.2, we have the values of τ_c listed in Table 6.3, for fixed S_T=0.33. Different formulas shown in Table 6.2 were assigned to the dynamic capillarity coefficient τ, and the results are shown in Figure 6.8. The inset shows an enlargement of the curves near S_T.

Table 6.3 Values of τ_c for different expressions of the dynamic capillarity coefficient

Dynamic capillarity coefficient	**τ_c for S_T=0.33**
τ_1 (constant)	0.14
$\tau_2(S)$ (decreasing)	0.23
$\tau_3(S)$ (increasing)	0.42
$\tau_4(S)$ (increasing and non-integrable)	0.09

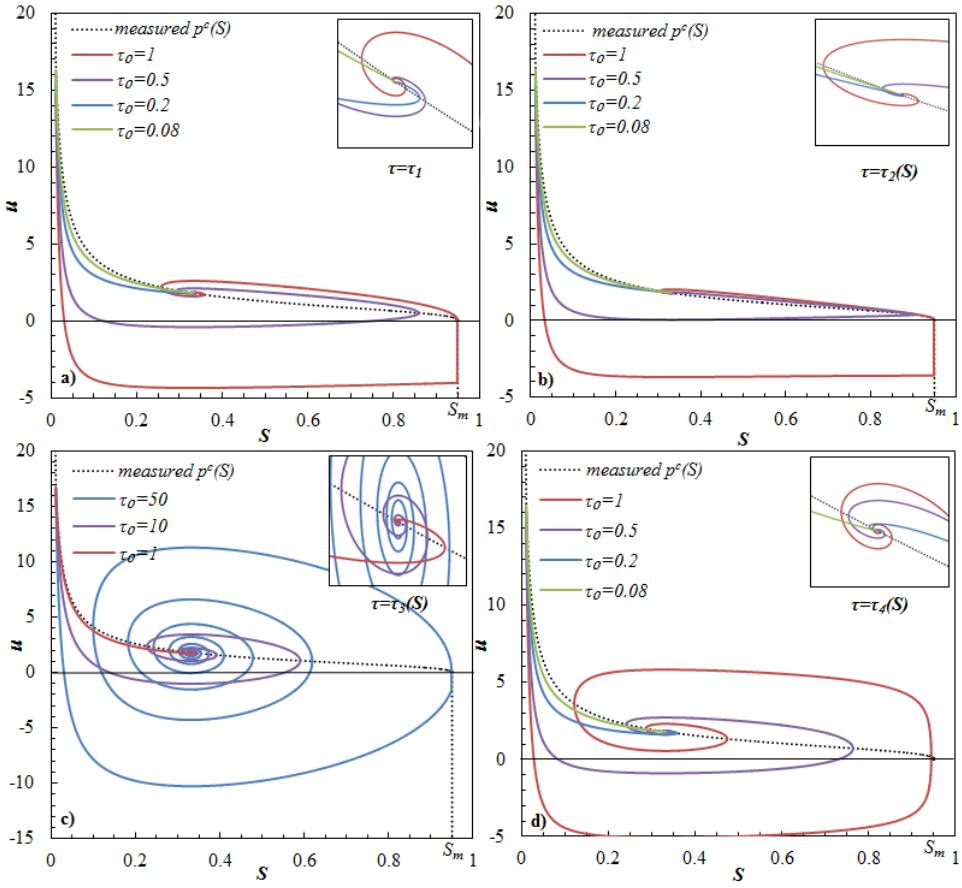

Figure 6.8 Saturation-pressure difference curves for different forms of $\tau(S)$: a) constant τ_1, b) decreasing $\tau_2(S)$, c) increasing $\tau_3(S)$, and d) non-integrable increasing $\tau_4(S)$

The computations were carried out for different values of τ_0, in each formula. Values τ_0=0.08 (which is less than τ_c) and 0.2, 0.5 and 1 (which are larger than τ_c) were chosen

for τ_1, $\tau_2(S)$ and $\tau_4(S)$. But for $\tau_3(S)$, we took τ_0 values of 1, 10 and 50 to show distinctly different saturation overshoot behaviors. Results obtained for a constant τ_0 are shown in Figure 6.8a. Note that the solution is monotonic when $\tau_0<\tau_c$. But, for $\tau_0>\tau_c$, a saturation overshoot exists (being larger for larger τ_0 values) along with small saturation oscillations. For the largest value τ_0=1, the maximum saturation of S_m is reached and the solution follows the extension of the capillary pressure (Equation (6.15)). Corresponding to the decreasing $\tau_2(S)$ and increasing integrable $\tau_3(S)$, saturation reached S_m for larger τ_0 values (see Figures 6.8b and 6.8c). However, the saturation obtained with the non-integrable increasing $\tau_4(S)$ had the smooth saturation plateau when saturation was close to S_m, with saturation always remaining just below S_m.

As shown in Figure 6.2, $\tau_2(S)<\tau_1<\tau_4(S)$ for $0<S<S_m$. However, the saturation overshoot corresponding to the largest $\tau_4(S)$ was lower than the one corresponding to the smallest function $\tau_2(S)$ (see τ_0=0.5 in Figures 6.8a, 6.8b and 6.8d). This trend is opposite as for the solutions for a constant τ_1, where larger saturation overshoot occurs for larger τ_0 values. This is explained in Appendix F.

6.8 Summary and conclusions

In this chapter we gave an overview of the literature describing the relationship between the dynamic capillarity coefficient τ and the saturation. Based on that overview, we considered four different expressions to specify the dependence of τ on saturation: constant τ_1, decreasing $\tau_2(S)$, increasing $\tau_3(S)$ and non-integrable increasing $\tau_4(S)$. We analyzed their effect on solutions of the unsaturated flow model for downward infiltration of water.

We provided a traveling wave analysis of the full equations using parameter values of a recent water infiltration experiment (Fritz, 2012). Saturation was found to be very sensitive to the value of the inflow rate. A relatively large saturation overshoot was found when the inflow rate was larger than 3×10^{-7} m/s. This is in agreement with the large overshoots observed in the experiments of Fritz (2012).

Based on traveling wave computations and simulation results for the full set of equations, the solution obtained with the non-integrable increasing $\tau_4(S)$ gave a saturation overshoot similar to the one found experimentally, but with a significant earlier arrival time. The traveling wave solution described the infiltration experiment only for longer distances when the saturation-pressure profiles were fully developed.

Nevertheless, they provided the same trend as obtained with simulations of the full equations.

In this chapter we disregarded hysteresis in the capillary pressure and the relative permeability: only the primary imbibition curves for capillary pressure and relative permeability were used. In a full analysis of the experiments, one has to include hysteretic effects as well. Here the emphasis was on understanding the influence and effect of the dynamic capillarity coefficient.

6.9 Appendix E

The effect of the dynamic term becomes larger, and consequently the overshoot becomes higher, for larger values of τ_0. Depending upon the values of S_B and S_T, it may happen that saturation reaches the maximum value S_m. That is why we extended the capillary pressure for $S > S_m$ in Equation (6.15).

Let us define the following function

$$\beta(S_T, S_B) = \int_{S_B}^{S_m} G(S; S_T, S_B)\, dS \qquad \text{(E1)}$$

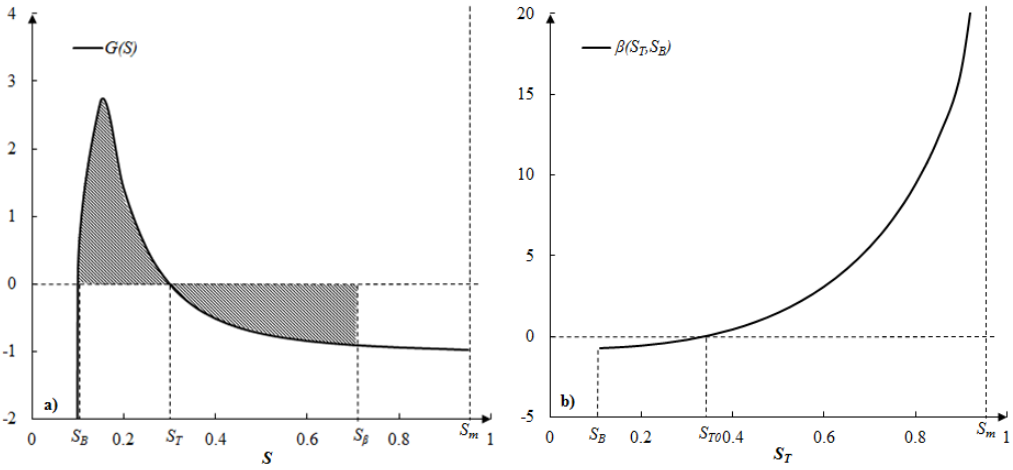

Figure 6.9 Left: the function $G(S)$ for a given $S_B<S_T<S_m$; Right: the integral $\beta(S_T,S_B)$ for a given S_B and with S_T ranging from S_B to S_m, for the case when $S_B=0.1$ and $S_T=0.33$.

The properties of G imply that $\beta(S_T,S_B)<0$ for S_T close to S_B and $\beta(S_T,S_B)>0$ for S_T close to S_m. Furthermore, $\beta(S_T,S_B)$ increases when S_T increases. Hence, a unique saturation S_{T0} exists when $\beta(S_T,S_B)=0$ (see Figure 6.9b). If S_T and S_B are such that

$\beta(S_T,S_B)<0$, i.e. $S_T<S_{T0}$, then for all $\tau_0>0$, no matter how large, the saturation overshoot remains bounded away from the maximum value S_m. More precisely, if $S_T<S_{T0}$, then $S(\eta)<S_\beta<S_m$, when S_β is determined such that (see Figure 6.9a)

$$\int_{S_B}^{S_\beta} G(S;S_T,S_B)dS = 0 \tag{E2}$$

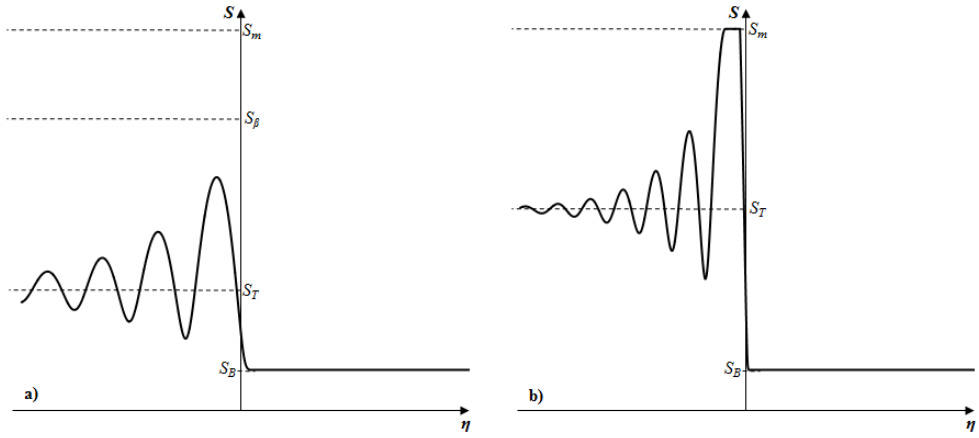

Figure 6.10 Sketch of saturation profiles: a) $\beta(S_T,S_B)<0$ and $S(\eta)<S_\beta<S_m$, no matter how large $\tau_0>0$; b) $\beta(S_T,S_B)>0$ in which case a saturation overshoot exists with a plateau at $S=S_m$ when τ_0 is sufficiently large (i.e. $\tau_0>\tau_{max}$)

On the other hand, if S_T and S_B are such that $\beta(S_T,S_B)>0$, i.e. $S_T>S_{T0}$ (see Figure 6.9b), then a $\tau_{max}>\tau_c$ exists such that

i) If $\tau_0<\tau_{max}$, then the corresponding saturation satisfies $S(\eta)<S_m$. This implies that the overshoot does not reach the maximal value S_m.

ii) If $\tau_0>\tau_{max}$, then the corresponding saturation has an overshoot with a plateau at the maximal value S_m.

Thus we have saturation profiles as sketched in Figure 6.10.

6.10 Appendix F

Here we discuss the case where $\tau(S)$ is not constant, but varies with saturation. For convenience we write

$$\tau(S) = \tau_0 f(S) \tag{F1}$$

First, consider the case where f is integrable, i.e.

$$\int_0^{S_m} \tau(S)dS < \infty \tag{F2}$$

Example: Let $f(S)=(S_m-S)^{\omega}$ for $0<S<S_m$ with $-\infty<\omega<+\infty$. Then

$$\int_0^{S_m} f(S)dS = \begin{cases} 1/1+\omega \, S_m^{1+\omega} < \infty & if\ \omega > -1 \\ +\infty & if\ \omega \le -1 \end{cases}$$

The function f is integrable if $\omega>-1$ (although $f(S)$ has singular behavior as $S\rightarrow S_m$ if $-1<\omega<0$) and f is non-integrable if $\omega\leq -1$.

When Equation (F2) holds, it is possible to transform the system of Equations (6.25)-(6.28) to a new system that is similar to the case of constant τ. To see this we introduce

$$y = F(S) = \int_0^S f(z)dz \tag{F3}$$

as a new variable and rewrite Equations (6.25)-(6.28) in terms of y and u.

Since $f(S)>0$ for $0<S<S_m$, the function F is strictly increasing in S. One can therefore also express S as a function of y,

$$S = \varphi(y) \tag{F4}$$

where φ is the inverse of F.

Now setting

$$p^c(S) = p^c(\varphi(y)) = \hat{p}^c(y) \text{ and } G(S) = G(\varphi(y)) = \hat{G}(y) \tag{F5}$$

and using

$$\tau(S)\frac{dS}{d\eta} = \tau_0 f(S)\frac{dS}{d\eta} = \tau_0 \frac{dy}{d\eta} \tag{F6}$$

one obtains the system of equations in terms of y and u

$$\frac{du}{d\eta} = \hat{G}(y) \tag{F7}$$

$$\frac{dy}{d\eta} = \frac{1}{\tau_0 c}(u - \hat{p}^c(y)) \tag{F8}$$

This transformed system is qualitatively of the same nature as the original system Equations (6.25)-(6.28) with $\tau(S)= \tau_0$. Therefore we can make the same analysis as before for $\tau_1= \tau_0$. We redefine Equations (E1) and (E2) according to

$$\beta(S_T, S_B) = \int_{F(S_B)}^{F(S_m)} \hat{G}(y; y_T, y_B)dy = \int_{S_B}^{1-S_r^a} G(S; S_T, S_B) f(S)dS \tag{F9}$$

$$\int_{F(S_B)}^{F(S_\beta)} \hat{G}(y)dy = \int_{S_B}^{S_\beta} G(S) f(S)dS = 0 \tag{F10}$$

With $y_T=F(S_T)$, the expression for the critical value τ_c becomes (see also Equation (6.30))

$$\tau_c = \frac{[\hat{p}^{c'}(y_T)]^2}{4c\hat{G}'(y_T)} = \frac{[p^{c'}(S_T)]^2}{4cf(S_T)G'(S_T)} \tag{F11}$$

Finally, we consider the case where $\tau(S)$ has such strong singularity at $S=S_m$ so that

$$\int_0^{S_m} \tau(S)dS = \infty \tag{F12}$$

One can then show that for every $\tau_0>0$ in Equation (F1), the saturation overshoot always remains below the maximal value S_m. In essence this follows from transformation Equations (F3) and (F4), where now $0<y<F(S_m)=\infty$. This shows that the transformed system (Equations (E7) and (E8)) always has a solution with $y<\infty$, implying $S<S_m$.

Acknowledgement

This work was carried out in collaborations with the Darcy Center of Utrecht University. The first author was supported by China Scholarship Council (No. 201206380076). The third author received funding from the European Research Council under the European Union's Seventh Framework Program (FP/2007-2013)/ERC Grant Agreement No. 341225.

References

Baker, R.S., and D. Hillel. 1990. Laboratory tests of a theory of fingering during

infiltration into layered soils. Soil Sci. Soc. Am. J. 54(1): 20–30.

Berentsen, C.W., S.M. Hassanizadeh, A. Bezuijen, and O. Oung. 2006. Modelling of two-phase flow in porous media including non-equilibrium capillary pressure effects. *In* Proceeding of the XVI International Conference on Computational methods in Water Resources. Tech. Univ. of Denmark, Copenhagen, Denmark.

Bottero, S., S.M. Hassanizadeh, P.J. Kleingeld, and A. Bezuijen. 2006. Experimental study of dynamic capillary pressure effect in two-phase flow in porous media. *In* Proceedings of the XVI International Conference on Computational methods in Water Resources. Tech. Univ. of Denmark, Copenhagen, Denmark.

Bottero, S., S.M. Hassanizadeh, P.J. Kleingeld, and T.J. Heimovaara. 2011. Nonequilibrium capillarity effects in two-phase flow through porous media at different scales. Water Resour. Res. 47: W10505.

Camps-Roach, G., D.M. O'Carroll, N.T. A., and S. Toshihiro. 2010. Experimental investigation of dynamic effects in capillary pressure: Grain size dependency and upscaling. Water Resour. Res. 44: W08544.

Cao, X., and I.S. Pop. 2016. Degenerate two-phase porous media flow model with dynamic capillarity. J. Differ. Equ. 260(3): 2418–2456.

Chapwanya, M., and J.M. Stockie. 2010. Numerical simulations of gravity-driven fingering in unsaturated porous media using a nonequilibrium model. Water Resour. Res. 46: W09534.

COMSOL. 2014. COMSOL Multiphysics 5.0. COMSOL Inc., Burlington, MA.

Cuesta, C.M., C.J. van Duijn, and J. Hulshof. 2000. Infiltration in porous media with dynamic capillary pressure: travelling waves. Eur. J. Appl. Math 11(4): 381-397.

Cuesta, C.M., C.J. van Duijn, and I.S. Pop. 2006. Non-classical shocks for Buckley-Leverett: Degenerate pseudo-parabolic regularisation. Progress in Industrial Mathematics at ECMI 2004. Springer Berlin Heidelberg, 2006: 569-573.

Cuesta, C.M., and J. Hulshof. 2003. A model problem for groundwater flow with dynamic capillary pressure : stability of travelling waves. Nonlinear Anal.: Theory Methods Appl. 52 (4): 1199–1218.

Cuesta, C.M., and I.S. Pop. 2009. Numerical schemes for a pseudo-parabolic Burgers equation: discontinuous data and long-time behaviour. J. Comput. Appl. Math 224(1): 269-283.

Dahle, H.K., M.A. Celia, and S.M. Hassanizadeh. 2005. Bundle-of-tubes model for calculating dynamic effects in the capillary-pressure-saturation relationship. Transp. Porous Media 58(1): 5–22.

Das, D.B., and M. Mirzaei. 2012. Dynamic effects in capillary pressure relationships for two-phase flow in porous media: experiments and numerical analyses. AIChE J. 58(12): 3891–3903.

Diamantopoulos, E. and W. Durner. 2011. Dynamic nonequilibrium of water flow in porous media: a review. Vadose Zone J. 11(3).

DiCarlo, D.A. 2004. Experimental measurements of saturation overshoot on infiltration. Water Resour. Res. 40(4): W04215.

DiCarlo, D.A. 2007. Capillary pressure overshoot as a function of imbibition flux and

initial water content. Water Resour. Res. 43: W08402.

DiCarlo, D.A. 2013. Stability of gravity-driven multiphase flow in porous media: 40 Years of advancements. Water Resour. Res. 49(8): 4531–4544.

van Duijn, C.J., Y. Fan, L.A. Peletier, and I.S. Pop. 2013a. Travelling wave solutions for degenerate pseudo-parabolic equations modelling two-phase flow in porous media. Nonlinear Anal. Real World Appl. 14(3): 1361–1383.

van Duijn, C.J., S.M. Hassanizadeh, I.S. Pop, and P.A. Zegeling. 2013b. Non-equilibrium Models for Two Phase Flow in Porous Media : the Occurrence of Saturation Overshoots. p. 59–70. *In* 5th International Conference on Applications of Porous Media. Romania.

van Duijn, C.J., L.A. Peletier, and I.S. Pop. 2007. A new class of entropy solutions of the Buckley–Leverett equation. SIAM J. Math. Anal. 39(2): 507–536.

van Duijn, C.J., G.J.M. Pieters, and P.A.C. Raats. 2004. Steady flows in unsaturated soils are stable. Transp. Porous Media 57(2): 215-244.

van Duijn, C.J., X. Cao, and I.S. Pop. 2015. Two-phase flow in porous media: dynamic capillarity and heterogeneous media. Transp. Porous Media: 1-26.

Egorov, A.G., R.Z. Dautov, J.L. Nieber, and A.Y. Sheshukov. 2002. Stability analysis of traveling wave solution for gravity-driven flow, Dev. Water Sci., 47(C), 121–128.

Eliassi, M., and R.J. Glass. 2003. On the porous continuum-scale modeling of gravity-driven fingers in unsaturated materials: Numerical solution of a hypodiffusive governing equation that incorporates a hold-back-pile-up effect. Water Resour. Res. 39(6): 1167.

Elzeftawy, A., and R.S. Mansell. 1975. Hydraulic conductivity calculations for unsaturated steady-state and transient-state flow in sand. p. 599–603. *In* Soil Science Society of America Journal.

Fan, Y, and I.S. Pop. 2013. Equivalent formulations and numerical schemes for a class of pseudo-parabolic equations, J. Comput. Appl. Math., 246: 86-93.

Fritz, S. 2012. Experimental investigations of water infiltration into unsaturated Soil - analysis of dynamic capillarity effects, M.S. thesis, Stuttgart University, Germany. http://www.nupus.uni-stuttgart.de/07_Preprints_Publications/Preprints/Preprints-PDFs/Preprint_2012-7.pdf.

Fučík, R., J. Mikyška, S. Toshihiro, M. Beneš, and T.H. Illangasekare. 2010. Significance of dynamic effect in capillarity during drainage experiments in layered porous media. Vadose Zone J. 9(3): 697–708.

Glass, R.J., S. Cann, J. King, N. Baily, J.-Y. Parlange, and T.S. Steenhuis. 1990. Wetting front instability in unsaturated porous media: A three-dimensional study in initially dry Sand. Transp. Porous Media 5(3): 247–268.

Glass, R.J., T.S. Steenhuis, and J.-Y. Parlange. 1989. Wetting front instability 2. Experimental determination of relationships between system behavior in initially dry porous media. Water Resour. Res. 25(6): 1195–1207.

Goel, G., and D.M. O'Carroll. 2011. Experimental investigation of nonequilibrium capillarity effects: Fluid viscosity effects. Water Resour. Res. 47(9): 1–15.

Hassanizadeh, S.M., M.A. Celia, and H.K. Dahle. 2002. Dynamic effect in the capillary

pressure-saturation relationship and its impacts on unsaturated flow. Vadose Zone J. 1(1): 38–57.

Hassanizadeh, S.M., and W.G. Gray. 1990. Mechanics and thermodynamics of multiphase flow in porous media including interphase boundaries. Adv. Water Resour. 13(4): 169–186.

Hassanizadeh, S.M., and W. G. Gray (1993), Thermodynamic basis of capillary pressure in porous media, Water Resour. Res., 29(10), 3389–3405.

Hassanizadeh, S.M., O. Oung, and S. Manthey. 2004. Laboratory experiments and simulations on the significance of non-equilibrium effect in the capillary pressure-saturation relationship. p. 3–14. *In* Unsaturated Soil: Experimental Studies: Proceedings of the International Conference: From experimental evidence towards numerical modeling of unsaturated soils. Weimar, Germany.

Hill, D.E., and J.-Y. Parlange. 1972. Wetting Front Instability in Layered Soils. Soil Sci. Soc. Am. J. 36(October): 697–702.

Joekar-Niasar, V., and S.M. Hassanizadeh. 2012. Analysis of Fundamentals of Two-Phase Flow in Porous Media Using Dynamic Pore-Network Models: A Review. Crit. Rev. Environ. Sci. Technol. 42(18): 1895–1976.

Joekar-Niasar, V., S.M. Hassanizadeh, and H.K. Dahle. 2010. Non-equilibrium effects in capillarity and interfacial area in two-phase flow: dynamic pore-network modelling. J. Fluid Mech. 655: 38–71.

Joekar-Niasar, V., and S.M. Hassanizadeh. 2011. Effect of fluids properties on non-equilibrium capillarity effects: Dynamic pore-network modeling. Int. J. Multiph. Flow 37(2): 198–214.

Kalaydjian, F.-M. 1992. Dynamic capillary pressure curve for water/oil displacement in porous media: Theory vs. experiment. *In* SPE Annual Technical Conference and Exhibition. Society of Petroleum Engineers.

Manthey, S., S.M. Hassanizadeh, and R. Helmig. 2005. Macro-scale dynamic effects in homogeneous and heterogeneous porous media. Transp. Porous Media 58(1-2): 121–145.

MATLAB. 2016. MATLAB R2016a. The Math Works Inc., MA.

Mirzaei, M., and D.B. Das. 2007. Dynamic effects in capillary pressure-saturations relationships for two-phase flow in 3D porous media: Implications of micro-heterogeneities. Chem. Eng. Sci. 62(7): 1927–1947.

Nieber, J., T.W. Bauters, T. Steenhuis, and J.-Y. Parlange. 2000. Numerical simulation of experimental gravity-driven unstable flow in water repellent sand. J. Hydrol. 231-232: 295–307.

O'Carroll, D.M., K.G. Mumford, L.M. Abriola, and J.I. Gerhard. 2010. Influence of wettability variations on dynamic effects in capillary pressure. Water Resour. Res. 46(8): 1–13.

O'Carroll, D.M., T.J. Phelan, and L.M. Abriola. 2005. Exploring dynamic effects in capillary pressure in multistep outflow experiments. Water Resour. Res. 41(11): 1–14.

Oung, O., S.M. Hassanizadeh, and A. Bezuijen. 2005. Two-phase flow experiments in a

geocentrifuge and the significance of dynamic capillary pressure effect. J. Porous Media 8(3): 247–257.

Peszynska, M., and S. Yi. 2008. Numerical methods for unsaturated flow with dynamic capillary pressure in heterogeneous porous media. Int. J. Numer. Anal. Model. 5: 126–149.

Sakaki, T., D.M. O'Carroll, and T.H. Illangasekare. 2010. Direct Quantification of Dynamic Effects in Capillary Pressure for Drainage–Wetting Cycles. Vadose Zone J. 9(2): 424–437.

Smiles, D.E., G. Vachaud, and M. Vauclin. 1971. A test of the uniqueness of the soil moisture characteristic during transient, nonhysteretic flow of water in a rigid soil1. Soil Sci. Soc. Am. J. 35(4): 534–539.

Stauffer, F. 1978. Time dependence of the relations between capillary pressure, water content and conductivity during drainage of porous media. p. 29 Aug–1 Sept. *In* IAHR symposium on scale effects in porous media, Thessaloniki, Greece. Thessaloniki, Greece.

Stonestrom, D.A., and K.C. Akstin. 1994. Nonmonotonc matric pressure histories during constant flux infiltration into homogeneous profiles. Water Resour. Res. 30(1): 81–91.

Topp, G., and A. Peters. 1967. Comparison of water content-pressure head data obtained by equilibrium, steady-state, and unsteady-state methods1. Soil Sci. Soc. Am. J. 31(3): 312–314.

Twan, G. 2007. Dynamic effect in two-phase flow in porous media: a pore-scale network approach, Ph.D. thesis, Delft University of Technology, the Netherlands.

Vachaud, G., M. Vauclin, and M. Wakil. 1972. A study of the uniqueness of the soil moisture characteristic during desorption by vertical drainage. Soil Sci. Soc. Am. J. 36(3): 531–532.

van Genuchten, M.Th. 1980. A closed-form equation for predicting the hydraulic conductivity of unsaturated soils1. Soil Sci. Soc. Am. J. 44(5): 892–898.

Wang, Z., W.A. Jury, A. Tuli, and D.-J. Kim. 2004. Unstable Flow during Redistribution: Controlling Factors and Practical Implications. Vadose Zone J. 3(2): 549–559.

Weller, U., O. Ippisch, M. Köhne, and H.-J. Vogel. 2011. Direct measurement of unsaturated conductivity including hydraulic nonequilibrium and hysteresis. Vadose Zone J. 10(2): 654.

Wildenschild, D., J.W. Hopmans, and J. Simunek. 2001. Flow rate dependence of soil hydraulic characteristics. Soil Sci. Soc. Am. J. 65(1): 35–48.

Xiong, Y. 2014. Flow of water in porous media with saturation overshoot: A review. J. Hydrol. 510: 353–362.

Chapter 7

Experimental Investigation of Hysteretic Dynamic Capillarity Effects in Unsaturated Flow

Prepared for submission to Water Resources Research, Zhuang, L., S.M. Hassanizadeh, C. Qin and A. de Waal.

Abstract

Macroscopic capillary pressure, defined as the difference in average pressures of two immiscible fluids, is commonly assumed only to be a function of saturation. However, under transient conditions, a dependency of the pressures difference on the time rate of saturation change has been observed by many researchers. This is commonly referred to as dynamic capillarity effect. In a linear approximation, the dynamic term is linearly dependent on the time rate of change of saturation, with a coefficient denoted by τ. In this study, a series of laboratory experiments was carried out to quantify the dynamic capillarity effect in an unsaturated sandy soil. Both static and dynamic primary, main and scanning drainage experiments were performed in a small-volume cell with highly sensitive pressure transducers. The value of the dynamic capillarity coefficient τ was calculated from the air-water pressure difference and average saturation measurements during static and dynamic drainage experiments. We found a dependence of τ on saturation, which showed a similar trend for drainage conditions. With the decrease in saturation, its value varied minimally at moderate saturation values, but then increased nearly linearly with saturation afterwards. Nevertheless, the magnitude of τ for primary drainage was found to be larger than for main drainage over the entire saturation range, while τ values were much smaller for scanning drainage loops. This implies that the relationship between τ and saturation is hysteretic. The values of τ obtained in our study, ranging from 5×10^4 to 3×10^6 Pa·s, were consistent with those reported in the literature for sand.

7.1 Introduction

Capillary pressure is of importance in the quantification of multiphase flow in porous media. Capillary pressure is defined as the difference between the pressures of two fluids, and is always expressed as a function of saturation. The resulting relationship is commonly measured during quasi-static conditions. However, due to the dynamics of multiphase flow, particularly for fine porous media, measurements of the capillary pressure curves are time-consuming, often taking weeks or even months. Experimental methods therefore have been developed for rapid measurements of the relationship between capillary pressure and saturation (e.g., Topp and Peters, 1967; Smiles et al., 1971; Vachaud et al., 1972; Elzeftawy and Mansell, 1975; Stauffer, 1978; Wildenschild et al., 2001). However, many observed a rate-dependency in this relationship when obtained using fast measurements. A number of concepts and formulations have been proposed to describe this phenomenon (Stauffer, 1978; Barenblatt and Gil'man, 1987; Kalaydjian, 1992; Hassanizadeh and Gray, 1993).

In this study we follow the thermodynamic approach proposed by Hassanizadeh and Gray (1990, 1993). In this approach, capillary pressure is shown to be equal to the difference in fluid pressures only during quasi-static conditions. However, they are not the same under dynamic conditions. The difference is found to depend on the time rate of change of saturation. The following linear approximation was proposed by Hassanizadeh and Gray (1993):

$$p^n - p^w - p^c = -\tau \frac{\partial S^w}{\partial t} \tag{7.1}$$

where p^n and p^w are non-wetting and wetting phase pressures, respectively, p^c is the capillary pressure, S^w is the wetting phase saturation, and τ is a dynamic (or non-equilibrium) capillarity coefficient. The dynamic capillarity coefficient τ is a damping coefficient depending in principle on material properties. Clearly, the difference between the two fluid pressures is equivalent to the capillary pressure under quasi-static conditions (i.e. $\partial S^w/\partial t=0$).

The values reported for τ in the literature vary over a wide range. Hassanizadeh et al. (2002) calculated approximate values of τ, ranging from 3×10^4 to 5×10^7 Pa·s, based on published experimental studies of dynamic capillarity effects. The values of τ in numerical (e.g., see Joekar-Niasar and Hassanizadeh (2012) for a review) and experimental studies (e.g., O'Carroll et al., 2005; Camps-Roach et al., 2010; Sakaki et al., 2010; Goel and O'Carroll, 2011; Bottero et al., 2011; Das and Mirzaei, 2012) have

been mostly within this range. Part of the variation in reported values can be explained by the fact that τ depends on saturation. However, various experimental studies have reported different or even contradictory dependences of τ on saturation. Some studies have reported that τ varies only slightly with saturation (e.g., Oung et al., 2005; Camps-Roach et al., 2010; Bottero et al., 2011), while others found that the value of τ increases or decreases as the saturation decreases (e.g., Sakaki et al., 2010; Das and Mirzaei, 2012).

The scale-dependence of τ has also been reported in the literature. In addition to the numerical study by Manthey et al. (2008), experimental works have been performed in experimental setups at different scales (O'Carroll et al., 2005, 2010; Oung et al., 2005; Camps-Roach et al., 2010; Sakaki et al., 2010; Goel and O'Carroll, 2011; Bottero et al., 2011; Das and Mirzaei, 2012). Among these, relatively few experimental studies have been carried out in small-volume sand columns (Hassanizadeh et al., 2004; Hou et al., 2012; Abidoye and Das, 2014). Hassanizadeh et al. (2004) estimated the magnitude of τ based on a series of PCE-water drainage experiments, ranging from 5×10^5 to 6×10^5 Pa·s. Abidoye and Das (2014) calculated τ values from silicone oil-water drainage experiments in sand columns having three different heights (4 cm, 8 cm and 12 cm). They found that the value of τ increased as saturation decreased, ranging from 2×10^5 to 1×10^7 Pa·s for silicone oils with different viscosities. Using an experimental unsaturated system, Hou et al. (2012) found τ values of 10^3 Pa·s or even less during dynamic drainage in a small sand column. Almost all studies have involved primary drainage processes. Note that no experimental studies have investigated or provided any information about the dynamic capillarity coefficient for scanning drainage or imbibition processes, which are dominant in many practical applications.

In order to address some of the contradictions and shortcomings mentioned above, we performed a series of dynamic drainage experiments in a small-volume unsaturated sand sample. The relationships between capillary pressure and saturation were first measured under equilibrium conditions. Afterwards, primary, main and scanning drainage experiments were carried out to investigate capillarity effects during transient drainage. Because the response time of the measurement devices could influence the estimation of dynamic capillarity, we used pressure transducers with a very fast response to collect water pressure readings during experiments. Results of experiments are used to estimate the values of the dynamic capillarity coefficient, for scanning as well as primary and main drainage processes, as a function of saturation.

7.2 Materials and methods

7.2.1 Materials

The sand used in all experiments was obtained from a sand mining site (Sibelco, Antwerp, Belgium). The sand had a relatively narrow pore size distribution with particle diameters ranging from 0.1 to 0.5 mm. Prior to use, the soil was rinsed with deionized water and then air dried, to remove fine clay particles. The sand properties are listed in Table 7.1. All experiments were conducted under unsaturated conditions, with air as the non-wetting phase. Deionized, distilled, and degassed water was used as the wetting phase.

Table 7.1 Properties of the sand used in experiments

Properties	Value
Mean particle diameter, d_{50} (mm)	0.20
Particle density, ρ_s (g cm^{-3})	2.56
Intrinsic permeability, (m^2)	1.7×10^{-11}
Average porosity, φ, (-)	0.39

7.2.2 Experimental Setup

All experiments were conducted using a custom-built Plexiglas sandbox. A schematic view of the experimental setup is shown in Figure 7.1. The dimensions of the sandbox were 3 cm (height) by 3 cm (length) by 2 cm (width). A valve at the top of sandbox (Valve 1) was connected to a balloon, filled with moist air, to keep constant atmospheric pressure. At the bottom of sandbox we used a hydrophilic nylon membrane (VWR International B.V., the Netherlands; mean pore size, 5 μm), supported by a stainless-steel porous plate, to serve as a capillary barrier to air. The water reservoir at the bottom of setup was connected with a short tube to a small water column, which was used to control the pressure head at the outlet. The small hanging column had an overflow to allow drained water to leave and thus keep ro the water head in the column constant. For the main and scanning drainage processes, the saturated sand sample was first drained to reach irreducible saturation, after which extra water was added to keep water level at the outflow level during main imbibition. Silicone tapes were used at all joints to avoid any leakage. The entire sandbox was fixed with the aid of a frame on a 3-digit precision balance (Kern & Sohn GmbH,

Germany). Readings of the balance were used to calculate changes in average saturation.

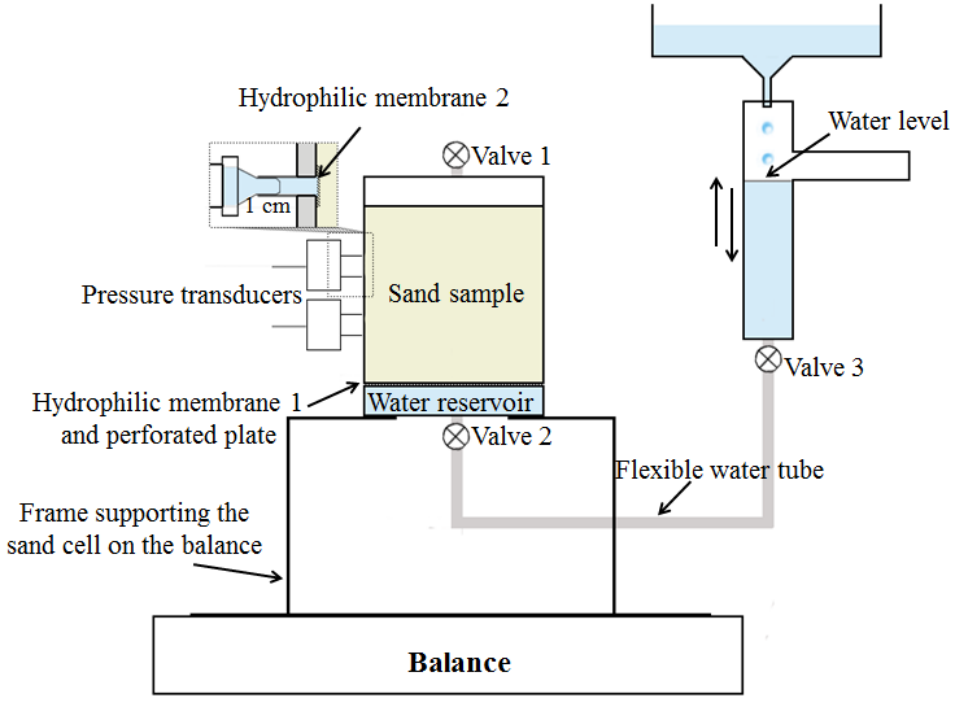

Figure 7.1 Schematic view of the experimental setup

Two pressure transducers (HMUM100, First Sensor, Germany) were installed at depths of 1 and 2 cm of the sandbox. An enlargement of the part between the transducer and the sand sample is shown in the inset of Figure 7.1. The dead volume of the transducer was saturated with water before installation. The transducer was connected with a1-cm water-saturated tube to the side wall of the sandbox, with an opening of 5 mm in diameter. A hydrophilic membrane (PVDF, Mdimembrane, India) with a mean pore size of 0.45 μm was adhered to the opening of the internal wall of the sandbox. The membrane was saturated with degassed water in all experiments. The two pressure transducers were connected to a CR1000 data logger (Campbell Scientific, Shepshed, UK). The pressure transducers were calibrated with hydrostatic water pressures prior to use in the experiments. The response time of the transducers was determined to be 0.4 seconds, based on a test explained in Appendix G.

7.2.3 Quasi-static and dynamic drainage experiments

The experimental setup was first mounted with the bottom reservoir full of water and without the top lid. Deionized and degassed water was used to minimize air entrapment. The sand was packed continuously by pouring dry sand into the water through a funnel, and it was regularly tapped. A small comb was used to mix the sand as it was being poured into water to avoid layering. This resulted in a fairly uniform packing. The top cover was then installed. The sand sample was fully saturated initially and was repacked so as to have almost the same weight for all experiments.

In quasi-static experiments, the hanging water column was kept at the same level as the bottom of the sand sample at first. Valve 2 and Valve 3 (see Figure 7.1) were always open. The elevation of the hanging column was decreased, or increased, in small increments (1.5-2 cm H_2O) for drainage, and imbibition, respectively. The readings from pressure transducers were monitored to ensure that the equilibrium was established before each change of elevation. The duration was almost two weeks for each p^c-S^w loop (from primary drainage to main imbibition to main drainage, or to scanning drainage).

In the dynamic drainage experiments, the saturated sand sample was first drained (for primary drainage) or drained and imbibed (for scanning and main drainage) under quasi-static conditions. After reaching the certain water saturation and pressures (as the initial conditions for dynamic experiments later on), Valve 3 was closed and the hanging water column was lowered to -70 cm H_2O below the bottom of the sandbox. Dynamic drainage experiments started by opening Valve 3. This resulted in a rapid drainage of the sand sample. Local water pressures and average water saturation were collected every 0.5 s for 4000 s at most. Given that the starting conditions for each loop of dynamic drainage (primary, scanning or main) experiments were almost the same (less than 3% difference), we assumed that the same water saturation in the sand sample was established for each set of drainage experiments.

In principle, dynamic imbibition experiments could be done also using the above experimental setup. However, we monitored the average saturation and the water pressures at two elevations, 1 cm and 2 cm, from the bottom of the sandbox during the experiments. The initial saturation of the main imbibition curve was approximately irreducible saturation, resulting in a very low permeability of the sand sample. We found that the average saturation started to change, while water pressure changes were monitored after several seconds during the dynamic imbibition process. Clearly, water started to accumulate at the bottom of the sand sample, and then moved slowly upwards to pass through the pressure transducers. This caused some mismatches

between the saturation and the pressure readings during the dynamic imbibition processes. For this reason we focused in this study only on the dynamic drainage experiments, while recognizing that further improvements of the experimental setup are needed for dynamic imbibition studies.

All experiments were conducted at a constant-temperature room at 21±0.5ºC. At least two replicates were conducted for each set of experiments. Because of the close overlap of the replicates, only one measurement set is shown here.

7.3 Results

7.3.1 Quasi-static experiments

The p^c-S^w data obtained under quasi-static conditions are shown in Figure 7.2. Different symbols represent measured data during the primary, main and scanning drainage and main imbibition processes. The measured data were fitted by the van Genuchten equations (1980) written as

$$p^c(S^w) = \frac{1}{\alpha}\left[S_e^{-1/m} - 1\right]^{1/n} \tag{7.2}$$

where effective saturation S_e is expressed as

$$S_e = \frac{S^w - S_{ir}^w}{1 - S_{ir}^w - S_r^a} \tag{7.3}$$

in which S_{ir}^w, S_r^a and S_e are irreducible water saturation, residual air saturation, and effective water saturation, respectively, α and n are fitting parameters, and m=1-1/n. The fitted curves are shown as dashed lines in Figure 7.2. The irreducible water saturation S_{ir}^w was fixed at the same value for all p^c-S^w curves. The residual air saturationS_r^a, α and n were fitted iteratively. The resulting parameters are listed in Table 7.2. These fitted curves were used to calculate the values of the dynamic capillarity coefficient τ later on.

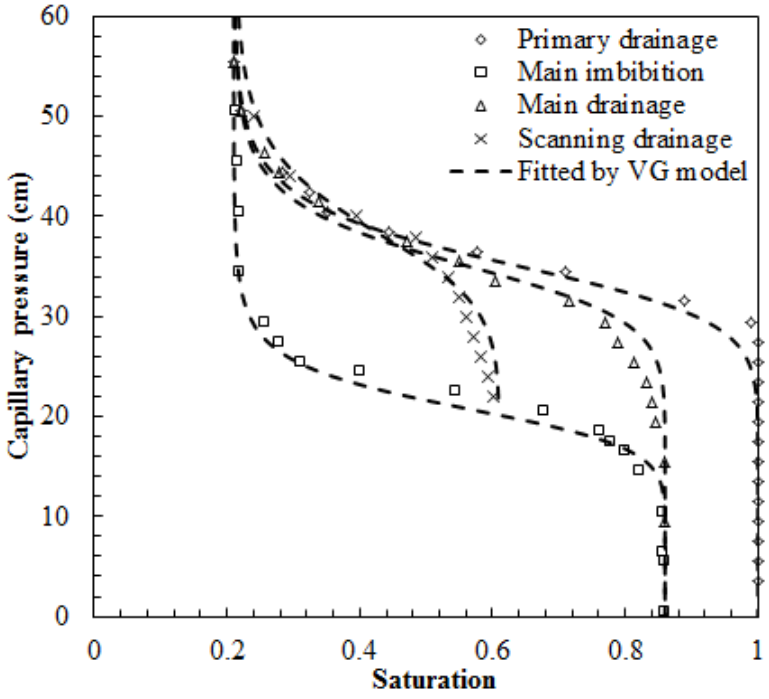

Figure 7.2 Capillary pressure-saturation curves under quasi-static conditions

Table 7.2 Values of the fitted van Genuchten parameters

Experiment	α (cm^{-1})	n	S_{ir}^{w}	S_{r}^{a}
Primary drainage	0.0284	12	0.21	0
Main imbibition	0.048	10	0.21	0.14
Main drainage	0.0284	12	0.21	0.14
Scanning drainage	0.026	10	0.21	0.39

7.3.2 Dynamic drainage experiments

Measured water pressures at two elevations as a function of time during primary, main and scanning drainage are shown in Figures 7.3a, 7.3c and 7.3e, respectively. We note that only water pressures at the early stage are shown here, when large changes occurred in water pressure and saturation. As can be seen, water pressures for all drainage processes reacted immediately as soon as Valve 3 (Figure 7.1) was opened.

The water pressure changed much more rapidly during dynamic main drainage than primary drainage, due to having similar saturation but being subject to a larger water pressure gradient initially. However, the water pressure decreased gradually during dynamic scanning drainage, even with a larger initial water pressure gradient than primary drainage. This is probably caused by the lower permeability at the lower initial saturation during scanning drainage.

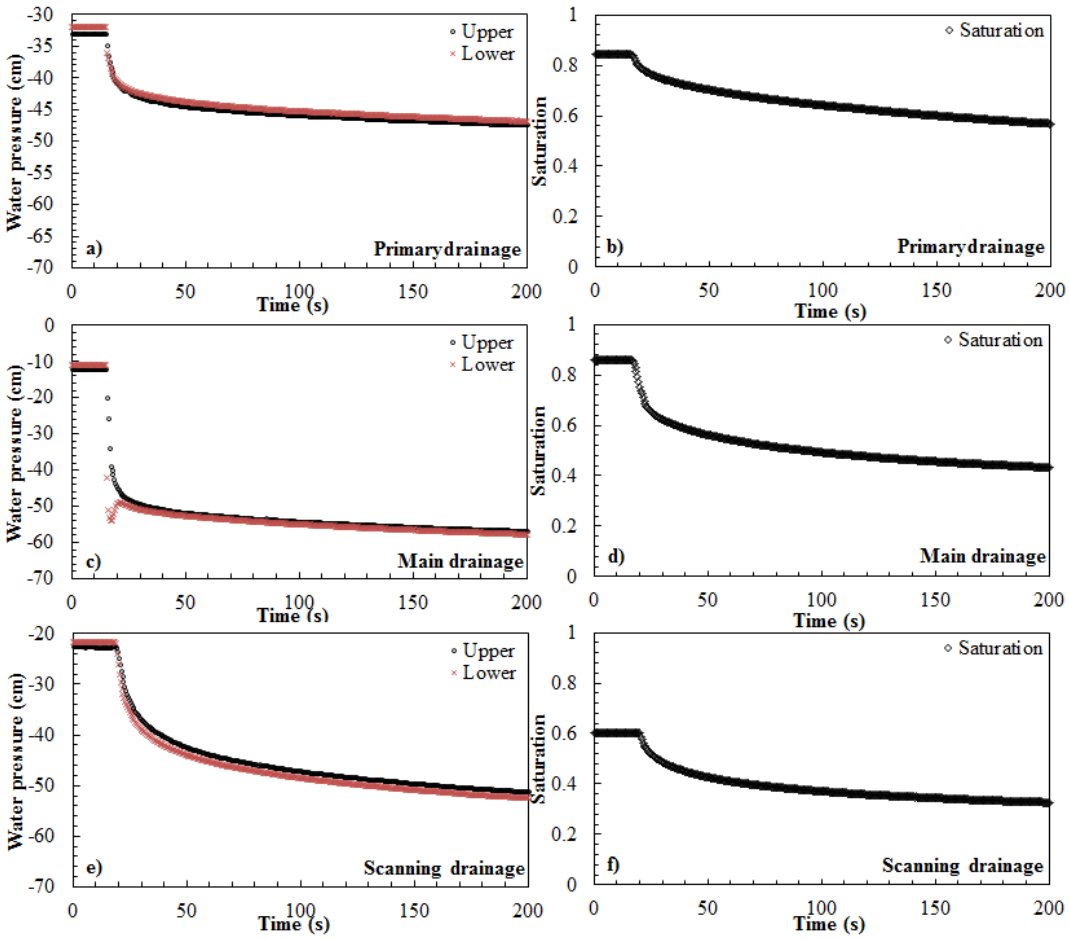

Figure 7.3 The changes of water pressure and saturation with time during dynamic drainage experiments: primary (a, b), main (c, d) and scanning (e, f)

One interesting phenomenon we observed was that the water pressure measured by the lower pressure transducers, which were close to the outlet, showed a non-monotonic behavior during dynamic main drainage (Figure 7.3c), while water pressures decreased

monotonically during other dynamic processes. This non-monotonic behavior in water pressure was observed earlier by Bottero et al. (2011) who performed a series of dynamic primary drainage experiments with different injection pressures in a PCE-water system. Their experimental results showed that at high injection pressures (when dynamic capillarity became important), the measured capillary pressure became non-monotonic at the location close to the injection boundary, after which non-monotonicity appeared at all measurement locations for even higher imposed pressures. Furthermore, this non-monotonic behavior in capillary pressure could be modelled only by accounting for dynamic capillarity effects (Berentsen et al., 2006; Bottero, 2009).

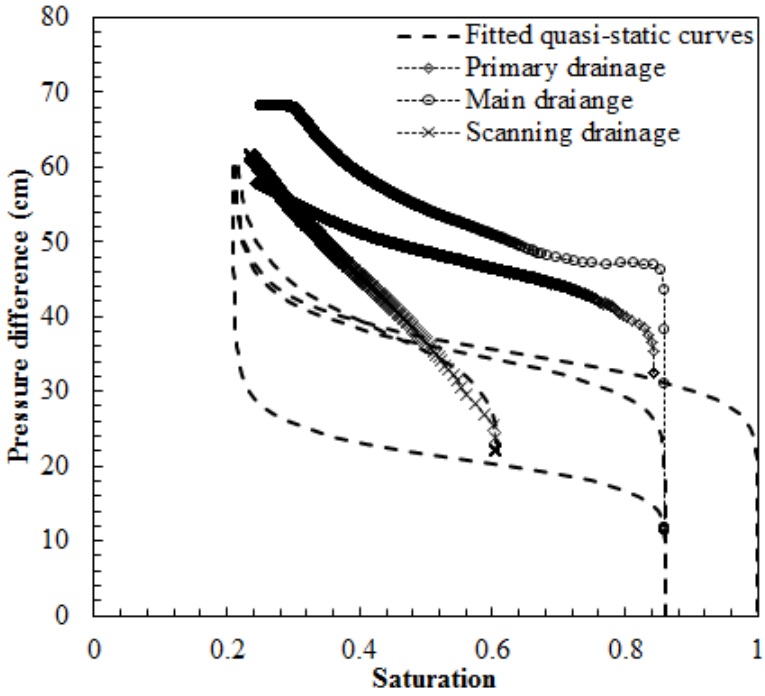

Figure 7.4 Measured pressure difference-saturation curves for dynamic primary, main and scanning drainage experiments

Since we measured average saturations during the experiments, we calculated corresponding arithmetic mean pressure values based on readings of the two pressure transducers. Average pressure differences are plotted as a function of saturation in Figure 7.4. The van Genuchten fitted quasi-static curves are shown as dashed lines. The pressure differences for dynamic primary and main drainage were larger than the

capillary pressure under quasi-static conditions at any saturation. However, for dynamic scanning drainage, the pressure difference-saturation curve coincided with the quasi-static curve when $0.5<S_w<0.6$, and then increased almost linearly. The pressure difference-saturation curve for dynamic main drainage is the highest one among these. It is evident that the deviation in pressure difference between dynamic and quasi-static processes depends on both the imposed boundary and initial conditions (Camps-Roach et al., 2010; Sakaki et al., 2010; Bottero et al., 2011).

Figures 7.3b, 7.3d and 7.3f show the change in saturation with time during dynamic primary, main and scanning drainage processes, respectively. Saturation in all cases decreased rapidly at the early stages and then more gradually later on. For these graphs, the rate of change in saturation with time, $\partial S^w/\partial t$, was calculated and plotted as a function of saturation, shown in Figure 7.5. As expected, the absolute values of $\partial S^w/\partial t$ in all dynamic drainage experiments increased dramatically to reach a maximum value, and then gradually approached zero. The largest maximum value was found to be 0.05 s^{-1} during main drainage, while it was smallest, around 0.02 s^{-1}, during primary drainage.

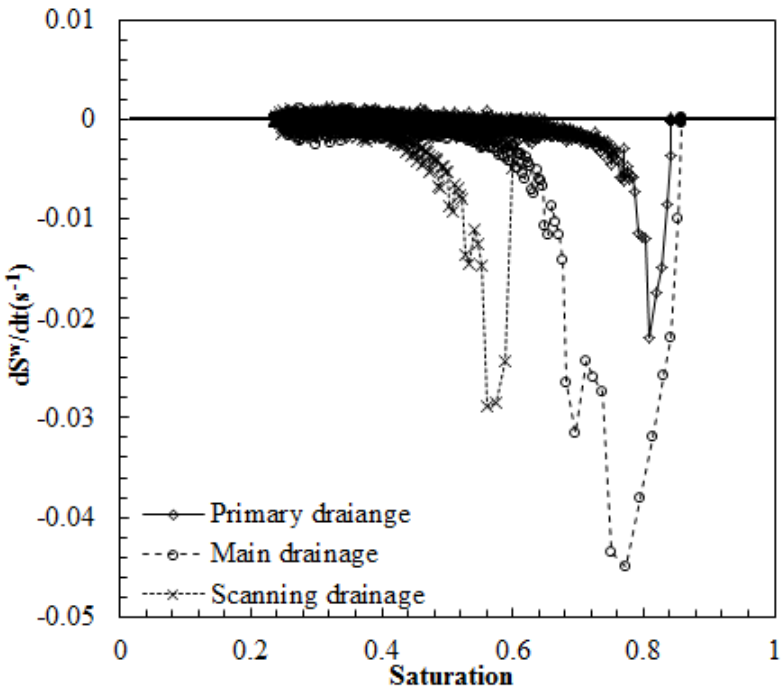

Figure 7.5 $\partial S^w/\partial t$ as a function of saturation for primary, main and scanning drainage

$$\tau(S^w) = \frac{p^c(S^w) + p^w}{\partial S^w / \partial t} \tag{7.4}$$

At any given time, the average saturation S^w and water pressure p^w were measured as explained earlier. The corresponding quasi-static capillary pressure was calculated using the fitted van Genuchten equation given by Equation (7.2), while the corresponding time derivative of saturation, $\partial S^w/\partial t$, was estimated using a backward difference approximation. The resulting values of τ are plotted as a function of saturation in Figure 7.6. Only positive values are shown, while values calculated based on small values of $\partial S^w/\partial t$ were discarded.

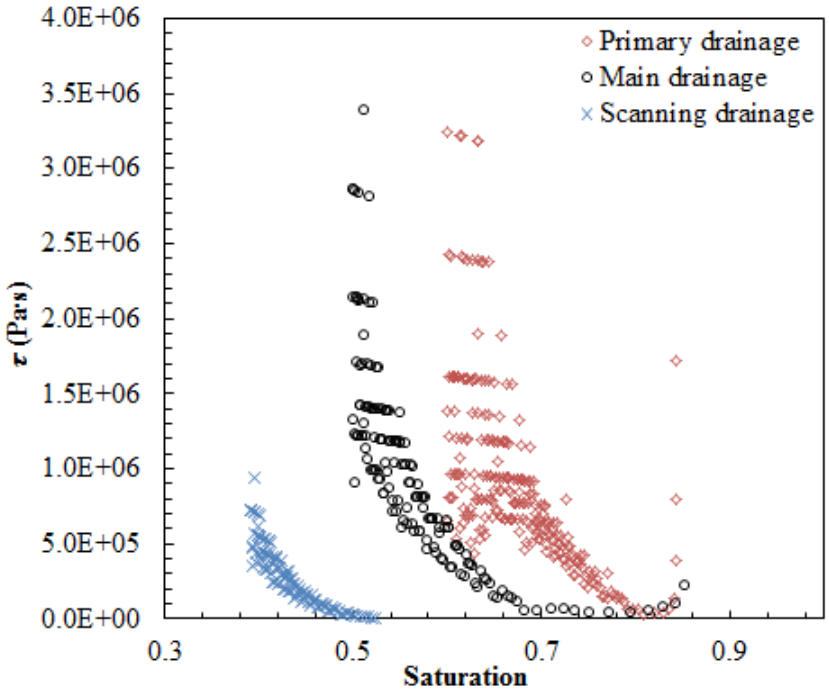

Figure 7.6 Calculated τ values for primary, main and scanning drainage

7.4 Discussion

7.4.1 Saturation dependence of τ

The values of τ for primary, main and scanning drainage were shown in Figure 7.6 using different colored symbols. As can be seen, as saturation decreased for primary drainage, the value of τ first decreased to reach a minimum value 5×10^4 Pa·s, then

stayed at this value when $0.77<S^w<0.85$, and increased nearly linearly afterwards. A similar trend is apparent for main drainage, but the values of τ stayed almost constantly around 5×10^4 Pa·s within $0.70<S^w<0.85$. By comparison, calculated τ values were almost zero or even slightly negative when $0.50<S^w<0.60$ for scanning drainage, after which τ increased linearly as saturation decreased, similar to the trends for primary and main drainage. The calculated τ values range from 5×10^4 to 3×10^6 Pa·s for both primary and main drainage within $0.50<S^w<0.85$, while τ values also increased to around 3×10^6 Pa·s within $0.30<S^w<0.50$ for scanning drainage. One interesting behavior shown in Figure 7.6 is that the τ-S^w relationship is similar for primary, main and scanning drainage. However, differences in τ values do exist for different drainage processes, thus implying that the τ-S^w relationship is hysteretic. We note that the time derivative of saturation was only calculated based on the mass loss of the entire sand sample. Even though this averaging of $\partial S^w/\partial t$ may lead to some overestimation of τ, it does not change the order of magnitude of τ. We discuss this effect in more detail in the next section.

In our work, as saturation decreased for primary and main drainage, the value of τ was found to decrease at first, and then mostly stayed constant, followed by an almost linear increase. A similar trend for primary or main drainage has been reported in the literature (Camps-Roach et al., 2010; Sakaki et al., 2010; Goel and O'Carroll, 2011; Abidoye and Das, 2014). Bottero et al. (2011) reported that the value of τ varies little within $0.50<S^w<0.85$, while the value of τ in our work also changed little within $0.60<S^w<0.85$ for main drainage. However, O'Carroll et al. (2005) performed inverse modeling using a negative linear τ-S^w relationship over the entire saturation range, inconsistent with the τ-S^w dependence we found in our study The flexibility and uncertainty of the numerical method used in the inverse analysis may have to be a concern.

Hysteresis in the τ-S^w relationship has only been reported by Mirzaei and Das (2013) and Sakaki et al. (2010) for primary drainage and main imbibition. We emphasize that more experiments need to be done to investigate this hysteretic behavior.

7.4.2 Inaccuracies in the estimation of τ

Scale-dependence of the dynamic capillarity coefficient τ has been reported in experimental studies by Bottero et al. (2011) and Abidoye and Das (2014), and in numerical studies by Manthey et al. (2005) and Dahle et al. (2005). We note that some measurement artifacts may exist in the estimation of τ. In our study, saturation was

calculated based on the total mass change of the entire sample. To some extent, the averaged $\partial S^w/\partial t$ may be smaller than local $\partial S^w/\partial t$ values, leading to over-estimation of τ values. In fact, Bottero et al. (2011) showed that the local $\partial S^w/\partial t$ may be an order of magnitude larger than the average $\partial S^w/\partial t$ over the length of 11 cm of their setup. However, we note that their experiments were done in a PCE-water system, with heavier PCE displacing water vertically up. This may have led to a very sharp PCE-water front, which in turn may have caused a large difference between local and average values of $\partial S^w/\partial t$. In air-water systems, air is much less viscous and lighter than water, while in our setup the displacement was downward. Thus, there was no sharp front, leading to small differences between average and local $\partial S^w/\partial t$ values. Camps-Roach et al. (2010) have reported that there is almost no difference between the local and average values of $\partial S^w/\partial t$ for a domain of 9 cm long. Moreover, based on numerical simulations in air-water system, Hou et al. (2014) found that the local values can be approximated by the average values, even for a 15 cm long sand column.

Determinations of the dynamic capillarity coefficient τ are very much based on dynamic processes. This means that rapid measuring times are needed to capture the dynamics. However, the response time of the devices limits the measuring time. Due to much shorter times in which the rate of saturation changed in our experiments than in other studies, notably Camps-Roach et al. (2010) and Bottero et al. (2011), the measuring time was set to be 0.5 s. The maximum time derivative of saturation reported by Hou et al. (2012) was around 0.03 s^{-1}, which is close to the value in our experiments, 0.05 s^{-1}. However, the values of τ reported in their work are at least one order of magnitude smaller than in our study. The measuring time of pressure transducers was set to be 0.1 s in their experiments, which was much smaller than the response time (the latter being more than 2 s). Even if they corrected the readings of the pressure transducers based on the response time, it seems that still an important mismatch may exist.

7.5 Summary and conclusions

A series of drainage experiments were carried out to quantify the dynamic capillarity effect in an unsaturated soil. Primary, main and scanning drainage experiments were performed under both quasi-static and dynamic conditions. The value of the dynamic capillarity coefficient τ was calculated based on average pressure difference and saturation measurements during static and dynamic drainage experiments.

A similar dependence between τ and saturation was found for primary, main and scanning drainage. With the decrease in saturation, the value of τ varied slightly at moderate saturation levels, but then increased nearly linearly afterwards. Nevertheless, the magnitude of τ for primary drainage was found to be larger than main drainage over the entire saturation range, while the τ value was much smaller for scanning drainage. This implies that the relationship between τ and saturation is hysteretic. This hysteretic behavior in the value of τ has rarely been reported before. The value of τ in our study was found to vary from 5×10^4 to 3×10^6 Pa·s for primary and main drainage, consistent with reported values of air-water systems.

7.6 Appendix G: Verifying the response time of pressure transducers

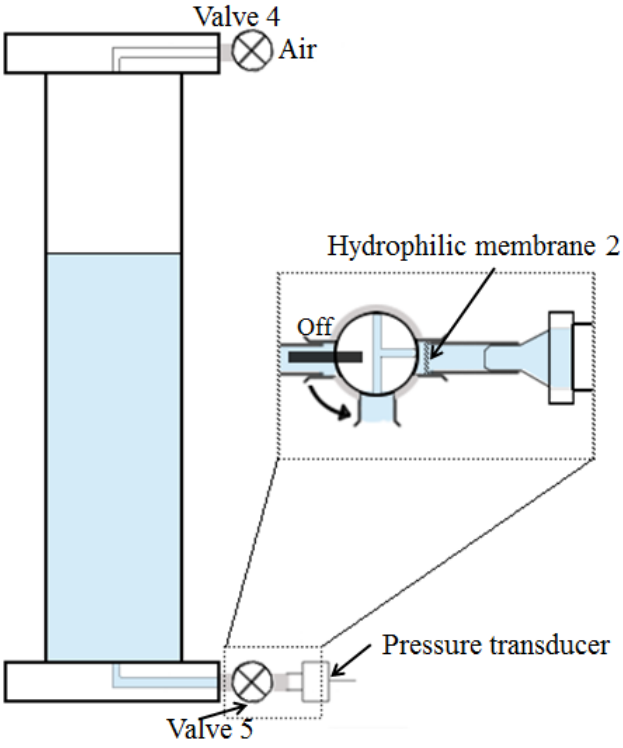

Figure 7.7 Experiment setup to test the response time of pressure transducers

Preliminary tests were conducted to verify the response time of the pressure transducers. A schematic view of the test experimental setup is shown in Figure 7.7. The idea was to monitor the readings of the pressure transducer when a sudden pressure difference is applied. The duration to reach stable readings of the pressure

transducer is set to be the response time. To do so, degassed water was filled into a Plexiglas column (length=50 cm and ID=5 cm). The top of the column was open to air (Valve 4 was open). The pressure transducer was installed at the bottom of the column, through Valve 5. The enlargement of the connection part between the transducer and the column is shown as the inset in Figure 7.7. The pressure transducer was connected with a 1-cm short tubing. The hydrophilic membrane was fixes onto the other side of the tubing. The tubing was connected with the test column through a three-way valve (Valve 5). One way of the valve was open to air, while the other two ways were connected with the tubing and the test column. Before starting the test, the connection part was ensured to be water-saturated. Readings of the pressure transducer were recorded every 0.1 s. The way to the test column was first closed, meaning that the tube with the pressure transducer was connected to air (as shown in the inset). The reference readings of the transducer were collected, and then the way of the valve was changed to the column immediately. Readings of the transducer reached the corresponding stable values of the water head within 0.4 s.

Acknowledgements

We gratefully acknowledge Thom Claessen and Sander Deelen from Utrecht University for their technical support. The first author was supported by China Scholarship Council (No. 201206380076). The second author has received funding from the European Research Council under the European Union's Seventh Framework Program (FP/2007-2013)/ERC Grant Agreement No. 341225.

Reference

Abidoye, L.K., and D.B. Das. 2014. Scale dependent dynamic capillary pressure effect for two-phase flow in porous media. Adv. Water Resour. 74: 212–230.

Barenblatt, G.I., and A.A. Gil'man. 1987. Nonequilibrium counterflow capillary impregnation. J. Eng. Phys. 52(3): 335–339.

Berentsen, C.W., S.M. Hassanizadeh, A. Bezuijen, and O. Oung. 2006. Modelling of two-phase flow in porous media including non-equilibrium capillary pressure effects. *In* Proceeding of the XVI International Conference on Computational methods in Water Resources. Tech. Univ. of Denmark, Copenhagen, Denmark.

Bottero, S. 2009. Advances in the theory of capillarity in porous media. Ph.D. thesis, Utrecht University, Geologica Ultreietina, 314, 200 pp.

Bottero, S., S.M. Hassanizadeh, P.J. Kleingeld, and T.J. Heimovaara. 2011. Nonequilibrium capillarity effects in two-phase flow through porous media at different scales. Water Resour. Res. 47: W10505.

Brooks, R., and A. Corey. 1964. Hydraulic properties of porous media. Hydrol. Pap. Color. State Univ. 3(March): 37 pp.

Camps-Roach, G., D.M. O'Carroll, N.T. A., and S. Toshihiro. 2010. Experimental investigation of dynamic effects in capillary pressure: Grain size dependency and upscaling Geremy. Water Resour. Res. 44: W08544.

Dahle, H.K., M.A. Celia, and S.M. Hassanizadeh. 2005. Bundle-of-tubes model for calculating dynamic effects in the capillary-pressure-saturation relationship. Transp. Porous Media 58(1): 5–22.

Das, D.B., and M. Mirzaei. 2012. Dynamic effects in capillary pressure relationships for two-phase flow in porous media: experiments and numerical analyses. AIChE J. 58(12): 3891–3903.

Elzeftawy, A., and R.S. Mansell. 1975. Hydraulic conductivity calculations for unsaturated steady-state and transient-state flow in sand. Soil Sci. Soc. Am. J. 29(3): 599-603.

Goel, G., and D.M. O'Carroll. 2011. Experimental investigation of nonequilibrium capillarity effects: Fluid viscosity effects. Water Resour. Res. 47(9): 1–15.

Hassanizadeh, S.M., M.A. Celia, and H.K. Dahle. 2002. Dynamic effect in the capillary pressure-saturation relationship and its impacts on unsaturated flow. Vadose Zone J. 1(1): 38–57.

Hassanizadeh, S.M., and W.G. Gray. 1990. Mechanics and thermodynamics of multiphase flow in porous media including interphase boundaries. Adv. Water Resour. 13(4): 169–186.

Hassanizadeh, S.M., and W.G. Gray. 1993. Thermodynamic basis of capillary-pressure in porous-media. Water Resour. Res. 29(10): 3389–3405.

Hassanizadeh, S.M., O. Oung, and S. Manthey. 2004. Laboratory experiments and simulations on the significance of non-equilibrium effect in the capillary pressure-saturation relationship. p. 3–14. *In* Unsaturated Soil: Experimental Studies: Proc. Int. Conf.: From experimental evidence towards numerical modeling of unsaturated soils. Weimar, Germany.

Hou, L., L. Chen, and T.C.G. Kibbey. 2012. Dynamic capillary effects in a small-volume unsaturated porous medium: Implications of sensor response and gas pressure gradients for understanding system dependencies. Water Resour. Res. 48: W11522.

Hou, L., B.E. Sleep, and T.C.G. Kibbey. 2014. The influence of unavoidable saturation averaging on the experimental measurement of dynamic capillary effects: A numerical simulation study. Adv. Water Resour. 66: 43–51.

Joekar-Niasar, V., and S.M. Hassanizadeh. 2012. Analysis of Fundamentals of Two-Phase Flow in Porous Media Using Dynamic Pore-Network Models: A Review. Crit. Rev. Environ. Sci. Technol. 42(18): 1895–1976.

Joekar-Niasar, V., and S. Majid Hassanizadeh. 2011. Effect of fluids properties on non-equilibrium capillarity effects: Dynamic pore-network modeling. Int. J. Multiph. Flow 37(2): 198–214.

Kalaydjian, F.-M. 1992. Dynamic capillary pressure curve for water/oil displacement in porous media: Theory vs. experiment. *In* SPE Annual Technical Conference and

Exhibition. Society of Petroleum Engineers.

Manthey, S., S.M. Hassanizadeh, and R. Helmig. 2005. Macro-scale dynamic effects in homogeneous and heterogeneous porous media. Transp. Porous Media 58(1–2): 121–145.

Manthey, S., S.M. Hassanizadeh, R. Helmig, and R. Hilfer. 2008. Dimensional analysis of two-phase flow including a rate-dependent capillary pressure–saturation relationship. Adv. Water Resour. 31: 1137–1150.

Mirzaei, M., and D.B. Das. 2013. Experimental investigation of hysteretic dynamic effect in capillary pressure-saturation relationship for two-phase flow in porous media. AIChE J. 59(10): 3958–3974.

O'Carroll, D.M., K.G. Mumford, L.M. Abriola, and J.I. Gerhard. 2010. Influence of wettability variations on dynamic effects in capillary pressure. Water Resour. Res. 46(8): 1–13.

O'Carroll, D.M., T.J. Phelan, and L.M. Abriola. 2005. Exploring dynamic effects in capillary pressure in multistep outflow experiments. Water Resour. Res. 41(11): 1–14.

Oung, O., S.M. Hassanizadeh, and A. Bezuijen. 2005. Two-phase flow experiments in a geocentrifuge and the significance of dynamic capillary pressure effect. J. Porous Media 8(3): 247–257.

Sakaki, T., D.M. O'Carroll, and T.H. Illangasekare. 2010. Direct Quantification of Dynamic Effects in Capillary Pressure for Drainage–Wetting Cycles. Vadose Zone J. 9(2): 424–437.

Smiles, D.E., G. Vachaud, and M. Vauclin. 1971. A test of the uniqueness of the soil moisture characteristic during transient, nonhysteretic flow of water in a rigid soil1. Soil Sci. Soc. Am. J. 35(4): 534–539.

Stauffer, F. 1978. Time dependence of the relations between capillary pressure, water content and conductivity during drainage of porous media. p. 3–35. *In* IAHR symposium on scale effects in porous media, Thessaloniki, Greece.

Topp, G., and A. Peters. 1967. Comparison of water content-pressure head data obtained by equilibrium, steady-state, and unsteady-state methods1. Soil Sci. Soc. Am. J. 31(3): 312–314.

Vachaud, G., M. Vauclin, and M. Wakil. 1972. A study of the uniqueness of the soil moisture characteristic during desorption by vertical drainage. Soil Sci. Soc. Am. J. 36(3): 531–532.

van Genuchten, M.T. 1980. A closed-form equation for predicting the hydraulic conductivity of unsaturated soils1. Soil Sci. Soc. Am. J. 44(5): 892–898.

Wildenschild, D., J.W. Hopmans, and J. Simunek. 2001. Flow rate dependence of soil hydraulic characteristics. Soil Sci. Soc. Am. J. 65(1): 35–48.

Chapter 8

Summary and Recommendations

8.1 Summary

The main objective of this study was to investigate the validity and applicability of advanced theories of two-phase flow in porous media.

We first performed a series of numerical simulations based on a water horizontal redistribution experiment reported in the literature. Two different models, the standard Richards equation and an interfacial area model, were employed and compared in terms of their ability to reproduce the experimental data. The Richards equation was used with and without accounting for hysteresis, while for the interfacial area model we used two different formulations for Darcy's law. As expected, the standard model without hysteresis gave results that were at odds with the observations. In particular, the standard model produced a full redistribution of water and complete disappearance of the saturation discontinuity between the two sides of the experimental setup. The hysteretic Richards model did lead to a non-uniform saturation distribution and properly simulated the saturation discontinuity. However, the flow process was found to be much faster than observed, and saturation values in the dry side were significantly over-predicted. The differences could be minimized only if unrealistic values were assigned to some of the soil hydraulic parameters. The interfacial area model produced better agreement with the observed spatial and temporal saturation distributions. To some extent this was expected since this model contains more parameters. Nevertheless, the fact that the interfacial area model predicted the persistence of the discontinuity in saturation, using the same set of hydraulic properties for both sides, confirms the hypotheses of the interfacial area model in terms of simulating capillary hysteresis.

However, based on the simulation results, we realize that better controlled experiments should be performed to ensure homogeneous soil packing and more precise direct measurement of the initial conditions. This could reduce uncertainties in the experimental data and theoretical analyses.

Next, we designed and performed a series of well-defined water redistribution experiments in an unsaturated soil. A custom-built long Plexiglas sandbox was employed to conduct three sets of experiments with different initial water saturations in the dry side. The gamma transmission method was used during the experiments to measure water saturations at different locations along the sandbox, while water and air tensiometers were installed at various positions to collect pressure data. A water discontinuity across the discontinuity persisted during all experiments, while measured

water pressures near the discontinuity became continuous immediately after the experiments started. We observed that less water was redistributed when the difference in the initial water saturation between the dry and wet side was smaller. These experiments were also simulated using the two models mentioned above. By adding hysteresis to the production term of the specific interfacial area, the interfacial area model gave similar or even better agreement with these three sets of experiments, than the standard Richards model.

In addition to the specific interfacial area, we also investigated the dynamic capillarity effect. We first simulated the results obtained from the experiments on downward infiltration of water into almost dry soil. The two models mentioned earlier were again used, including a dynamic capillarity equation. Results of all simulations with the hysteretic Richards model deviated substantially from the experimental data. Without the dynamic capillarity term, completely monotonic saturation profiles were obtained regardless of the kind of hysteresis included. This was consistent with previous studies by other researchers. When including the dynamic term, the Richards model gave a sharp saturation overshoot if no hysteresis was included. When accounting for hysteresis in capillary pressure and/or relative permeability, then the overshoot showed a plateau structure. Because of considerable saturation overshoot, results obtained withy the hysteretic Richards model never showed good agreement with the data. The interfacial area model could capture saturation overshoots observed in experiments with different conditions very well. By fitting hysteretic values of the coefficient in the production term, the projected capillary curve for primary imbibition in the interfacial area model produced good agreement with measured values. To some extent, this indicates that the coefficient in the production term is determined by material properties and the history of the processes involved, similarly as the capillary curves. The dynamic capillarity coefficient τ was assumed to be a constant in these simulations. Nevertheless, many studies have shown that τ itself may be a function of saturation. Further experimental studies are therefore needed to determine the dependence of τ on saturation.

We further investigated the potential effect of the dependence of τ on saturation on the solutions of the equations. We considered four different expressions for the dependence of τ on saturation: constant, an integrable decreasing function, an increasing function and a non-integrable increasing function. We performed a traveling wave analysis of the full equations using parameter values of a recent water infiltration experiment. Based on traveling waves and simulation results, the solutions obtained with the non-integrable increasing function gave a saturation overshoot similar to the

one found in experiments but with significantly earlier arrival times. The traveling waves were only valid after a long distance. Nevertheless, they provided the same trend as obtained with simulations of the full equations.

Finally, to quantify the dynamic capillarity effect directly, a series of drainage experiments were carried out in an unsaturated soil. Primary, main and scanning drainage experiments were performed under both quasi-static and dynamic conditions. The value of the dynamic capillarity coefficient τ was calculated based on local pressure difference and average saturation measurements during static and dynamic drainage experiments. A similar trend of the dependency between τ and saturation was found for primary and main drainage. When saturation decreased from 0.9 to 0.4, the value of τ decreased slightly at first, then varied little at moderate saturation values, and then increased nearly linearly afterwards. The value of τ increased for scanning drainage as the saturation decreased from 0.5 to 0.3. The magnitude of τ for primary drainage was found to be larger than for main drainage over the entire saturation range, while τ values were much smaller for scanning drainage. This implies that the relationship between τ and saturation is non-unique (i.e., hysteretic). This hysteretic behavior in the value of τ has rarely been reported before. The value of τ in our study was found to vary from 1.5×10^5 to 4×10^6 Pa·s for primary and main drainage, consistent with reported values for air-water systems.

8.2 Recommendations for future work

Advanced theories, including those including the specific interfacial area, have been investigated comprehensively using pore-scale experiments and modeling. However, systematic studies about the specific interfacial area at REV scale has never been reported. Furthermore, quantifying the specific interfacial area of a soil directly is of much importance, especially for solute or virus transport processes in the vadose zone. We emphasize that more studies are needed to directly quantify the terms in the interfacial area evolution equation at the REV scale.

Based on our calculations of the dynamic coefficient τ, it seems that hysteresis also exists in the relationship between this coefficient and saturation. Uncertainty remains whether the specific interfacial area is capable to eliminate this hysteresis. To investigate this problem, preliminary pore-scale modeling could be performed at first. It would be of great help to have a better understanding about the hysteretic relationship between the dynamic coefficient τ and saturation.

Samenvatting

Het doel van deze studie was om de validiteit en toepasbaarheid te onderzoeken van complexe theorieën van twee-fase stromingen in poreuze media.

We begonnen met een numerieke simulatie van een horizontale water distributie experiment, waarvan experimentele data beschikbaar waren in de literatuur. Twee verschillende numerieke modellen werden gebruikt, namelijk het standaard Richard model en een model die het grensvlak tussen twee fasen expliciet in beschouwing neemt, en die we hier het "interface model" noemen. De modellen werden onderling vergeleken ten opzichte van experimentele data. Van het Richards model gebruikten we twee versies, een versie waar we rekening hielden met hysterese en een tweede versie waar we dat niet deden. Voor het interface model gebruikten we twee verschillende vormen van de Darcy vergelijking.

Het simpelste model (Richards model zonder hysterese) kon de experimentele data niet reproduceren; met name de discontinuïteit in water verzadiging tussen de twee delen van het experiment kon niet worden beschreven met het model. Het Richards model met hysterese kon de niet-uniforme water verzadigingsprofiel wel reproduceren. Alleen waren de stroomsnelheden in dat model dan veel hoger dan die van de experimenten, terwijl daarnaast de water verzadigingen in het droge deel van het experiment ernstig overschat werden door het model. Dit model kon de experimentele data wel reproduceren als onrealistische waardes voor hydrologische parameters werden gebruikt voor.

Het "interface model" kon de dynamische water verzadigingsprofiel veel beter reproduceren dan voorgaande modellen. Dit was mede omdat het model meer parameters heeft. Desalniettemin, het feit dat het interface model de discontinuïteit goed na kon bootsen bevestigde de correctheid van de aannames en hypotheses die in het model gemaakt zijn ten opzichte van hysterese in de capillariteit. Losstaand van het modelleer werk realiseerde wij ons dat gedetailleerde experimenten nodig zijn om de onzekerheid in experimentele data en theoretische analysis te verminderen, met name de onzekerheid in de begincondities en de mate van homogeniteit van het zandpakket.

Daarom hebben we zelf horizontale distributie experimenten ontworpen en uitgevoerd die goed gedefinieerd waren. We hebben een Plexiglas container gemaakt waarin de experimenten werden uitgevoerd, voor verschillende waterverzadigingen aan de droge kant van het experiment. De waterverzadigingen werden gemeten met behulp van een gamma transmissiviteit systeem, terwijl de waterdruk werd gemeten met druksensoren

die over de lengte van de container werden geplaatst. In alle experimenten bevond zich een volhardende discontinuïteit in de water verzadigingsprofiel, terwijl de waterdruk gelijk in het begin van het experiment continue werd. Resultaten lieten zien dat minder water werd uitgewisseld naar mate het verschil in de beginverzadiging kleiner werd. De experimenten werden gesimulleerd met behulp van de boven genoemde modellen. Het bleek dat door toevoeging van hysterese in de productie term van het oppervlak tussen lucht en water, het interface model vergelijkbare of zelfs betere resultaten gaf dan het Richards model.

We hebben ook het effect van dynamische capillariteit onderzocht, gebruikmakend van naar beneden stromende water infiltratie in een nagenoeg droog zandpakket. Experimenten werden gemodelleerd gebruikmakend van de twee modellen met een vergelijking voor dynamische capillariteit. Alle resultaten van de modellen verschilde substantieel van experimentele data. Zonder het dynamische effect resulteerde alle modellen in een monotonisch verzadigingsprofiel, zoals eerder gerapporteerd in de literatuur. Het interface model kon de niet-monotone verzadigingsprofiel goed nabootsen mits de hysterese parameters in de productie term werden gekalibreerd. De dynamische capillariteit is uitgedrukt in de parameter τ, die konstant werd gehouden in onze simulaties terwijl andere studies argumenteren dat τ afhangt van verzadiging. Daarom hebben we in het vervolg meer experimentele onderzoek gedaan om de afhankelijkheid van τ te bepalen.

In de modelstudie hebben we de relatie van τ met verzadiging getest door middel van vier verschillende vergelijkingen voor de afhankelijk van τ met waterverzadiging, namelijk: een constant model, een integreerbare dalende functie, een stijgende functie, en een niet-integreerbare functie. Gebaseerd op een lopende golf analyse en model resultaten, concluderen we dat de niet-integreerbare stijgende functie resulteerde in een verglijkbare nonmonotone verzadiging verdeling als in hete experiment, alleen overschatte het model de reistijden.

Uiteindelijk werden er experimenten uitgevoerd om het dynamische capillariteits parameter, τ, te kwantificeren gebruikmakend van een serie drainage experimenten. Primaire, hoofd, en scanning drainage experimenten werden uitgevoerd voor dynamische zowel als statische experimenten. De waarde van τ was bepaald door middel van waterdruk en verzadiging metingen. De waarde van τ daalde met water verzadiging voor water verzadigingen tussen 0.4 en 0.9, maar daarna steeg het met water verzadiging. The waardes van τ waren het hoogst voor primaire drainage en het

laagst voor de scanning curves. Dit betekend dat τ een niet-unieke functie is van verzadiging, en er is dus hysterese in τ.

Acknowledgements

I really would like to acknowledge a number of people for their help and support over the past four years. Because of all of them, I really enjoyed my research and my life in the Netherlands.

Foremost, I would like to express my deepest gratitude to my promotor, Majid Hassanizadeh, for everything he did for me throughout my study. I am very grateful to him for giving me an opportunity to do research in a new scientific field, multiphase flow in porous media. His optimism, enthusiasm and criticism to research deeply impressed me. His attitude to research will influence my way to both research and life in future. I must also thank him for his encouragement, for always being there to help, and for his patience with my writing. Without his help and support, this thesis would not be possible, and I could not discuss my research and collaborate with many excellent researchers. Majid, I must be so lucky to be one of your PhD students. You really showed me how to do research and how to be a supervisor. I will keep learning from you, and will become an independent researcher finally.

Special thanks are given to Pieter J. Kleingeld, Arjen de Waal and Thom Claessen for their technical support. I want to thank Pieter for his delicate designs of my experimental setups, for patient explanations of devices (gamma system, TDR, etc.), and for always giving useful suggestions or solutions of problems. I did learn a lot not only from his knowledge of experiments, but also from his attitude to his work. I am very grateful to Thom for always being patient to help me find the needs of experiments, when I just started my experiments in the early years. Many thanks go to Arjen for his valuable designs, suggestions and tests of experimental setups. Whenever I need any help in experiments, he always tried to solve my problems as fast as he can. I also want to thank Frits Meijboom for providing such wonderful tensiometers and useful discussions and suggestions. I am grateful to Hans van Aken for discussions and nice chats in the lab.

I sincerely thank my doctoral committee, Hans van Duijn, Rainer Helmig, Insa Neuweiler, Amir Raoof, Rien van Genuchten, and Azita Ahmadi, for their valuable comments and suggestions on the thesis. I wish to thank Rien van Genuchten for his discussions about my research, and for his detailed comments about my manuscripts and this thesis, and for always explaining English grammar patiently to me. Many thanks go to Hans van Duijn for his discussions about mathematical analysis of equations, and for such careful and detailed corrections about my manuscript. I also want to thank Amir Raoof and Anton Leijnse for checking my calculations very patiently, when I was just a stupid fresher in numerical field. Rainer Helmig and

Michael Celia are deeply appreciated for their useful discussions about my experiments and simulations. I am grateful to Sorin Pop and Paul Zegeling for useful mathematical discussions. I also appreciate the collaborations with Camila and Koondi. I further acknowledge Susanne Zimmermann and Tim Feuring for providing their experimental data and useful discussions.

I really appreciate my colleagues and friends in the Environmental Hydrogeology Group. I must say that these lovely gentlemen, and also our nice secretaries, make me really enjoy my daily life in this big family. First of all, I would like to thank Margreet and Annuska, our secretaries, for administrative tasks, for filling in Dutch forms, and for sharing interesting things during nice and joyful chats. Many thanks go to Ruud Schotting for his discussions and also for delicious dinners at his place. Special thanks are given to my former and current officemates, Wouter and Amir Hossein, for having a nice time every day. I acknowledge Thomas for translating the summary into Dutch. I also would like to thank the other colleagues and friends: Jack Schijven, Niels Hartog, Tom Bosma, Ioannis, Mojtaba, Willem-Bart, Hamed, Pierre, Ehsan, Lucas, Jan, Gillian, Enno, Sayantan, and Nikos, for the nice working atmosphere, joyful daily chats, wonderful group meetings, and impressive group-outing days. I would like to express my appreciations also to visitors in our group, Emilio, Hossein and Andres (my former officemates), Abhishek and Seetha from India, Philip Kunz from Stuttgart University, Bruno from France, and Andrea from Italy.

I want to thank the Chinese colleagues and friends in our group, Qiulan, Chaozhong, Shuai and Xiaoguang. A special thank is given to Qiulan for her kindly help in both research and daily life, when I just came to Utrecht. I appreciate Chaozhong for his valuable discussions in Chinese. Many thanks go to Shuai and Xiaoguang for being a labor, for help in trivial affairs, and for daily Chinese chats.

I am grateful to Forooz for her nice chats, support and delicious dinners. I also wish to thank Betty May for her nice gifts and encouragement.

I also would like to thank all the Chinese friends outside of the Environmental Hydrogeology Group but for nice chats, trips and dinners. Xue Bao, Shaohui Zhang and Ying Liu, my dear roommates, are thanked for their company during almost the whole period of my PhD. I will definitely treasure these memories we have had, happiness and sadness. I want to thank Xin Wang for impressive trips and chats. Many thanks are also given to Miao Zhang, Jiawang Wu, Jingchao Wu, Nan Xiang, Ping Huang, Xu Huang, Lulu Zhang, Jianye Chen, Jinfeng Liu, Xiaochen Liu and Xiaoqi Wang and Jie Gao, my current roommates. I further acknowledge Xiulei Cao, Bo Guo,

Bo Liang and Hong Zhang for nice chats and discussions during conferences. I sincerely thank Weihua Zhang, from Sun Yat-sen University, for her encouragement and sharing experience during the most difficult time of my research.

At last, but not at least, I thank my dear family and besties for their unconditional love to make the stressful life more enjoyable.

感谢我最亲爱的爸爸，妈妈和弟弟，谢谢你们永远无条件的支持，理解和鼓励。感谢我最亲爱的闺蜜赵洁和陈欣，谢谢你们做我的树洞听我的抱怨和唠叨，谢谢你们给我安慰和鼓励，无论二十年，三十年还是四十年以后。